Theoretical Analysis of Laterally Vibrating Microcantilever Sensors in a Viscous Liquid Medium

Russell Cox
Marquette University

Recommended Citation
Cox, Russell, "Theoretical Analysis of Laterally Vibrating Microcantilever Sensors in a Viscous Liquid Medium" (2011). *Dissertations (2009 -)*. Paper 97.
http://epublications.marquette.edu/dissertations_mu/97

THEORETICAL ANALYSIS OF LATERALLY VIBRATING MICROCANTILEVER SENSORS IN A VISCOUS LIQUID MEDIUM

by

Russell Cox, B.S., M.S.

A Dissertation submitted to the Faculty of the Graduate School,
Marquette University,
in Partial Fulfillment of the Requirements for
the Degree of Doctor of Philosophy

Milwaukee, Wisconsin

May 2011

ABSTRACT
THEORETICAL ANALYSIS OF LATERALLY VIBRATING MICROCANTILEVER SENSORS IN A VISCOUS LIQUID MEDIUM

Russell Cox, B.S., M.S.

Marquette University, 2011

Dynamically driven microcantilevers are normally excited into resonance in the out-of-plane flexural mode. The beam's resonant frequency and quality factor are used to characterize the devices. The devices are well suited for operation in air, but are limited in viscous liquid media due to the increased viscous damping. In order to improve these characteristics, other vibration modes such as the in-plane (or lateral) flexural mode are investigated. In this work, microcantilevers vibrating in the in-plane flexural mode (or lateral direction) in a viscous liquid medium are investigated. The hydrodynamic forces on the microcantilever as a function of both Reynolds number and aspect ratio (thickness over width) are first calculated using a combination of numerical methods and Stokes' solution. The results allowed for the resonant frequency, quality factor, and mass sensitivity to be investigated as a function of both beam geometry and medium properties. The predicted resonant frequency and quality factor for several different laterally vibrating beams in water are also found to match the trends given by experimentally determined values found in the literature.

The results show a significant improvement over those of similar devices vibrating in the out-of-plane flexural mode. The resonant frequency increases by a factor proportional to the inverse of the beam's aspect ratio. Moreover, the resonant frequency of a laterally vibrating beam shows a smaller decrease when immersed in water (5-10% compared to ~50% for transversely vibrating beams) and, as the viscosity increases, the resonant frequency decreases slower compared to beams excited transversely. The quality factor is found to increase by a factor of 2-4 or higher depending on the medium of operation and the beam geometry. Due to the increased resonant frequency and the decreased effective mass of the beam (compared to beams excited transversely), the estimated mass sensitivity of a laterally excited microcantilever is found to be much larger (up to two orders of magnitude). The improvement in these characteristics is expected to yield much lower limits of detection in liquid-phase bio-chemical sensing applications.

ACKNOWLEDGMENTS

Russell Cox, B.S., M.S.

I would like to thank my advisor, Dr. Fabien Josse, for his hard work, understanding, and patience over the course of this investigation. His guidance has been essential in the preparation of this dissertation and the analysis of its results. I would also like to thank him for giving me many opportunities to grow, both as a researcher and as a student. I would like to thank Dr. Stephen Heinrich for the many hours of discussion and insight into the physical modeling of the system. Thanks are also extended to Dr. Isabelle Dufour for helping to initiate research into this problem and for her continued advice. Thanks are given to Dr. Oliver Brand and his group at Georgia Institute of Technology, especially Luke Beardslee, for providing experimental data used to confirm results in this dissertation. Thanks are also due to my entire research committee (Dr. Fabien Josse, Dr. Stephen Heinrich, Dr. Isabelle Dufour, Dr. Edwin Yaz, and Dr. Susan Schneider) for their corrections and suggestions on how to improve this dissertation. I would like to thank Dr. Edwin Yaz for his useful input into my research. Thanks are also due to Dr. Susan Schneider for her advice and guidance. I would also like to thank Dr. Nicholas Nigro for the many helpful discussions on the numerical modeling of the problem. Thanks are also given to current and former members of the Microsensor Research Group, especially Dr. Arnold Mensah-Brown, Dr. Michael Wenzel, Dr. Florian Bender, Tao Cai, and Jinjin Zhang.

Finally I would like to thank my family, friends, and church for offering me support throughout the time it took to complete this work.

TABLE OF CONTENTS

CHAPTER

LIST OF TABLES

LIST OF FIGURES

1. Introduction

1.1 Microcantilevers as Chemical Sensor Platforms

Microcantilevers are devices that have great potential as micro-scale sensing platforms due to their high mass sensitivity and low fabrication cost. Advances in photolithography and other microfabrication techniques have allowed the fabrication of these small beams from silicon wafers or silicon-on-insulator (SOI) wafers with dimensions ranging from millimeters to nanometers [1-8]. The small relative mass of these microcantilevers make them ideal platforms as highly sensitive mass sensors. Depositing mass onto a microcantilever operating in a resonance mode changes the frequency at which it resonates. The magnitude of this change can be used to quantify the amount of added mass, allowing the microcantilever to be used as a mass sensor [9-14]. Using microspheres of various materials attached to the microcantilever's tip, masses in the range of picograms (10^{-12} g) have been detected [14], with the predicted minimum detectable mass in the range of femtograms (10^{-15} g) [15].

Microcantilevers have also been utilized extensively in bio-chemical sensing applications [1,2,15-44]. Applications range from detecting gases such as mercury vapor [21-22,25,42], volatile organic compounds [1,19,28], to very specific biological detection applications such as the detection of Bacillus Anthracis spores [34], as well as many other applications. As a biochemical sensor, the microcantilever is generally coated with a chemically sensitive polymer layer, self-assembled monolayers, a metal film, or a layer of biochemical receptors [31]. This layer selectively sorbs and concentrates particular analytes of interest from the operating environment. The result is a change in the layer's characteristics such as its mass, volume, and viscoelastic properties [27,31,45-46]. The concentration of particular analytes in the operational medium can then be estimated by measuring the changes in the static deflection and/or the resonant frequency of the coated cantilevers. This layer is normally partially selective, so that it only responds to a particular group of analytes with similar chemical characteristics. The selectivity of the biochemical sensor can be further improved using an array of microcantilevers.

Due to their small size, several microcantilevers can be fabricated in a small area (usually on the order of 1 mm^2) [17,47]. This allows for the creation of micro-scale arrays of microcantilevers [5,17,27,41,48]. Each microcantilever can be coated with a layer of different chemical sensitivity which causes each microcantilever to respond differently when exposed to a particular analyte. Pattern recognition schemes such as linear discriminants analysis (LDA) or principal components analysis (PCA) can then be used to correctly identify unknown analytes in the medium of operation [18,49]. However, care must be taken when spacing the microcantilevers in an array. If the microcantilevers are spaced too far apart, there might not be enough space available for the number of microcantilevers required for successful identification. If they are placed too close together, the microcantilevers might interact and couple in the medium of operation [11,50] This interaction is dependent both on the medium of operation and the choice of the mode of operation.

1.2 Static and Dynamic Mode Operation

Microcantilevers can be operated in two fundamental modes: the static mode and the dynamic mode [27,31,51]. When the microcantilever is operating in the static mode, the static deflection of the microcantilever is used as an indicator of changes in the sensing layer. When the microcantilever is operating in the dynamic mode, changes in the sensing layer are indicated by changes in the microcantilever's resonant frequency. A material commonly used for the sensing layer is a chemically selective polymer [52]. Polymers can be deposited or applied on one surface of the microcantilever through spincoating, spray-coating, vapor deposition, or dip-coating [1,53-55]. Analyte molecules interact with the polymer layer through the process of adsorption (adhering to the surface) and absorption (penetrating through the surface and diffusing into the layer) [56]. Analyte sorption (the combination of adsorption and absorption) differently affects each mode of operation.

In static mode operation, the analyte absorption causes electrostatic and steric effects which in turn cause the polymer layer to swell [18,31,39]. The base layer is normally constructed of a chemically inert material, and thus will not expand. This stress differential between the coating and the base causes the microcantilever to deflect. The deflection is similar in nature to the operation of a bimetallic thermostat, which deflects due to the mismatch in stress caused by two different coefficients of thermal expansion [18,31,57-58]. While the surface stress caused by interaction between the sorbed analyte and the coating is a function of the amount of mass absorbed, the actual mass loading doesn't directly cause the deflection [18,31,57]. One of the drawbacks in static mode operation is the sensor's long response time to analyte exposure. The time it takes the deflection to reach its steady state value depends on the characteristics of the microcantilever, the characteristics of the polymer, and the rate of absorption and diffusion of the analyte through the polymer layer [18].

A method of reducing the response time of the system is to operate the microcantilever in the dynamic mode. Operating in the dynamic mode excites the microcantilever into resonance. Several types of transduction mechanisms have been used to excite microcantilevers into resonance, including electrothermal [59-61], electrostatic [59,62], electromagnetic [59,62], and piezoelectric [59,62-63]. The microcantilever can even use the thermal noise of the system to undergo self-resonance [64-65]. Once the microcantilever is excited, the deflection of the microcantilever as a function of excitation frequency can be measured. A common method of measuring the deflection is by optical readout using a laser. The laser can be shone onto the microcantilever at a particular angle and the angle of the reflected beam related to the magnitude of the deflection [19,27,31]. The microcantilever deflection can also be measured indirectly by circuitry placed on the microcantilever. A Wheatstone bridge made up of piezoresistors can be fabricated either on or next to the microcantilever [1,61,66-67]. As long as at least one of the piezoresistors in the Wheatstone bridge is on the microcantilever, the deflection-induced stress will cause the resistance of the piezoresistors on the microcantilever to change. This change in resistance will cause a change in the bridge voltage which can then be related to the deflection of the microcantilever.

Once the deflection is measured, the magnitude of the deflection can be investigated as a function of the frequency of excitation. The shape of the magnitude spectrum is roughly a Lorentzian around the resonant frequency of a particular mode [4]. If the loss is low enough, the system can be modeled as if it were an RLC-circuit [68]. The equivalent capacitance can be determined by the inverse of the microcantilever's stiffness; the equivalent inductance determined by the mass of the microcantilever (as well as the displaced mass of the medium); and the equivalent resistance determined by the damping of the system [68]. An RLC-circuit will resonate at a particular frequency. If a property of the microcantilever or operating medium is altered, such as the mass of the sensing layer, the frequency at which the system resonates will also change. Operating in the dynamic mode will thus allow instantaneous detection of mass uptake by the coating. Changes in the viscoelastic properties of the sensing layer [45,69] and the viscosity and density of the medium of operation [70-72] can also be detected in this manner. This work will primarily deal with dynamic mode operation.

1.3 Gas and Liquid Phase Sensing

There are numerous examples of dynamically driven microcantilevers used as sensing platforms. Historically, the use of microcantilevers as sensing platforms arose out of modifications to standard atomic force microscopes (AFMs), which are microcantilevers with sharp tips on their free end. The tip is placed into contact with a surface of unknown height. In a vacuum, the tip is repulsed by chemical, van der Waals, electrostatic, and magnetic forces when it gets within 100 nm of the surface [73]. When operating in a gas or a liquid, the AFM tip is repulsed by meniscus forces formed by adhesion layers on the tip and surface of the sample [73]. The deflection of the AFM is then related to the height of the unknown surface. In the 1990s, AFMs were observed to be sensitive to various ambient effects from the environment [22,71,74]. Since then, dynamically operating microcantilevers have been applied to a large variety of gas-phase detection applications [1,15,20-23,25,27,40,67,75-81]. These include but are not limited to the detection of simple gasses such as hydrogen [76], helium, nitrogen, and carbon dioxide [40], environmental contaminants such as mercury vapor [21-22,25] or volatile organic compounds [1,78], and explosive residues in air [9,27,79]. While a large number of works have been done related to gas-phase detection, there are fewer works to be found on direct detection in liquid-phase.

Liquid-phase detection of aqueous analytes can be done either directly or indirectly. Indirect detection utilizes gas-phase sensors to detect the analyte as it evaporates off the liquid sample. However, this changes the phase of the analyte to a vapor and limits the analytes that can be detected to volatile or semi-volatile chemicals. Some liquid sensing applications require the device to be placed directly in the sample. This allows the analyte to be detected without having to undergo a change in phase, allowing for the detection of non-volatile and biological analytes in liquids.

Many liquid-phase sensing applications have used dynamically driven microcantilevers to sense analytes [9,16,28,30,31,35-36,46-47,61,64,68,70-72,74,82-83]. However, a dynamically driven microcantilever's frequency stability and mass sensitivity decrease drastically when exposed to a viscous liquid medium, thus decreasing its usefulness as an effective sensing platform [24,35,71,84-85]. These decreases are due to the additional fluid resistance (combined effects of fluid-related inertial and viscous forces) from the medium [35,45,84,86]. As the microcantilever vibrates, it drags along a portion of the fluid. This fluid mass acts to increase the effective mass of the microcantilever which, in turn, decreases the microcantilever's resonant frequency. Since the densities of liquids are much higher than those of gases, the resonant frequency of the microcantilever will drastically decrease when placed into a liquid. The increased viscosity of the medium also decreases the resonant frequency by increasing the viscous damping from the medium of operation. The increased damping will also broaden the frequency spectrum, which, in turn, decreases the frequency stability of the system.

A useful characteristic used as a measure of the frequency stability of a resonating device is the quality factor. The quality factor, denoted by Q, is usually defined within the context of systems with damped oscillatory behavior. Two possible definitions can be used when dealing with dynamically driven microcantilevers [87]. The first definition is 2π times the ratio of the maximum energy stored in the system to the amount of energy dissipated in one cycle. The 2π keeps the definition consistent with the second definition, which is the ratio of the resonant frequency to the half power or 3 dB bandwidth of the system. When working with systems that undergo resonance, the 3 dB bandwidth definition is normally used to calculate the quality factor, as the 3 dB bandwidth is easily obtainable from the deflection measurements. Ideally, the energy definition should be used. However, it is noted that when the fluid damping is low (such that $Q \gg 1$), the two definitions are equivalent [85,87].

Common dynamically driven microcantilevers vibrating in the out-of-plane direction have quality factors upwards of 20,000 in a vacuum and around 500 in air, depending on the geometry of the microcantilever [24,30,88]. The minimum detectable mass of analyte that a microcantilever chemical sensor can detect is proportional to the resonant frequency and inversely proportional to the quality factor of the system [89].

When operating in a viscous liquid environment, the quality factor can drop as low as the single digits, raising the minimum detectable mass by several orders of magnitude [24,30,84,86]. The resonant frequency also decreases drastically when the microcantilever is operating in a viscous liquid medium, causing a similar decrease in both mass sensitivity and chemical sensitivity [24].

Dynamically driven microcantilevers would be ideal liquid-phase sensing platforms if it were not for this decrease in both the resonant frequency and the quality factor [24,35,71,85]. Many techniques have been utilized to improve both the resonant frequency and the quality factor of a dynamically driven microcantilever. Increasing the resonant frequency while maintaining a constant 3 dB bandwidth increases the quality factor. The sensitivity would also increase, as it is a linear function of the resonant frequency [89]. One way of obtaining a higher resonant frequency is to operate in a higher-order mode. Higher-order modes have flexural mode shapes that have one or more points along the length of the microcantilever (besides the clamped end) that do not deflect as a function of time [90]. Both theoretical [90] and experimental investigations [10,91] show that when working in air or liquids, the quality factor of a microcantilever operating in a higher-order mode is higher than the same microcantilever operating in the fundamental mode. There are some drawbacks to operating in higher-order modes, such as an increase in support loss. The support losses for a particular microcantilever operating in the second mode are 10 times larger than operating in the first mode [92-93]. When working in a vacuum, experiments have shown that the quality factor of the microcantilever decreases with an increasing mode number [60]. This tends to be less of a concern when operating in air or liquid, since the viscous losses generally dominate the support losses [94]. Higher-order modes also correspond to stiffer behavior and, thus, to smaller deflections than the fundamental mode [60].

Another way of increasing the microcantilever's resonant frequency and quality factor is by increasing the stiffness of the microcantilever. Using a material with a higher Young's modulus can increase the stiffness of the microcantilever. However, the material chosen for the microcantilever is normally a function of the fabrication process and cannot be altered. The microcantilever can also be made stiffer by shortening its length. The resonant frequency of a microcantilever operating in a fluid is roughly proportional to the inverse of its length squared. Thus, decreasing the length by 10% would increase the resonant frequency by ~23% [45]. Shorter microcantilevers also have less surface area when interacting with the surrounding medium, thus decreasing the amount of fluid damping. There are a few drawbacks to decreasing the length of the microcantilever. The support loss also increases for shorter microcantilevers. Again, this is less of a concern when operating in fluids as the increase in the support loss is negligible compared to the reduction of the viscous losses. The deposition reproducibility is a function of the surface area of the microcantilever [92]. Decreasing the length will then decrease the deposition reproducibility, which will increase the error in the estimate of the thickness of a deposited sensing layer. Finally, while smaller surface areas lead to smaller levels of fluid damping, they also lead to smaller amounts of analyte that can be sorbed into the sensing layer. This will decrease the change in the resonant frequency due to the sorbed analyte.

The stiffness of the microcantilever can also be increased by operating in a different vibration mode. The most common mode of operation is in the transverse flexural mode, which vibrates the microcantilever in the out-of-plane direction [1,2,9,16,17,19,23,27,31,43,45]. Microcantilevers can operate in many other vibration modes. Both the torsional mode (torsion or twisting) and the lateral flexural mode (bending vibration in-plane) have been investigated in the literature [10,60-61,84,95-97]. The torsional mode can be excited by applying a torque to the microcantilever, causing it to twist. The torsional mode has been investigated both theoretically [95] and experimentally in air [10,96]. The quality factor of a particular microcantilever is found to be larger when operating in the torsional mode compared to the transverse flexural mode [10,95]. While few investigations have been conducted using the torsional mode in liquid, the quality factor using the torsional mode is still predicted to be higher than in the transverse flexural mode [95].

Excitation of the in-plane flexural mode has also been suggested in the literature as another technique for increasing the resonant frequency and the quality factor of dynamically driven microcantilever biochemical sensors [10,84,97]. Microcantilevers can be excited in the lateral direction as shown in Fig. 1-1 by the application of a lateral driving force. It is expected that driving the microcantilever in the lateral direction will cause it to encounter less fluidic damping, which will increase its resonant frequency and quality factor. Due to the change in the direction of vibration, the microcantilever's flexural rigidity will increase compared to microcantilevers vibrating transversely by a factor of $(b/h)^2$, where b and h are the width and the thickness of the microcantilever, respectively. This will increase the resonant frequency. Microcantilevers operating in the in-plane direction have also been investigated both theoretically [84,97] and experimentally [60-61].

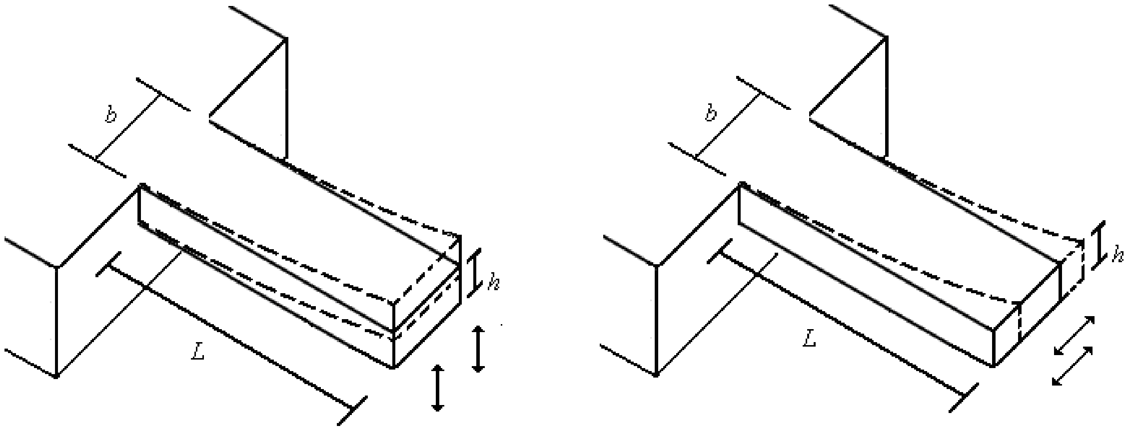

Out-of-plane Flexural Mode
(Transverse Excitation)

In-plane Flexural Mode
(Lateral Excitation)

Figure 1-1. An illustration of a microcantilever undergoing transverse (left) and lateral (right) excitation.

As was the case with operating in a higher-order mode or shortening the microcantilever’s length, the support loss increases when operating in the lateral flexural mode. Experimentally determined quality factors for laterally vibrating microcantilevers in vacuum have been found to be lower than similar microcantilevers vibrating in the out-of-plane flexural mode [60]. However, the resonant frequency of each mode is different and the primary benefit of operating in the lateral flexural mode comes from the decreased fluid drag. In air, the quality factors of laterally vibrating microcantilevers were experimentally found to be significantly higher than the same microcantilevers operating in the transverse flexural mode [10]. When operating in liquid, the quality factor can reach 70 or higher depending on the microcantilever’s geometry [61].

There have been several attempts to model the characteristics of laterally vibrating beams, such as its resonant frequency and quality factor. A laterally vibrating beam can be modeled by a method similar to the method used to model the transversely vibrating beam [84]. This approach works when the device is operating in air or vacuum. However, when laterally vibrating microcantilevers are operating in viscous liquid media, only the pressure forces on the thickness dimension would be considered, neglecting the effects of fluid shear acting on the width dimension. Other approaches assume that the fluid shear on the width is dominant compared to the pressure [98-99]. The hydrodynamic damping is approximated using the solution to Stokes' second problem which modeled the forces acting on an infinitely vibrating flat plate [98-99]. However, this approach neglects the effects of the pressure on the thickness dimension. Recently, these effects have been found to contribute significantly to the overall hydrodynamic force acting on a laterally vibrating microcantilever [100]. Each of these forces and their effects on the characteristics of the device, such as the resonant frequency, quality factor, and mass sensitivity, should be modeled and their significance investigated.

1.4 Modeling Laterally Vibrating Microcantilevers

Transversely vibrating microcantilevers have been successfully modeled using standard Euler-Bernoulli beam theory. The same method can be used to model laterally vibrating microcantilevers operating in a vacuum with the width and thickness switched in the equation of motion. When operating in a viscous liquid medium, the effects of the hydrodynamic force acting on a laterally vibrating microcantilever may be important; moreover, the relative importance of the various contributions to this force are fundamentally different than those corresponding to transverse vibrations and these differences must therefore be taken into account. This includes modeling both the pressure and fluid shear, accounting for the edge effects and the effects of thickness [100-

102]. This will allow the case of using lateral excitation to be compared with that of transverse excitation.

The total force from the pressure is composed of the hydrostatic and the dynamic pressures [101]. It will be assumed in this work that there is no net fluid flow. Thus, there is no net force acting on the microcantilever from the hydrostatic pressure. There is also no net dynamic pressure acting on a vibrating rectangular microcantilever in the direction perpendicular to its vibration. However, there is a net dynamic pressure in the direction applied parallel to the microcantilever's vibration. This force is applied on the surfaces of the microcantilever which are perpendicular to the motion of vibration [90,97]. Since these surfaces involve the thickness dimension of the microcantilever when it is vibrating in the in-plane direction and the width dimension when it is vibrating in the out-of-plane direction, it is assumed that the hydrodynamic force from the pressure will be smaller when vibrating in the in-plane direction. However, when the microcantilever is vibrating in the in-plane direction, the pressure force may not be the dominant fluid force, as was assumed in Ref. 84.

The pressure forces of microcantilevers vibrating in the out-of-plane direction were originally found by Tuck in Ref. 102. From the linearized version of the Navier-Stokes' equation, Tuck was able to derive an integral equation relating the velocity at any point in the medium to the fluid shear and pressure along the contour of the cross-section of the microcantilever. In order to find the fluid shear and pressure, the velocity of the medium must be known on some contour in the medium. The velocity of the microcantilever is known. The velocity of the fluid and microcantilever can be considered equal at the fluid-beam interface if the medium of operation can be considered a continuum. This boundary condition is called the no-slip condition. The medium can be considered a continuum if it is a liquid or if it is a gas with a Knudsen number (the ratio of the mean free path of molecules in the medium to the width of the microcantilever) less than 0.01 [103]. For air at standard temperature and pressure, the mean free path of molecules is 65 nm [103], meaning that the microcantilever's width in air must be greater than 6.5 μm. This condition is satisfied since in this investigation all the microcantilever's widths in air are greater than 6.5 μm. This boundary condition can be used with Tuck's integral equation to check if a particular given fluid shear and pressure distribution along the microcantilever's cross-section is valid. However, the integral equation has not been analytically solved to find the pressure and fluid shear from this boundary condition.

Using a numerical method called the Method of Moments, the integral equation can be discretized and the average pressure and shear can be estimated along particular segments of the microcantilever's cross-section. Tuck assumed the microcantilever to be a ribbon (infinitely thin) and vibrating transversely, so that both the thickness effect and the fluid shear could be neglected. The pressure acting on this transversely vibrating ribbon was found to be very similar to that of a vibrating circular cylinder [102]. A correction factor was obtained in Ref. 85 that mapped the well-known analytical expression for the hydrodynamic force acting on a vibrating cylindrical pendulum [104] to that of an infinitely thin microcantilever vibrating in the out-of-plane direction. However, this method only accounts for the pressure force.

In order to fully model the hydrodynamic forces, the frictional drag from the fluid shear must also be taken into consideration [100]. The fluid shear force is expected to be larger for microcantilevers vibrating in the in-plane direction as opposed to the out-of-plane direction since the shear force will act on the larger surfaces, i.e., those parallel to the direction of motion. The fluid shear force is expected to be the dominant hydrodynamic force for microcantilevers with small thicknesses when the microcantilever is vibrating in the in-plane direction.

As noted before, the hydrodynamic force from the fluid shear can be approximately modeled using the results for the fluid shear found by Stokes for an infinite flat plate vibrating in the in-plane direction [105]. This problem is commonly referred to as Stokes' second problem in the literature [106]. As the plate is infinitely wide, there are no edge effects (non-uniform hydrodynamic forces near the edges of a finite surface) or pressure effects assumed acting on the plate. Again, the linearized version of the Navier-Stokes equation was used to model the fluid velocity. A partial differential equation (PDE) with respect to the stream function can be found in the form of a modified biharmonic equation. The stream function defines the stream lines in the fluid and the curl of the stream function is equal to the fluid velocity [102]. From this PDE, Tuck was able to create the integral equation given in Ref. 102. Since Stokes made the assumption that the plate was infinitely wide, the assumption could be made that the stream function was constant in the direction of the width. From this assumption, a general form of the solution to the PDE could be written. Using the no-slip condition and the assumption that the fluid velocity at infinity is zero as boundary conditions, the fluid shear on the laterally vibrating plate can be found. The total fluid shear per unit length for a laterally vibrating microcantilever at a certain point along the length of the beam can then be approximated by the fluid shear per unit length acting on a laterally vibrating plate with the same velocity and frequency of excitation. However, this approximation does not take into account the microcantilever thickness or the edge effects.

To account for these additional effects, several studies have attempted to model the cross-section of vibrating beams or cylinders in viscous liquids as ellipsoids [100,107-109]. Utilizing an elliptical coordinate system, the PDE was solved and the exact analytical solution of the hydrodynamic forces derived for a vibrating ellipsoid in Ref. 100. The solution was obtained in terms of an infinite series of Mathieu functions. The resulting formulation is complicated and fails to account for the sharp edges of the non-streamlined rectangular cross-section.

Very recently, an investigation expanded upon the method used in Ref. 102 to obtain numerical results that accounted for the edge and thickness effects of a rectangular cross-section [97]. The investigation used the same integral equation as Tuck in Ref. 102 but did not use the assumption of zero thickness. The hydrodynamic forces found were similar to those found in the present investigation. However, the results were found for particular thicknesses and media and no attempt was made to create an analytical expression for the hydrodynamic forces. A comparison between the hydrodynamic forces found in Ref. 97 and those found in this investigation will be presented.

Other investigations have attempted to use finite element analysis (FEA) in order to account for the edge effects and the effects of thickness [86,107]. Finite element analysis is a numerical technique which is comparable to the method of moments technique used in Ref. 102, only the techniques used at approximating the PDE are much more efficient and are available from many different commercial FEA programs. While it is easier to define the problem using FEA compared to other methods, FEA is still a numerical technique and a sufficient number of fluid elements must be used to ensure an accurate solution. FEA allows for the pressure and shear force to be found on the microcantilever’s cross-section as well as in the medium surrounding the microcantilever as a function of time. However, as with the method used in Ref. 97, this technique does not yield an analytical expression for the hydrodynamic forces as a function of the properties of the medium of operation and the microcantilever’s thickness.

The effect of thickness of a microcantilever vibrating in the out-of-plane mode has been investigated using FEA [107]. The numerical results were fit to the form of Oseen’s approximation of the drag force of an elliptical cylinder [110]. Using the same method, the edge effects and the thickness effects can be accounted for and an expression for the hydrodynamic forces acting on a microcantilever vibrating in the in-plane direction can be found. However, Oseen’s approximation only considered transversely vibrating elliptical cylinders where Re<<1 [111]. Stokes’ technique modeling the viscous drag on an infinite flat plate is a more appropriate technique to model lateral vibration and can be used at higher Reynolds numbers, thus making it a better technique for approximating the physical system. Using FEA, the numerical results can be used to modify Stokes’ solution to account for edge effects and thickness effects.

1.5 Problem Statement and Objectives

Dynamically driven microcantilevers have been used as highly sensitive gas-phase chemical sensors for many different applications. The use of these sensors in liquid-phase sensing applications has been limited due to the device’s decreased frequency stability and decreased sensitivity caused by the larger fluidic forces when operating in a liquid. Several methods have been investigated to improve the sensing characteristics including operating the microcantilever in higher-order modes and shortening the microcantilever’s thickness. Another promising method mentioned in the literature [10,60-61] of increasing both the resonant frequency and quality factor is to flexurally vibrate the microcantilever in the in-plane direction.

Dynamically driven microcantilevers are commonly vibrated in the out-of-plane direction. Experiments have shown that when the microcantilever is excited in the in-plane direction, both the resonant frequency and the quality factor are improved in both air and liquid [10,61]. In order to theoretically compare the benefits of using lateral excitation over transverse excitation, one must first define and account for all the hydrodynamic forces acting on the laterally excited microcantilever. These include both the pressure force and the fluid shear force taking into account both the effects of the thickness of the microcantilever and the edge effects. Several attempts at modeling the hydrodynamic forces of a laterally vibrating microcantilever have been made. Some investigations focused on modeling either the pressure or the fluid shear, but not both. Other investigations attempted to model the microcantilever as either a vibrating ribbon or an ellipsoid. However, in order to accurately account for all the forces, the edge effects, and the effects of thickness, both the pressure and the fluid shear force must be considered and found for a vibrating microcantilever with a rectangular cross-section.

The primary objective of this work is to theoretically characterize and compare the characteristics of microcantilever-based biochemical sensors vibrating in the in-plane and out-of-plane direction and note the differences in characteristics of interest when the microcantilever is excited in the in-plane direction. Characteristics such as the microcantilever's resonant frequency, quality factor, sensitivity, and limit of detection will be investigated. These characteristics may be determined by solving the system's equation of motion. However, the equation of motion can only be solved if the hydrodynamic forces acting on a laterally excited microcantilever are known.

The hydrodynamic forces will be expressed via the steady state solution to Stokes' second problem modified using a correction factor. The form of the correction factor will be determined by performing FEA on the fluid domain. This correction factor will account for both the effects of the thickness and the edge effects. Once the hydrodynamic forces are known, the equation of motion for the microcantilever can be solved and characteristics of the device can be extracted and investigated as a function of the direction of excitation, as well as functions of the geometry and the medium of operation. The trends in these characteristics can be used to improve the choice of device geometry for liquid-phase detection, as well as quantify the benefits and drawbacks of using in-plane vibration as opposed to out-of-plane vibration.

1.6 Dissertation Organization

This dissertation is organized into five chapters. In chapter 2, the equation of motion will be solved for the deflection of a microcantilever vibrating in the in-plane direction in a viscous liquid fluid. The result will be expressed in terms of an arbitrary exciting frequency. This can be used to find the characteristics of a microcantilever vibrating in the in-plane direction if the hydrodynamic forces are known. Chapter 3 will define all the hydrodynamic forces and present Stokes' solution. It will also include a finite element analysis model used to approximate the hydrodynamic forces. Using the results of this numerical procedure, a correction factor for Stokes’ solution can be found and an analytical function for the hydrodynamic forces obtained. Chapter 4 uses the expression for the sum of the hydrodynamic forces from chapter 3 to extract useful characteristics, such as the resonant frequency, quality factor, and sensitivity. Trends in these characteristics as functions of microcantilever geometry and medium properties are found and recommendations made for design considerations. The characteristics of microcantilevers of similar geometry excited both laterally and transversely are then compared and contrasted. Finally, chapter 5 gives a summary of the results and identifies areas of future research.

2. Laterally Excited Microcantilevers in a Viscous Liquid Medium

2.1 Introduction

In order to analyze a laterally vibrating microcantilever in a viscous liquid medium, it is first necessary to obtain the solution to the equation of motion governing the deflection of the microcantilever. This will allow the characteristics of the vibrating microcantilevers to be found and investigated as functions of geometry, material properties, medium properties, and excitation direction. Figure 2-1 shows the microcantilever's length, L, width, b, and thickness, h. The origin is placed at the center of the beam-support interface with the x-axis, y-axis, and z-axis in the direction of the microcantilever's length, width, and thickness, respectively. The microcantilever is clamped at x=0 and has a free end at x=L. Also shown in Fig. 2-1 is the lateral deflection in the y direction, denoted by $v(x,t)$. Please note that $v(x,t)$ stands for the lateral displacement of the microcantilever as a function of both time and position along the length of the microcantilever, and is not the microcantilever's velocity.

The microcantilever in Fig. 2-1 can be modeled using standard Euler-Bernoulli beam theory if certain assumptions listed below are satisfied. The equation of motion for a laterally vibrating microcantilever in a vacuum under harmonic loading is

$$EI_{lat}\frac{\partial^4 v(x,t)}{\partial x^4}+\rho_B bh\frac{\partial^2 v(x,t)}{\partial t^2}=F_y(x)e^{j\omega t} \qquad \textbf{(Eq. 2-1)}$$

where

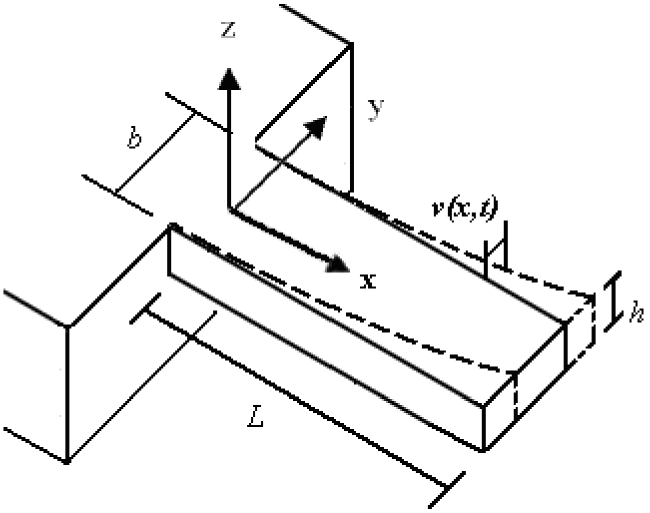

Figure 2-1. A microcantilever with length, *L*, width, *b*, and thickness, *h* vibrating laterally with a deflection of *v*(*x*,*t*).

$$I_{lat} = b^3 h / 12\,. \tag{Eq. 2-1a}$$

In Eq. 2-1, *E* is the Young's modulus of the microcantilever in the longitudinal direction, ρ_B is the mass density of the microcantilever, and $F_y(x)$ is the position-dependent forcing function per unit length operating at an angular frequency of ω.

Note that the equation for the moment of inertia, I_{lat}, has the width cubed instead of the thickness (opposite the case of transverse vibration). The Young's modulus is the same for both lateral and transverse vibration. Thus, the flexural rigidity (*EI*) of a microcantilever undergoing lateral vibration is a factor of $(b/h)^2$ times larger than that of the same microcantilever undergoing transverse vibration. This increased flexural rigidity indicates that the beam is stiffer (compared to the same beam vibrating transversely). Since the beam is stiffer when vibrating laterally, yet has the same amount of mass, it will have a higher resonant frequency [84].

Euler-Bernoulli beam theory places several assumptions on the beam geometry and deflection and, thus, the applicability of Eq. 2-1:

- The beam's cross-sectional area is uniform over the length of the beam
- The length of the beam greatly exceeds its width
- The amplitude of the vibration of the beam is far smaller than any length scale in the beam geometry

It will also be assumed in this work that the density and Young's modulus are also uniform over the length of the beam. These assumptions generally hold true for standard commercially available microcantilevers [85] However, some of the geometries investigated in this work do not have lengths that greatly exceed their widths. The effects of violating this assumption will be investigated in chapter 4. For microcantilevers made of several different layers of materials, the weighted average mass density can be used as the beam density. Likewise, an effective Young's modulus can be found (either via composite beam theory [1] or use of experimental data) for a multilayer beam. If the microcantilever's cross-sectional area changes as a function of *x*, such as in the case of a hammerhead or T-shaped microcantilever, the additional mass and rotational inertia of the head must be taken into account. One method of accounting for this additional mass is to use Rayleigh's method, modeling the additional mass as a point mass at the end of the microcantilever [112]. Other methods utilize finite element analysis in order to model the additional effects of the head [113]. However, only beams that have a constant cross-section are considered in this investigation. If the length of the laterally vibrating microcantilever is on the order of its width, the shear strain and rotational inertia effects must be taken into account using Timoshenko's beam theory [57] in place of Euler-Bernoulli's beam theory. Finally, if the amplitude of the vibration is too large, the problem becomes geometrically nonlinear and the stress versus strain relationship can possibly become non-linear; in these cases failure criteria such as lateral-torsional buckling might need to be taken into account [59,114].

2.2 Effects of a Viscous Liquid Medium

When the microcantilever operates in a viscous liquid medium, an additional force from the medium affects the microcantilever and the equation of motion is modified to

$$EI_{lat}\frac{\partial^4 v(x,t)}{\partial x^4}+\rho_B bh\frac{\partial^2 v(x,t)}{\partial t^2}=F_y(x)e^{j\omega t}+F_{medium,lat}(x,t)\,. \qquad \textbf{(Eq. 2-2)}$$

This additional hydrodynamic force, $F_{medium,lat}$ is a force per unit length that is partially out-of-phase with the displacement, and can be represented as

$$F_{medium,lat}(x,t)=-g_{1,lat}\frac{\partial v(x,t)}{\partial t}-g_{2,lat}\frac{\partial^2 v(x,t)}{\partial t^2} \qquad \textbf{(Eq. 2-3)}$$

where $g_{1,\mathrm{lat}}$ and $g_{2,\mathrm{lat}}$ are time-independent coefficients associated with the fluidic damping force per unit length and the fluidic inertial force (displaced fluidic mass) per unit length, respectively [85-86]. It is common to normalize $F_{medium,lat}$ into a dimensionless form called the hydrodynamic function, Γ_{lat}, where [3,85]

$$g_{1,lat}=\eta\,\mathrm{Re}\,\Gamma_{lat,I}(\mathrm{Re},h/b)\,, \qquad \textbf{(Eq. 2-4)}$$

$$g_{2,lat}=\frac{\pi}{4}\rho_L b^2\Gamma_{lat,R}(\mathrm{Re},h/b)\,. \qquad \textbf{(Eq. 2-5)}$$

where ρ_L and η are the mass density and dynamic viscosity of the fluid, respectively. The subscripts *R* and *I* in Eqs. 2-4 and 2-5 represent the real and imaginary portions of the hydrodynamic function, respectively, where *h/b* is the aspect ratio of the beam cross-section and Re is the Reynolds number of the system.

The Reynolds number is a measure of the relative size of the fluid’s inertial and viscous forces in the problem. An analytical expression for the Reynolds number can be defined from the ratio of the inertial term to the viscous term in the equation of motion of the fluid. The linearized incompressible form of the Navier-Stokes’ equation can be used to model the fluid if the fluid is assumed incompressible and the velocity gradient of the fluid is small. The fluid can be considered incompressible as the wavelength of the microcantilever’s vibration in the cases of interest in this work greatly exceeds the width of the microcantilever, which is the dominant length scale in the flow [85]. The velocity gradient of the fluid is related to the velocity gradient of the vibrating microcantilever. Since it is assumed that the microcantilever’s amplitude of vibration is far smaller than any length scale in the microcantilever’s geometry, the velocity gradient of the beam and fluid can be considered small. Thus, the equation of motion for the fluid can be given as [86, 98, 109]:

$$\rho_L \frac{\partial u}{\partial t} = -\nabla P + \eta \nabla^2 u \qquad \textbf{(Eq. 2-6)}$$

where *P* and *u* are the pressure and velocity at a particular point in the fluid, respectively. The term on the left hand side of Eq. 2-6, $\rho_L \frac{\partial u}{\partial t}$, is the term related to the fluid’s inertial forces. The second term of the right hand side of Eq. 2-6 , $\eta \nabla^2 u$, is the term related to the fluid’s viscous forces. The Reynolds number, in this form sometimes called the nondimensional frequency [102] or one fourth of the Valensi number [115], can then be found by taking the ratio of these terms and simplifying,

$$\mathrm{Re} = \frac{|\rho_L \frac{\partial u}{\partial t}|}{4|\eta \nabla^2 u|} = \frac{\rho_L \omega b^2}{4\eta}. \qquad \textbf{(Eq. 2-7)}$$

The viscous term is multiplied by a factor of four to keep the definition consistent with the one found in Ref. 102.

The hydrodynamic function, Γ_{lat}, is the total hydrodynamic force per unit length applied by the fluid onto the microcantilever normalized to the amount of force per unit length needed to excite fluid in a vibrating circular cylinder of diameter *b* to the same velocity as the microcantilever. The normalized hydrodynamic force per unit length is dependent on the microcantilever's aspect ratio. This dependency will be investigated in chapter 3.

The hydrodynamic function is also dependent on the properties of the medium of operation. The properties of the medium of operation, along with the excitation frequency ω, will determine the skin depth of the liquid layer surrounding the vibrating beam. The skin depth or boundary layer thickness, denoted δ, is defined as the distance over which the fluid velocity decays to 1/*e* of its maximum value [116]. The larger the skin depth, the larger the amount of fluid excited by the vibrating beam. Physically, the boundary layer thickness can be thought of as the amount of fluid trapped in the vortex created by the vibrating microcantilever [104]. The boundary layer thickness can be found as

$$\delta = \sqrt{\frac{2\eta}{\rho_L \omega}} \ . \qquad \textbf{(Eq. 2-8)}$$

Equation 2-8 can be rewritten as

$$\delta = \frac{b}{\sqrt{2\,\mathrm{Re}}} \qquad \textbf{(Eq. 2-9)}$$

The hydrodynamic function for a transversely vibrating beam was found to be a function of δ/b, or a function of the inverse of the square-root of the Reynolds number [86,116]. It is expected that the hydrodynamic function for a laterally vibrating beam will also depend on this ratio, and thus on the Reynolds number.

The hydrodynamic function is a complex number. The real portion of the hydrodynamic function is related to the effective displaced fluid mass per unit length and the imaginary portion of the hydrodynamic function is related to the amount of viscous damping per unit length. The effective displaced fluid mass acts to increase the total effective mass of the system. This, in turn, decreases the resonant frequency and increases the amount of energy stored in the system which increases the quality factor. Increasing the viscous damping will also decrease the resonant frequency. However, increasing the viscous damping will decrease the quality factor.

2.3 Mode Shapes

In order to find the characteristics of laterally vibrating beams, the frequency spectrum of the deflection (the deflection as a function of excitation frequency) must be found from the equation of motion. First the mode shapes of the beam, or the shape of the beam at maximum deflection as a function of x, must be found. The frequency spectrum can then be found using the mode shapes and the equation of motion.

It can be assumed that the deflection in the lateral direction is sinusoidal with respect to time. Using separation of variables, the deflection can be given as

$$v(x,t) = V(x)e^{j\omega t} \qquad \textbf{(Eq. 2-10)}$$

where V(x) is the overall mode shape with respect to x (and not the velocity of the microcantilever). To solve for $V(x)$, it is recalled that any appropriately smooth function can be written as an infinite series of weighted orthonormal functions [117], or

$$V(x) = \sum_{i=1}^{\infty} C_i \phi_i(x) \qquad \textbf{(Eq. 2-11)}$$

where each mode has an amplitude of C_i and a particular mode shape $\phi_i(x)$. Any infinite set of orthogonal mode shapes could be used for $\phi_i(x)$. However, it is convenient to use the set of mode shapes that the microcantilever takes naturally when freely vibrating in a vacuum. These mode shapes satisfy the condition

$$\frac{d^4\phi_i(x)}{dx^4} = \beta_i^4 \phi_i(x) \qquad \textbf{(Eq. 2-12)}$$

where β_i is a constant defining the modes of operation of the microcantilever and is given by

$$\beta_i^4 = \frac{\rho_B b h \omega^2}{EI_{lat}}. \qquad \textbf{(Eq. 2-13)}$$

A general form of the solution to $\phi_i(x)$ is

$$\begin{aligned}\phi_i(x) = {} & D_1(\cos\beta_i x + \cosh\beta_i x) + D_2(\cos\beta_i x - \cosh\beta_i x) \\ & + D_3(\sin\beta_i x + \sinh\beta_i x) + D_4(\sin\beta_i x - \sinh\beta_i x)\end{aligned}. \qquad \textbf{(Eq. 2-14)}$$

where D_1, D_2, D_3,and D_4 are constants. Due to the orthogonality of the modes [118], the mode shapes will have the property such that

$$\int_0^L \phi_i(x)\phi_j(x)dx = 0 \;\; (\forall i \neq j)\,. \qquad \textbf{(Eq. 2-15)}$$

Because the microcantilever is clamped at x=0, each individual mode shape $\phi_i(x)$ must satisfy the following boundary conditions:

$$\phi_i(0) = 0 \qquad \textbf{(Eq. 2-16)}$$

$$\frac{d\phi_i(0)}{dx} = 0 \qquad \textbf{(Eq. 2-17)}$$

Since the microcantilever is free at $x=L$, there will be no bending moment or shear force at that point, thus:

$$\frac{d^2\phi_i(L)}{dx^2} = 0 \qquad \textbf{(Eq. 2-18)}$$

$$\frac{d^3\phi_i(L)}{dx^3} = 0 \qquad \textbf{(Eq. 2-19)}$$

From these four boundary conditions, the general form of the *i*th mode shape given by Eq. 2-14 can be rewritten as

$$\phi_i(x) = D_4\left(\frac{(\cos\beta_i x - \cosh\beta_i x)(\cos\beta_i L + \cosh\beta_i L) + (\sin\beta_i x - \sinh\beta_i x)(\sin\beta_i L - \sinh\beta_i L)}{(\sin\beta_i L - \sinh\beta_i L)}\right),$$

(Eq. 2-20)

Using the second and third derivatives of Eq. 2-14 with respect to x at $x=L$, β_i can be found as the infinite set of solutions to

$$(\cos\beta_i L \cosh\beta_i L) = -1\,. \qquad \textbf{(Eq. 2-21)}$$

The smallest solution for $\beta_i L$ is approximately equal to 1.8751. This value will be used for i=1, with each successively larger solution (4.6941, 7.8548, 10.9955, 14.1372…) assigned to successively higher integer values of i. These values are well-known [92], and converge to

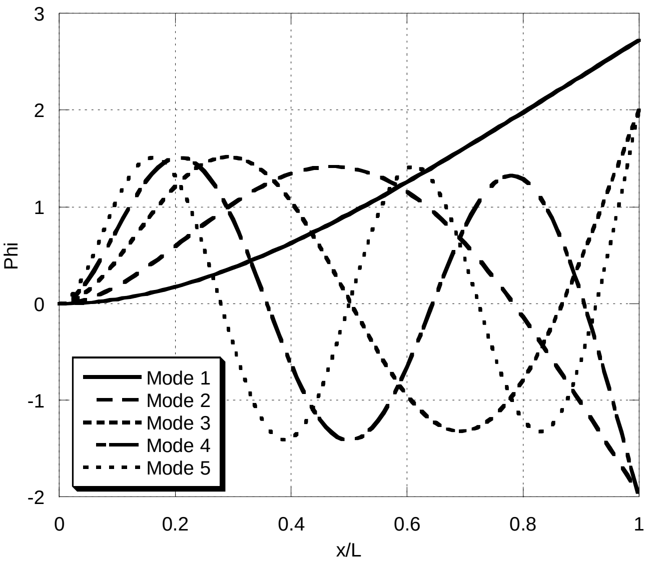

Figure 2-2. The first 5 mode shapes of a vibrating microcantilever using Eq. 2-20, $D_4=1$ and the β_i values found from Eq. 2-21.

$$\beta_i L \cong \frac{\pi}{2}(2i-1) \quad \forall i > 5. \qquad \textbf{(Eq. 2-22)}$$

The mode shapes $\phi_i(x)$ of each individual mode, *i*, can then be plotted as a function of normalized length (see Figure 2-2).

2.4 Mode Shape Amplitudes and Phases of Laterally Vibrating Microcantilevers in Viscous Liquid Media

The variables D_4 and C_i in Eqs. 2-11 and 2-14 are still unknown. The constant D_4 can be written in terms of C_i. From Eq. 2-10 it can be shown that

$$-g_{1,lat}\frac{\partial v(x,t)}{\partial t} = \frac{jg_{1,lat}}{\omega}\frac{\partial^2 v(x,t)}{\partial t^2}. \qquad \textbf{(Eq. 2-23)}$$

Using Eq. 2-23, Eq. 2-2 can then be rewritten as

$$EI_{lat}\frac{\partial^4 v(x,t)}{\partial x^4} - \left(\rho_B bh + g_{2,lat} - j\frac{g_{1,lat}}{\omega}\right)\omega^2\frac{\partial^2 v(x,t)}{\partial t^2} = F_y(x)e^{j\omega t}. \qquad \textbf{(Eq. 2-24)}$$

Equations 2-24 and 2-11 can be combined to give

$$\sum_{i=1}^{\infty} C_i \left((EI_{lat}) \frac{d^4\phi_i(x)}{dx^4} - \left(\rho_B bh + g_{2,lat} - j\frac{g_{1,lat}}{\omega} \right) \omega^2 \phi_i(x) \right) e^{j\omega t} = F_y(x) e^{j\omega t} .$$

(Eq. 2-25)

Canceling out the time dependency and using Eq. 2-12, Eq. 2-25 can be simplified to

$$\sum_{i=1}^{\infty} C_i \left((EI_{lat}) \beta_i^4 - \left(\rho_B bh + g_{2,lat} - j\frac{g_{1,lat}}{\omega} \right) \omega^2 \right) \phi_i(x) = F_y(x) .$$ **(Eq. 2-26)**

Both sides can be multiplied by $\phi_j(x)$ where C_j is the desired mode amplitude to be found. Eq. 2-26 then becomes

$$\sum_{i=1}^{\infty} \left(C_i \phi_i(x) \phi_j(x) \left((EI_{lat}) \beta_i^4 - \left(\rho_B bh + g_{2,lat} - j\frac{g_{1,lat}}{\omega} \right) \omega^2 \right) \right) = F_y(x) \phi_j(x) .$$

(Eq. 2-27)

Integrating both sides of Eq. 2-27 along the length of the microcantilever from zero to L, and using Eq. 2-15,

$$C_j \left((EI_{lat}) \beta_j{}^4 - \left(\rho_B bh + g_{2,lat} - j\frac{g_{1,lat}}{\omega} \right) \omega^2 \right) \int_0^L \phi_j(x)^2 \, dx = \int_0^L F_y(x) \phi_j(x) dx .$$

(Eq. 2-28)

Eq. 2-28 can then be rearranged to obtain C_j as

$$C_j = \frac{\int\limits_0^L F_y(x) \phi_j(x) dx}{\left(EI_{lat} \beta_j^4 - \left(\rho_B bh + g_{2,lat} \right) \omega^2 + j g_{1,lat} \omega \right) \int\limits_0^L \phi_j{}^2(x) dx} .$$

(Eq. 2-29)

C_j is a complex number, which indicates that the microcantilever's deflection is not always in-phase with the excitation. Eq. 2-29 can be rewritten as

$$C_j = \frac{\int\limits_0^L F_y(x)\phi_j(x)dx}{\sqrt{\left(EI_{lat}\beta_j^4-\left(\rho_B bh+g_{2,lat}\right)\omega^2\right)^2+\left(g_{1,lat}\omega\right)^2}\int\limits_0^L \phi_j^{\,2}(x)dx}\, e^{j\vartheta}$$

(Eq. 2-30)

where

$$\vartheta_j = \begin{cases} \tan^{-1}\left(\dfrac{-g_{1,lat}\omega}{(EI_{lat})\beta_i^4-\left(\rho_B bh+g_{2,lat}\right)\omega^2}\right) & , \quad \left((EI_{lat})\beta_j^4-\left(\rho_B bh+g_{2,lat}\right)\omega^2\right)>0 \\ \tan^{-1}\left(\dfrac{-g_{1,lat}\omega}{(EI_{lat})\beta_i^4-\left(\rho_B bh+g_{2,lat}\right)\omega^2}\right)-\pi & , \quad \left((EI_{lat})\beta_j^4-\left(\rho_B bh+g_{2,lat}\right)\omega^2\right)<0\,. \end{cases}$$

(Eq. 2-30a)

The deflection amplitude at the tip of the microcantilever as a function of frequency can then be found by substituting Eq. 2-30 into Eq. 2-11,

$$\left|V(L)\right| = \left|\sum_{i=1}^{\infty}\frac{\int\limits_0^L F_y(x)\phi_i(x)dx}{\sqrt{\left(EI_{lat}\beta_j^4-\left(\rho_B bh+g_{2,lat}\right)\omega^2\right)^2+\left(g_{1,lat}\omega\right)^2}\int\limits_0^L \phi_i^{\,2}(x)dx}\,\phi_i(L)\right|.$$

(Eq. 2-31)

From Eq. 2-31, the frequency spectrum of the microcantilever can be calculated. It is important to note that the excitation force per unit length, $F_y(x)$, can be any arbitrary force as a function of the position along the length of the microcantilever. If a tip force, is placed on the beam at $x=L$,

$$\int\limits_0^L F_y(x)\phi_i(x)dx = \int\limits_0^L F_{tip}\delta(L)\phi_i(x)dx$$

(Eq. 2-32)

where F_{tip} is the amplitude of the harmonic tip force. Eq. 2-32 can be simplified, such that

$$\int_0^L F_y(x)\phi_i(x)dx = F_{tip}\phi_i(L)\,. \qquad \textbf{(Eq. 2-33)}$$

The deflection amplitude of the tip of a laterally vibrating microcantilever in a viscous liquid medium, *V(L)*, excited using a tip force can then be found from Eq. 2-31 and 2-33 as

$$\left|V(L)\right| = \left|\sum_{i=1}^{\infty} \frac{F_{tip}\phi_i^{\,2}(L)}{\sqrt{\left(EI_{lat}\beta_j^4 - \left(\rho_B bh + g_{2,lat}\right)\omega^2\right)^2 + \left(g_{1,lat}\omega\right)^2}\int_0^L \phi_i^{\,2}(x)dx}\right|$$

(Eq. 2-34)

Normally, when operating around the resonant frequency of the *i*th mode, only the *i*th term in Eq. 2-31 is significant. This approximation will be investigated in chapter 4.

By investigating the lateral deflection as a function of the excitation frequency, the resonant frequency and quality factor of the microcantilever can be found. Using the resonant frequency and the quality factor, sensing characteristics such as the mass sensitivity can be found. In order to find the microcantilever's spectrum, all the terms in Eq. 2-31 must be known. The beam's density, ρ_B, and Young's modulus, *E*, are determined by the material or materials chosen for the microcantilever. For example, silicon's density and Young's modulus are 2330 kg/m^3 and 169 GPa (for the <110> direction), respectively [119]. The length, *L*, width, *b*, and thickness, *h*, of the microcantilever are determined during its fabrication. The excitation frequency, ω, is determined by the frequency of excitation of the transducers. The lateral excitation force per unit length F_y is determined by both the location of the transducers on the microcantilever and the amount of power used to excite it. The force per unit length, F_y, while difficult to estimate, only acts as a multiplier for the tip deflection. The resonant frequency and quality factor thus do not depend on the value of the excitation force. However, the force per unit length must still be small enough to assume a deflection smaller than any length scale of the microcantilever. The moment of inertia I_{lat}, the mode shape function ϕ_i, and the constant β_i, can be found by Eq. 2-1a, Eq. 2-20, and Eq. 2-21, respectively.

This leaves $g_{1,\mathrm{lat}}$ and $g_{2,\mathrm{lat}}$ as the only unknown quantities in Eq. 2-31. The values of $g_{1,\mathrm{lat}}$ and $g_{2,\mathrm{lat}}$ can be found from Eq. 2-4 and Eq. 2-5, respectively. Equations 2-4 and 2-5 require the frequency of excitation, dynamic viscosity and density of the medium, and the width of the beam, all of which are known. Equations 2-4 and 2-5 also require the real and imaginary parts of the hydrodynamic function, Γ_{lat}. The hydrodynamic function, Γ_{lat}, is the hydrodynamic force per unit length normalized to the amount of force per unit length it would take to excite fluid occupying a cylindrical volume with a diameter equal to the microcantilever's width to the same velocity as the microcantilever [85,102]. In order to find the characteristics of laterally vibrating beams, an expression for the hydrodynamic function of a laterally vibrating beam must be found. In the next chapter, the different hydrodynamic forces acting on laterally vibrating microcantilevers will be defined. An approximation of the hydrodynamic function for a laterally vibrating plate will be given. A numerical procedure for finding the precise value for the hydrodynamic function for particular values of the Reynolds number, Re, and aspect ratio, h/b will also be given. The simple expression for the hydrodynamic function of a laterally vibrating plate will then be mapped to the numerical results using a set of correction factors. The corrected expression for the hydrodynamic function can then be used with Eq. 2-31 to find characteristics of a laterally vibrating microcantilever in a viscous liquid medium.

3. Hydrodynamic Forces on Laterally Vibrating Microcantilevers in a Viscous Liquid Medium

3.1 Introduction

In order to evaluate the characteristics of a laterally excited microcantilever, the hydrodynamic forces acting on the vibrating microcantilever must be known. All hydrodynamic forces must first be defined. Using the equation of motion of the fluid, the hydrodynamic forces can be approximated using the steady state solution to Stokes' second problem [105]. This, in turn, will yield a simple analytical expression for the hydrodynamic function. However, this expression neglects the thickness and edge effects. The fluid can be modeled more accurately using a numerical procedure which accounts for these effects and the hydrodynamic forces on the cross-section of the microcantilever can be estimated. Stokes' solution can then be modified using a set of correction factors found from the numerical results to account for the edge effects and the effect of thickness. The corrected expression for Stokes' solution can then be used to find the viscous damping and effective displaced fluid mass per unit length as a function of the microcantilever's geometry and the Reynolds number. When used with the solution to the microcantilever's equation of motion, relevant vibration characteristics of the system can be found.

3.2 Hydrodynamic Forces

When a microcantilever is vibrating in an infinite viscous liquid medium (either in the in-plane or out-of-plane direction), the fluid acts to oppose the movement of the microcantilever, applying an opposing hydrodynamic force. However, this hydrodynamic force is not always applied perpendicularly to the surface of the microcantilever, as shown in Fig. 3-1.

Conceptually, the total hydrodynamic force is the sum of the hydrodynamic force perpendicular to the surface of the microcantilever, $F_{pressure}$, (also known as the pressure force), and a force parallel to the surface, F_{shear}, called the shear force. The shear force is proportional to the shear drag on the microcantilever [97,100]. The total hydrodynamic force can then be found as

$$F_{medium,lat} = F_{pressure} + F_{shear} . \qquad \textbf{(Eq. 3-1)}$$

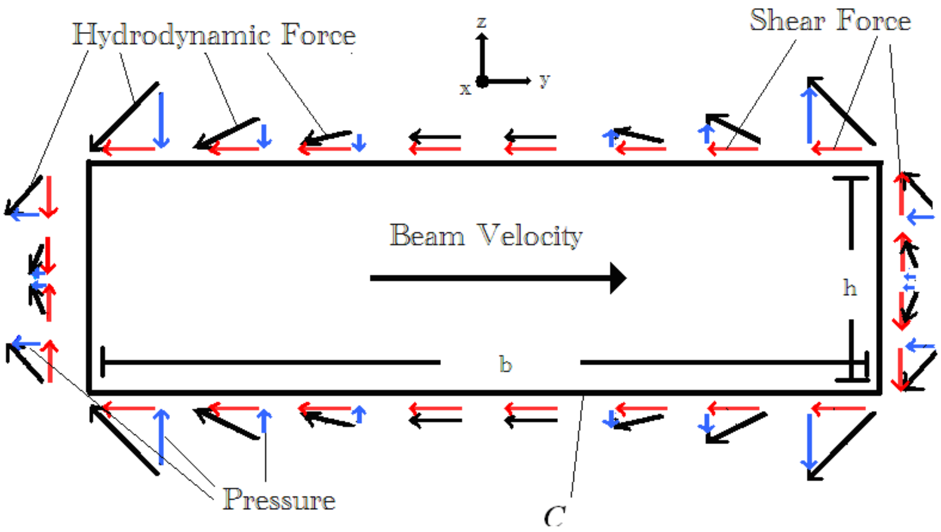

Figure 3-1. Hydrodynamic forces acting on the surfaces of a cross-section of a laterally vibrating microcantilever in fluid.

3.2.1 Pressure

The pressure is the force per unit area applied perpendicularly to the microcantilever’s surface by the fluid and is the dominant hydrodynamic force encountered when relatively thin microcantilevers are excited in the out-of-plane direction [97,100]. It is noted that the calculated hydrodynamic force on a transversely vibrating microcantilever based on Ref. 85 neglects the shear force and is still found to be in good agreement with experimental results found in the literature [85]. However, it must be noted that the pressure might not always be the dominant hydrodynamic force. For thin microcantilevers undergoing in-plane vibration in a viscous liquid medium, the shear force is expected to be larger than the pressure force. When a microcantilever is vibrating in a liquid medium, pressure from the medium is applied on all surfaces of the microcantilever. When the microcantilever is at rest and there is no net flow in the medium, the pressure applied on the microcantilever by the medium is the static pressure of the medium and is essentially uniform over the surface of the microcantilever. The forces in the y and z directions applied to the microcantilever by the static pressure will therefore cancel each other out.

When the microcantilever vibrates in the in-plane direction, the pressure incident on the surface of the microcantilever becomes both a function of time and position. The pressure must maintain a value higher than the medium’s vapor pressure; otherwise the medium will undergo cavitation and form vapor bubbles [101]. The total pressure is the sum of the static pressure and the dynamic pressure [101]. Since the total pressure can be lower than the static pressure, the dynamic pressure can be a negative quantity.

Due to the symmetry of the problem, the dynamic pressure should be symmetric with respect to the y axis and anti-symmetric with respect to the z axis [97]. All the forces in the z direction from the pressure cancel each other out due to its symmetry about the y axis. The hydrodynamic force from the pressure acting on the leading and trailing edges of the microcantilever will be equal. The total remaining hydrodynamic force per unit length from the pressure acting on the microcantilever is then twice that of the pressure acting on its leading edge, or

$$F_{pressure}(x) = 2\int_{-h/2}^{h/2} P(b/2, z)dz \qquad \textbf{(Eq. 3-2)}$$

where P is the pressure.

It is noted [97,102,107] that the pressure is partially out-of-phase with the velocity of the microcantilever. As indicated in chapter 2, the hydrodynamic force from the pressure will then contribute to both the effective displaced fluid mass and the damping of the system. The phase of the hydrodynamic force from the pressure will depend on the Reynolds number and the aspect ratio (*h/b*) of the microcantilever's geometry. When the Reynolds number increases (or the viscosity decreases), it is expected that the viscous damping will become negligible. The hydrodynamic force from the pressure can then be treated simply as an effective displaced fluid mass. Since the hydrodynamic force from the pressure only comes from the leading and trailing edges of the microcantilever, it is also expected that the pressure's effect on the microcantilever should become negligible as the aspect ratio of a laterally excited microcantilever goes to zero.

3.2.2 Fluid Shear

The shear stress of the fluid acting on the microcantilever is given by

$$\tau = \eta \frac{du}{dn} \qquad \textbf{(Eq. 3-3)}$$

where u is the velocity of the fluid in the vicinity of the fluid-beam interface and n is a coordinate in the direction normal to the surface [100]. Note that, unlike the pressure, when the dynamic viscosity, η, of the medium goes to zero the shear stress also goes to zero. The total shear force per unit length, F_{shear}, is the resultant of all shear stresses acting over the entire contour of the microcantilever's cross-section, or

$$F_{shear}(x) = \oint_C \tau d\lambda \qquad \textbf{(Eq. 3-4)}$$

where C is the contour running around the cross-section of the microcantilever.

The shear forces in the z direction will cancel each other out due to the symmetry of the problem about the y axis. The shear force in the y direction is a function of the area of the microcantilever's surfaces parallel to the direction of motion. For microcantilevers undergoing out-of-plane vibration, the shear force acts on the surface along the thickness of the microcantilever, which can safely be neglected as long as the width is not of the same order as the thickness [97]. When the microcantilever is vibrating in the in-plane direction, the shear force is applied to the top and bottom of the microcantilever. Due to the symmetry of the problem, the shear force acting on the top of the microcantilever will be the same as the shear force acting on the bottom. Thus, when the microcantilever is vibrating in the in-plane direction, the shear force per unit length can be calculated as

$$F_{shear}(x) = 2 \int_{-b/2}^{b/2} \tau(y, h/2)\, dy \qquad \textbf{(Eq. 3-5)}$$

Using Eqs. 3-2 and 3-5 in Eq. 3-1, the total hydrodynamic force per unit length on a rectangular microcantilever can be calculated, provided that the fluid velocity can be obtained. However, several approximations can be made depending on the dimension of the microcantilever. If the thickness is small enough, the pressure can be neglected and only the shear force will contribute to the hydrodynamic force. However, as will be shown in Section 3.4.3, the pressure force can remain significant under certain conditions, even when the microcantilever's width is much greater than its thickness. It will initially be assumed that the shear force is the dominant hydrodynamic force. This assumption will be investigated. The shear force is also partially out-of-phase with the velocity of the microcantilever, meaning that the shear force will also contribute to both the effective displaced fluid mass and the viscous damping of the system. Since the shear force is a function of the dynamic viscosity, both the effective displaced fluid mass and the damping from the shear force are expected to approach zero as the Reynolds number approaches infinity.

There have been several attempts to model the hydrodynamic forces acting on a microcantilever vibrating in the in-plane direction. When the microcantilever's thickness is small compared to its width, it can be approximated as a laterally vibrating ribbon. Stokes investigated the forces acting on an infinitely wide flat plate brought from rest to sinusoidal lateral vibration. This is commonly called Stokes' second problem [106]. The problem of a laterally vibrating ribbon can be reduced to the steady state solution of Stokes' second problem if the microcantilever under investigation is also quite wide relative to the boundary layer thickness of the fluid.

3.3 Stokes' Solution

The total hydrodynamic force per unit length can be found from first solving the fluid's equation of motion given by Eq. 2-6, which is repeated here for convenience.

$$\rho_L \frac{d\vec{u}}{dt} = -\nabla P + \eta \nabla^2 \vec{u} \,. \qquad \textbf{(Eq. 3-6)}$$

$\vec{u}$ is the velocity field of the fluid at all points, P is the pressure, and ρ_L and η are the density and dynamic viscosity of the fluid, respectively. If the velocity field in the fluid is known everywhere, both the pressure and shear force per unit length incident on the microcantilever can be found. Dividing both sides by the fluid density, taking the curl of each side to remove the pressure dependence, and assuming the fluid velocity to be sinusoidal, the Navier–Stokes equation can be modified to

$$j\omega\left(\nabla \times \vec{u}\right) = \frac{\eta}{\rho_L} \nabla^2 \left(\nabla \times \vec{u}\right). \qquad \textbf{(Eq. 3-7)}$$

In order to solve the above equation, the stream function, $\vec{\psi}\,(x,y,z;t)$, will be introduced and is the function that quantifies the amount of fluidic flux passing in between two points [102]. The contour of constant values for $\vec{\psi}$ is known as a stream line which is always parallel to the direction of fluidic flow. Mathematically, the stream function can be defined in terms of the velocity field as

$$\vec{u} = \nabla \times \vec{\psi} \qquad \textbf{(Eq. 3-8)}$$

and, likewise, the curl of the velocity field as

$$\nabla \times \vec{u} = \nabla^2 \vec{\psi} \qquad \textbf{(Eq. 3-9)}$$

Since only the cross-section of the fluid and microcantilever in the *y-z* plane is under consideration and the assumption is made that the microcantilever is long enough so that the variations in the fluid velocity in the x direction are small, only the x component of the stream function will be considered non-zero. ψ_x will be written as ψ for notation convenience. Eq. 3-7 can then be rewritten as

$$\nabla^2\left(\nabla^2\psi\right)-\alpha^2\left(\nabla^2\psi\right)=0 \qquad \textbf{(Eq. 3-10)}$$

where

$$\alpha=\sqrt{\frac{j\omega\rho_L}{\eta}} \qquad \textbf{(Eq. 3-10a)}$$

The general solution to Eq. 3-10 is difficult to obtain. If $b>>h$, only the shear force can be considered significant. If it is also assumed that the stream function is constant in the y direction, the general solution to Eq. 3-10 is given by

$$\psi(z;t)=A_1+A_2z+B_1e^{-\sqrt{\frac{\rho_L\omega}{2\eta}}(1+j)z}+B_2e^{\sqrt{\frac{\rho_L\omega}{2\eta}}(1+j)z}\,. \qquad \textbf{(Eq. 3-11)}$$

where A_1, A_2, B_1 and B_2 are amplitude terms that may depend on time. Making the assumption that the stream function is not dependent on y means that the anticipated stress singularities on the edge of the microcantilever (called edge effects) are neglected, making the implicit assumption that the microcantilever is infinitely wide. These singularities have been previously noted in the literature [97,102] and are significant when the Reynolds number is low. Thus, this procedure is only valid when Re>>1.

From Eq. 3-8, the velocity of the fluid in the y direction can then be found as

$$u_y=\frac{\partial\psi}{\partial z}=A_2+\sqrt{\frac{\rho_L\omega}{2\eta}}(1+j)\left[B_2e^{\sqrt{\frac{\rho_L\omega}{2\eta}}(1+j)z}-B_1e^{-\sqrt{\frac{\rho_L\omega}{2\eta}}(1+j)z}\right] \qquad \textbf{(Eq. 3-12)}$$

While, in practice, the microcantilever is in a finite volume cell, it is normally assumed that the microcantilever is operating in an infinitely bound medium. Thus, as |z| goes to infinity, the velocity must approach zero, implying that $A_2=0$. Likewise, by only considering the half space of the fluid above the microcantilever (since the problem is symmetric about the *x*-*y* plane), it is found that $B_2 = 0$. Thus, Eq. 3-11 and Eq. 3-12 become

$$\psi(z;t) = A_1 + B_1 e^{-\sqrt{\frac{\rho_L \omega}{2\eta}}(1+j)z}, \qquad \textbf{(Eq. 3-13)}$$

$$u_y = -\sqrt{\frac{\rho_L \omega}{2\eta}}(1+j)B_1 e^{-\sqrt{\frac{\rho_L \omega}{2\eta}}(1+j)z}. \qquad \textbf{(Eq. 3-14)}$$

It has been assumed that fluid in contact with the microcantilever will have the same velocity as the microcantilever. Using the no-slip boundary condition at $z=h/2$, for small thicknesses,

$$U_0 e^{j\omega t} = -\sqrt{\frac{\rho_L \omega}{2\eta}}(1+j)B_1. \qquad \textbf{(Eq. 3-15)}$$

where U_0 is the amplitude of the excitation velocity. Solving for B_1 and applying symmetry, the velocity in the upper half-space of the fluid is then found as

$$u_y = U_0 e^{j\omega t} e^{-\sqrt{\frac{\rho_L \omega}{2\eta}}(1+j)z}. \qquad \textbf{(Eq. 3-16)}$$

Using Eq. 3-3, the shear stress on the top face of the microcantilever can then be written as

$$\tau = -U_0 e^{j\omega t}\sqrt{\frac{\eta \rho_L \omega}{2}}(1+j) \qquad \textbf{(Eq. 3-17)}$$

and the total force per unit length can be found using Eq. 3-5 as

$$F_{medium,lat,Stokes} = -2U_0 e^{j\omega t} b\sqrt{\frac{\eta \rho_L \omega}{2}}(1+j) = -2U_0 e^{j\omega t}\eta\sqrt{2\,\mathrm{Re}}(1+j). \qquad \textbf{(Eq. 3-18)}$$

Equation 3-18 indicates that, when edge effects and pressure forces are neglected, the total hydrodynamic force is 45° out of phase with the velocity, linearly dependent on both the width and the amplitude of the excitation velocity U_0, while dependent on the square-root of the product of dynamic viscosity, liquid density and excitation frequency. The hydrodynamic function can, in turn, be found from the total hydrodynamic force per unit length as

$$\Gamma_{lat,Stokes}(\mathrm{Re}) = \frac{F^{*}_{medium,lat,Stokes}}{j\pi\eta \mathrm{Re} U_0 e^{-j\omega t}} = \frac{2\sqrt{2}}{\pi\sqrt{\mathrm{Re}}}(1+j)\,. \qquad \textbf{(Eq. 3-19)}$$

As stated in chapter 2, the hydrodynamic function is the total hydrodynamic force per unit length normalized to the amount of force per unit length it would take to excite fluid occupying a circular cylindrical volume with a diameter equal to the microcantilever's width to the same velocity as the microcantilever [85,102]. Equation 3-19 indicates that, for the fluid resistance predicted by Stokes, the real and imaginary parts of the hydrodynamic function are equal. Also note, as stated in chapter 2, the hydrodynamic function is a function of δ/b. Equation 3-19 can give a good approximation for the hydrodynamic forces from the fluid shear if the edge effects are negligible, which happens when Re>>1. However, it does not account for the effects of thickness. In order to investigate the edge and thickness effects on both the hydrodynamic forces and on the device's characteristics of interest, a method that takes into account all the hydrodynamic forces must be found.

3.4 Numerical Evaluation of the Hydrodynamic Forces

In order to account for both the edge and thickness effects, a set of correction factors will be found for Eq. 3-19 using results from finite element analysis (FEA). Finite element analysis, also called the finite element method (FEM), is a useful technique used to simulate the behavior of complicated systems. FEA is based on discretizing of larger systems into smaller, less complicated systems [120]. Initially developed to model beams and trusses [121], FEA has been used to model problems in many different fields, such as electromagnetism, fluidics, and thermodynamics [120]. FEA finds field quantities (e.g., displacements, stresses) by attempting to minimize the equations of equilibrium [122]. In the case of fluid flows the fluid velocities in the medium are obtained from the conservation of momentum principle, and the pressure is obtained using the conservation of mass principle.

The commercially available FEA package ANSYS 11.0 was utilized to simulate the hydrodynamic forces acting on the cross-section of a laterally vibrating rigid bar of rectangular cross-section. First, the simulation procedure is defined and an arrangement of finite fluid elements, called a mesh, is produced. These meshes are then tested to see if they produce a convergent solution for the hydrodynamic forces. Once a converged solution is obtained, the hydrodynamic force is extracted as a function of both the Reynolds number, Re, and the aspect ratio, *h/b*. The numerical results can then be compared to known hydrodynamic forces for special cases, such as the laterally vibrating ribbon at large Re values.

3.4.1 Simulation Procedures

The first step in defining the mesh was to choose the type of fluid elements to be used. There are many different fluid elements available in ANSYS. FLUID141, the 2-D fluid-thermal element, was chosen because it was one of the elements available that incorporated the viscous shear force of the fluid. A two-dimensional mesh of triangular elements was defined using FLUID141 elements with the microcantilever’s cross-section represented as a vibrating rectangular boundary condition. A 2-D mesh was chosen over a 3-D mesh as the number of elements needed to produce a convergent solution for the hydrodynamic forces using a 3-D mesh was found to be computationally prohibitive. Using a two-dimensional model of the fluid surrounding a rigid vibrating microcantilever’s cross-section (see Fig. 3-1) has proved to be an accurate approximation in previous attempts at finding the hydrodynamic forces [102,105]. Modeling the effects of the length or the deformation of the microcantilever’s cross-section on the hydrodynamic function is also outside of the scope of this investigation.

Two boundary conditions were placed on the mesh. A lateral sinusoidal velocity was imposed on the cross-section, and a zero displacement and zero pressure boundary condition was placed on the outer boundary. This violated the assumption of an infinitely large operating medium, causing the hydrodynamic forces to become dependent on the total domain size. If the outer boundary of the mesh is placed very far away from the vibrating cross-section, this dependence becomes negligible. However, the number of elements needed to define the mesh (for a fixed element size) increases as a function of the square of the mesh size. Estimating the velocity near the edge of the model is not as important as estimating the velocity near the vibrating cross-section; thus a tapering of element sizes was employed. Smaller elements were placed closer to the cross-section and larger elements (coarser mesh) placed near the outer boundary. Two regions in the fluid model were used, as shown in Fig. 3-2.

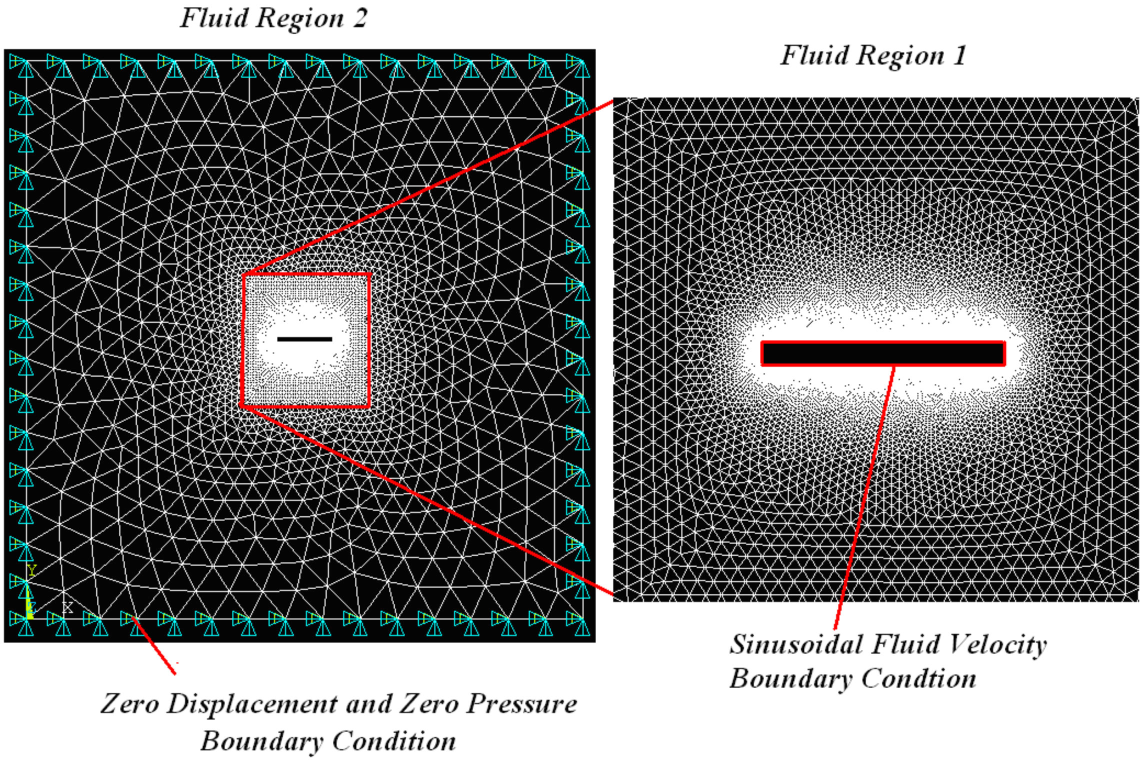

Figure 3-2. A finite element mesh used to model the hydrodynamic forces acting on the cross-section of a laterally vibrating beam with an aspect ratio of 1/10 in fluid. The mesh has a higher element density near the vibrating cross-section and has a zero displacement and pressure boundary condition placed on the outer boundary.

The first region was a square centered on the cross-section with a width and thickness of twice the width of the cross-section. The width of the cross-section can be set to any arbitrary distance as long as the excitation frequency and thickness produce the desired Reynolds number and aspect ratio. For the majority of the simulations run, the width of the cross-section was kept at 20 μm. However, the width was set to 10 μm and 40 μm for two sample test cases, while the Reynolds number and the aspect ratio were maintained constant. The numerical results of the hydrodynamic function were found to be nearly identical (within 1%). The assumption was then made that the numerical results for the hydrodynamic function did not depend on the size of the cross-section as long as the Reynolds number and aspect ratio remain constant.

The elements were triangular in shape, as indicated above, and defined via a free-mesh of the area from the fluid-beam interface to the border of the first region. The size of the elements in the first region was graded from a node spacing of 33.33 nm (600 nodes along the width) when the elements were placed along the cross-section to 1.33 μm (40 times larger) when the elements were placed on the outer boundary of region 1.

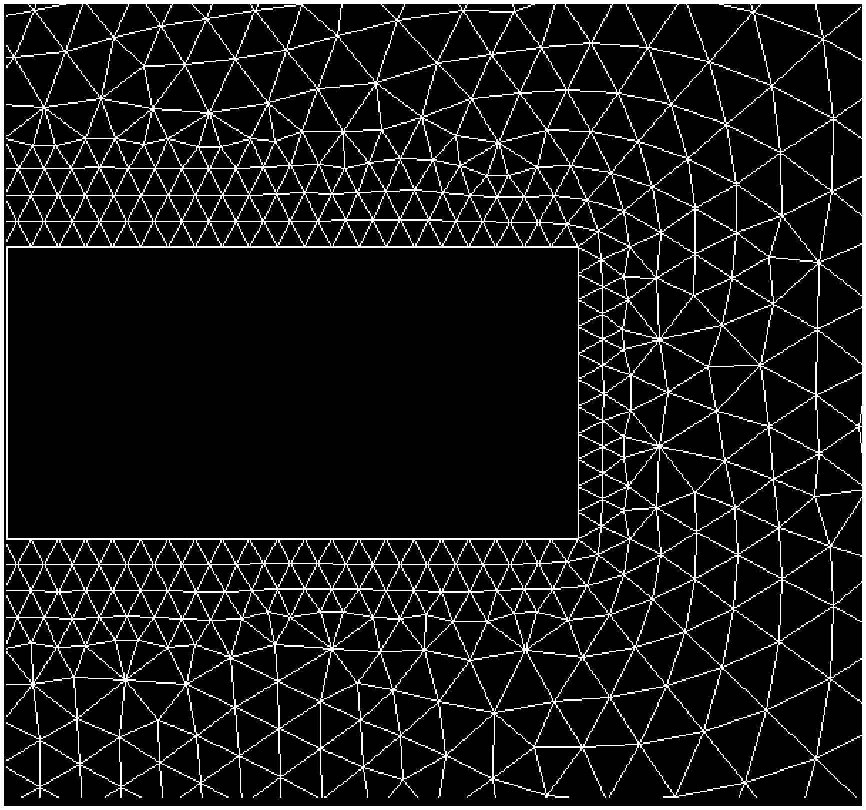

Figure 3-3. The mesh of the fluid defined near the right side of a beam cross-section with an aspect ratio of ~1/56.

This is roughly 44 times larger than the largest boundary layer thickness considered in this work. The elements in the second region were also created via a free mesh of triangular elements, graded in size from a minimum node spacing of 1.33 μm along the interface of the two fluid regions to a node spacing of 13.33 μm along the outer edge of the total mesh. The velocity gradient near the fixed outer boundary is very small, such that the velocity found near (within a few elements) the outer boundary was less than 1% of the applied velocity. This is expected as the velocity should be zero on the outer boundary. It is then assumed that the overall fluid mesh volume is large enough to serve as an appropriate approximation of an infinite medium.

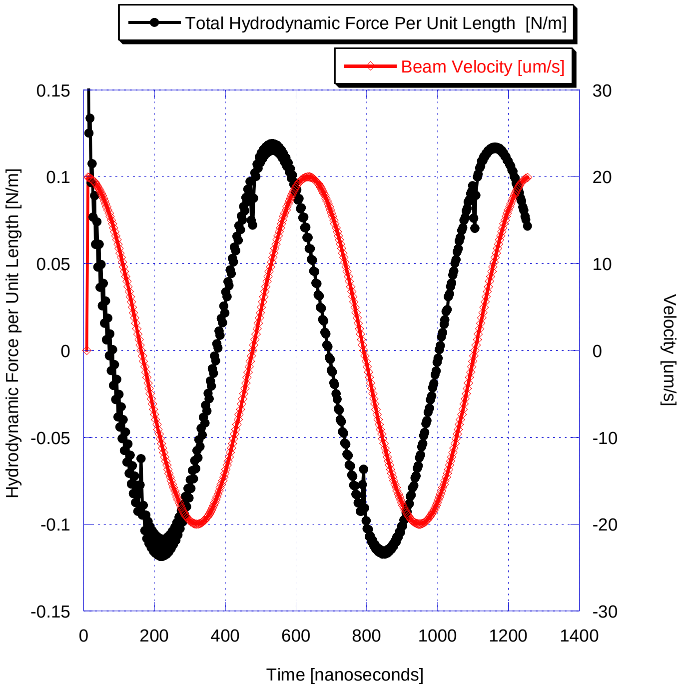

Figure 3-4. The simulated hydrodynamic force per unit length acting on the top and left hand side of a cross-section of a laterally vibrating microcantilever in water (b=20 μm, h/b=1/10, Re=1000) compared to the velocity of the cross-section.

Figure 3-4 shows a sample result of the simulated total force per unit length over the top and right side of the cross-section as a function of time. Note the phase offset between the force per unit length and the velocity. The force per unit length of a microcantilever undergoing only viscous damping would have no phase offset with respect to the velocity. The force per unit length of a microcantilever only undergoing the effects of displaced fluid mass would lag the velocity by 90°. For the configuration used to produce the results in Fig. 3-4 (h/b= 1/10, Re=1000), the force per unit length lags the velocity by ~53.6°, which means that in this case the displaced mass is slightly larger than the viscous damping.

The pressure and shear force can be investigated separately. Instead of finding the shear force, ANSYS calculates the wall shear stress (the total shear force distributed over the contour), as shown in Fig. 3-5. The wall shear stress is always found as a positive quantity. The wall shear stress can be corrected to the shear force by inverting its sign every half cycle. Numerical discontinuities affect the shear force near those time values at which the imposed velocity is zero. These discontinuities are artifacts of the mesh density and decrease when the mesh density is increased.

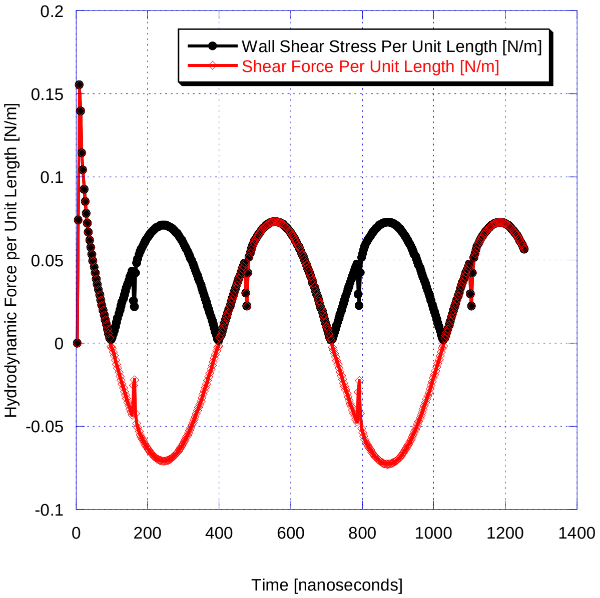

Figure 3-5. The wall shear stress and the shear force per unit length acting on a 20 μm wide microcantilever in water (*b*=20 μm, *h/b*=1/10, Re=1000).

Figure 3-6 shows the pressure and shear force per unit length acting in the lateral (*y*) direction compared to the overall hydrodynamic force per unit length acting in the lateral direction. The total hydrodynamic force per unit length is the sum of the pressure and shear forces per unit length. Note that they both have different phase offsets, which means that (in this case) the shear force contributes more to the viscous damping than the pressure force and the pressure force contributes more to the displaced mass than the shear force. It is interesting to note for this aspect ratio (*h/b*=1/10) that the magnitude of the pressure force per unit length is about the same as that of the shear force per unit length even though the pressure acts on a surface that is only one tenth of the size that the shear force acts on. The pressure and shear forces per unit length were found at 200 different times per cycle over two cycles. More cycles could be used, but this increases the amount of computation time needed. Investigating the predicted amplitude and phase as a function of time, all transient effects (for the range of aspect ratios and Reynolds numbers in this investigation) were found to be negligible within the first cycle.

The numerical results had noise. In order to eliminate this noise, the data is smoothed by using the average of the current and prior time instant's result. This averaging introduces a half time-step phase offset in the total force per unit length. When finding the phase offset between the force per unit length and the velocity using the averaged data, this half a time-step phase offset must be taken into account.

The hydrodynamic function is found next after calculating the magnitude and phase of the total hydrodynamic force per unit length. The magnitude of the hydrodynamic force per unit length is found by doubling the maximum value of the force per unit length on the top and right-hand side of the cross-section over the second cycle.

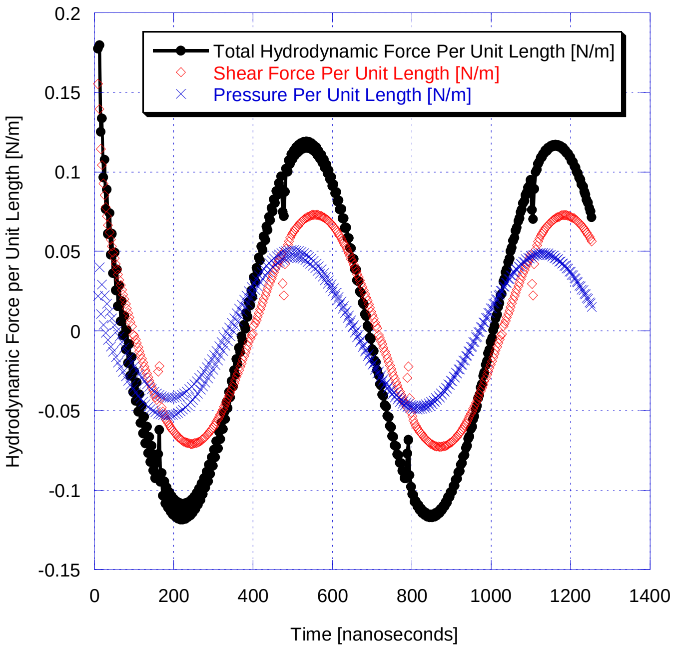

Figure 3-6. The simulated hydrodynamic force per unit length acting on the top and right side of a laterally vibrating microcantilever in water (b=20 μm, h/b=1/10, Re=1000). Also shown are the pressure force per unit length from the thickness and the shear force per unit length from the width.

The magnitude is doubled due to the symmetry of the problem, as the total force per unit length is twice that of the force per unit length acting on the top and right-hand side. The maximum value of the force per unit length over the first cycle still has transient effects from starting the microcantilever from rest, thus the maximum value from the second cycle is used.

The phase offset could be found by using the time difference between the zero crossings of the force per unit length and velocity. However, the values for the real and imaginary parts of the hydrodynamic function are very susceptible to small variations in the phase offset caused by variations in the numerical data. For example, if the total hydrodynamic force per unit length lagged the velocity by 89.8°, a 0.1° variation in the phase offset would cause a 50% variation in the estimated value of the imaginary part of the hydrodynamic function. This is an extreme example. However, the phase will converge to 90° as the Reynolds number converges to infinity. Thus, there is a need for a more accurate method of finding the phase offset. Using trigonometric identities, it is known that [123]

$$\begin{aligned} &u_{\max}\cos(\omega t)F_{medium,lat,\max}\cos(\omega t+\theta)= \\ &\frac{1}{2}u_{\max}F_{medium,lat,\max}(\cos(2\omega t+\theta)+\cos(-\theta)). \end{aligned} \qquad \textbf{(Eq. 3-20)}$$

Multiplying the velocity by the force per unit length produces a sinusoid with twice the frequency and an amplitude offset of $\cos(-\theta)$. The average phase offset over the second cycle can then be found as

$$\theta_{average} = -\cos^{-1}\left(\sum_{i=200}^{400}\left(\frac{2u(i)F_{medium,lat}(i)}{200u_{\max}F_{medium,lat,\max}}\right)\right). \qquad \textbf{(Eq. 3-21)}$$

Once the magnitude and phase of the hydrodynamic force per unit length are found, the hydrodynamic function can be determined as

$$\Gamma_{lat,Stokes}(\mathrm{Re}, h/b) = \frac{F_{medium,lat,\max} e^{j(\omega t - (\theta_{average} - 0.005\pi))}}{j\pi\eta \,\mathrm{Re}\, u_{\max} e^{j\omega t}} . \qquad \textbf{(Eq. 3-22)}$$

It is noted again that the hydrodynamic function is the hydrodynamic force per unit length normalized to the amount of force per unit length it would take to excite fluid of a cylindrical cross-section, with a diameter of the microcantilever's width, to the velocity of the microcantilever. The estimated phase is shifted by 0.005π radians (0.9°, or half a time step) to account for the two-point averaging of the pressure and shear force per unit length.

3.4.2 Determining the Mesh Density

The mesh density must be tested to ensure that it is high enough to produce a good estimate of the hydrodynamic forces. As the mesh density is increased, the estimated hydrodynamic function should converge to a particular value. The density of the elements in the mesh depends on the node spacing of the boundaries. The node spacing on the interface of the two fluid regions is 40 times greater than the node spacing on the microcantilever's surface. The node spacing on the outer boundary is 10 times larger than the node spacing on the interface of the two fluid regions. Finally, the node spacing along the thickness of the microcantilever's cross-section is approximately equal to the node spacing on the width. Thus, by increasing the number of nodes along the width of the microcantilever's cross-section, the density of the entire mesh increases. For example, doubling the number of points along the width roughly quadruples the number of elements used in the simulation. If there are not enough elements used in the simulation, numerical artifacts such as those shown in Fig. 3-4 will grow larger and the error in the estimation of the total hydrodynamic force per unit length will increase, especially due to inaccuracies near the corners of the beam's cross-section.

Six different meshes were created by varying the number of nodes along the width of the microcantilever's cross-section. The number of nodes used along the width of the microcantilever's cross-section in each of the 6 meshes was 100, 200, 300, 400, 600, and 800. This varies the number of elements used in the simulation from around 1000 to around 80,000. These 6 meshes were used to simulate the nine different combinations of aspect ratios and Reynolds numbers shown in Table 3-1. Eight different aspect ratios were investigated in this work ranging from ~1/56 (or $10^{-1.75}$) to 1 with an increment of 0.25 on a logarithmic scale. This allows for smaller aspect ratios to be investigated more thoroughly. Simulating an aspect ratio of 1/100 was attempted, but the number of elements required to produce a convergent solution (based on the difference between the numerical results from the two highest mesh densities) was too high. The 13 different Reynolds numbers investigated in this work range from 10 to 10,000, also with an increment of 0.25 on a logarithmic scale. While the Reynolds numbers normally considered for transversely vibrated microcantilevers range from 1 to 1000, laterally excited microcantilevers have larger resonant frequencies and Reynolds numbers.

Aspect Ratio (*h/b*)	1	1	1	1/10	1/10	1/10	1/56	1/56	1/56
Reynolds Number (Re)	10	316.23	10000	10	316.23	10000	10	316.23	10000

Table 3-1. Aspect ratios and Reynolds numbers used to test solution convergence.

Thus, the practical range for Reynolds numbers of laterally vibrating microcantilevers is an order of magnitude higher than those of transversely vibrating microcantilevers. There are then 108 different combinations of aspect ratios and Reynolds numbers investigated in this work.

Figure 3-7 plots the real and imaginary parts of the hydrodynamic function for an aspect ratio of 1/10 and a Reynolds number of 10,000 as a function of the number of elements used. Also plotted is the estimate of the real and imaginary hydrodynamic functions found from Eq. 3-19. Only one line is plotted as Stokes' solution assumes that the real and imaginary parts of the hydrodynamic function to be equal. The discrepancy between the numerical solution and Stokes' solution is due to the edge effects and the effect of thickness.

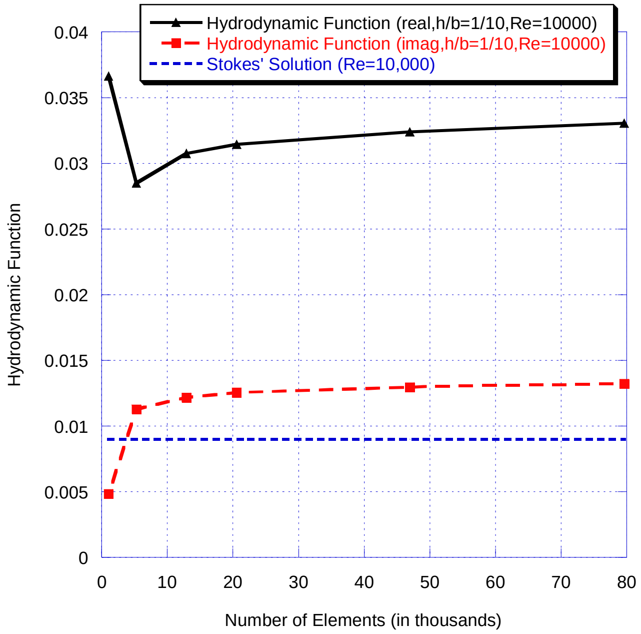

Figure 3-7. The real and imaginary parts of the hydrodynamic function for a laterally vibrating microcantilever (*h/b*=1/10, Re=10,000) as a function of the number of fluid elements used. Also plotted is Stokes' solution for Re=10,000.

Note that the solution for the hydrodynamic function converges when the number of elements used increases. The same trend was seen in all nine combinations of aspect ratios and Reynolds numbers. The second highest mesh size (600 points along the width of the cross-section) was chosen as a convergent mesh, as seen in Fig 3-3. The values for the hydrodynamic functions using the 600 node mesh and the 800 node mesh can be compared and given in terms of the percentage difference. This percentage difference will give a measure of how close the estimation of the hydrodynamic force per unit length is to the convergent value. Ideally, there should be zero difference in the two hydrodynamic functions found from both meshes. However, minimal differences are acceptable.

The largest percentage difference between these two meshes for the nine different aspect ratios and Reynolds numbers investigated was 5.19% for the real part of the hydrodynamic function and 2.87% for the imaginary part of the hydrodynamic function. The largest differences were found for microcantilevers with aspect ratios of ~1/56. This is expected, as thinner microcantilevers require a higher number of elements to accurately model the forces along the thickness. For example, a microcantilever with an aspect ratio of ~1/56 with 600 nodes along the width of the microcantilever’s cross-section only has 10 nodes along its thickness. Increasing the number of overall elements by ~32,000 only increases the number of nodes on the thickness by 4. The highest percentage difference for the real part of the hydrodynamic function was found for the highest Reynolds number used (Re=10,000), while the highest percentage difference for the imaginary part was for the lowest Reynolds number used (Re=10). This is also expected because, as the Reynolds number increases, the hydrodynamic force per unit length along the thickness (the pressure) becomes more out-of-phase with the velocity. Errors in estimating this force per unit length would then cause a larger error in estimating the real part of the hydrodynamic function compared to the imaginary part when the Reynolds number is large (Re>>1). The other combinations of aspect ratios and Reynolds numbers have differences in the real and imaginary parts of the hydrodynamic function ranging from as high as 2.81% to as low as 0.03%, as shown in Table 3-2. While there may be some issues with convergence for very thin microcantilevers, generally the hydrodynamic function is convergent when using the chosen mesh.

Another way of determining whether the mesh's density is high enough is to simulate the hydrodynamic forces acting on a transversely vibrating microcantilever and compare the results to the known forces found from the literature. The hydrodynamic function of a transversely vibrating microcantilever is well-known and defined in the literature in the case of a zero thickness ribbon as [85]

$$\Gamma_{trans}(\mathrm{Re}) = \Omega(\mathrm{Re})\left(1 + \frac{4jK_1(-j\sqrt{j\,\mathrm{Re}})}{\sqrt{j\,\mathrm{Re}}\,K_0(-j\sqrt{j\,\mathrm{Re}})}\right) \qquad \textbf{(Eq. 3-23)}$$

Aspect Ratio (h/b)	1	1	1	1/10	1/10	1/10	1/56	1/56	1/56
Reynolds Number (Re)	10	316.23	10000	10	316.23	10000	10	316.23	10000
Percentage Difference in $\Gamma_{R,lat}$ (Re, h/b)	-0.43%	0.85%	0.15%	1.59%	1.98%	2.02%	2.46%	2.81%	5.19%
Percentage Difference in $\Gamma_{I,lat}$ (Re, h/b)	-1.34%	0.43%	1.14%	2.00%	0.03%	1.86%	2.87%	1.70%	1.50%

Table 3-2. The percentage difference in the real and imaginary parts of the hydrodynamic function using the two finest meshes as a function of aspect ratio and Reynolds number.

where K_0 and K_1 are modified Bessel functions of the third kind and the Ω(Re) function is a correction function that maps the hydrodynamic function for a microcantilever of circular cross-section to that of an infinitely thin transversely vibrating microcantilever, and is defined in Ref. 85.

Figure 3-8 shows the simulated real and imaginary parts of the hydrodynamic function of a transversely vibrating microcantilever with an aspect ratio of ~1/56 over a range of Reynolds numbers. The numerical results can be compared to the results given by Eq. 3-23 by investigating the absolute percent difference, or

$$\% \,|\, Diff_{real} \,| = \frac{|\, \Gamma_{trans,real}(\mathrm{Re}) - \Gamma_{trans,FEA,real}(\mathrm{Re}, 1/56) \,|}{\Gamma_{trans,real}(\mathrm{Re})} * 100\% \qquad \textbf{(Eq. 3-24)}$$

and

$$\% \,|\, Diff_{imag} \,| = \frac{|\, \Gamma_{trans,imag}(\mathrm{Re}) - \Gamma_{trans,FEA,imag}(\mathrm{Re}, 1/56) \,|}{\Gamma_{trans,imag}(\mathrm{Re})} * 100\% \qquad \textbf{(Eq. 3-25)}$$

The real part of the hydrodynamic function calculated using the mesh has on average a 2% absolute percent difference with the values found from Eq. 3-23. The numerical results range from 1.6% lower than the values found from Eq. 3-23 when Re = 10 to 4.3% higher than the values found from Eq. 3-23 when Re = 10,000. The imaginary part of the hydrodynamic function was on average 7.7% lower than the values found from Eq. 3-23, ranging from 5.4% lower when Re = 10 to 10.3% lower when Re = 3162. This difference is most likely due to the assumption of zero thickness made in Ref. 85 when Eq. 3-23 was derived. The work done in Ref. 97 shows that the viscous damping actually decreases and the displaced mass increases when the thickness for a transversely vibrating microcantilever is increased until the aspect ratio is larger than 1/10.

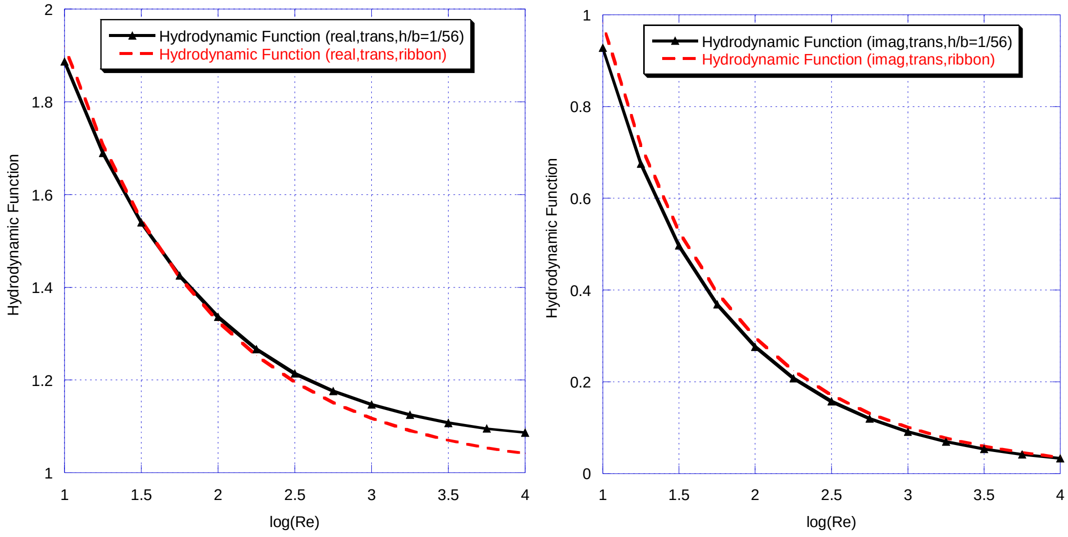

Figure 3-8. The real (left) and imaginary (right) parts of the simulated hydrodynamic function of a transversely vibrating microcantilever with an aspect ratio of ~1/56 as a function of Reynolds number compared to the hydrodynamic function given by Eq. 3-23.

Specifically, the real part of the hydrodynamic function should converge to a value of 1.04 for *h/b*=1/56. There could also still be some difference coming from the numerical modeling. However, the trends in the simulated hydrodynamic function are close enough to indicate that the chosen mesh is a good approximation of the operational medium.

3.4.3 Results of the Numerical Simulation

Figure 3-9 shows the real and imaginary parts of the hydrodynamic function of a laterally vibrating microcantilever as a function of the Reynolds number and aspect ratio using the procedure described in section 3.4.1 using the mesh chosen (an example of which is shown in Fig. 3-2) in section 3.4.2. Also shown in Fig. 3-9 is the thickness-independent Stokes' solution which is given in section 3.3. Note that the real part of the hydrodynamic function converges to Stokes' solution as the thickness goes to zero. The imaginary part of the hydrodynamic function also converges to Stokes' solution as the thickness goes to zero when the Reynolds number is large (Re>>1). For small Reynolds numbers, the edge effects become significant, causing additional viscous damping forces which are not accounted for in Stokes' solution. The same effect is present for the real part of the hydrodynamic function; however the magnitude of the edge effects is not as large. It can be seen from Fig. 3-9 that Stokes' solution diverges from the numerical results when the microcantilever's aspect ratio is increased or the system's Reynolds number is increased. Over the range of Reynolds numbers and aspect ratios investigated, there is a difference of 10% or greater between Stokes' solution and both the real and imaginary numerical results. If the thinnest aspect ratio (1/56) is not considered, this difference increases to 17% or more.

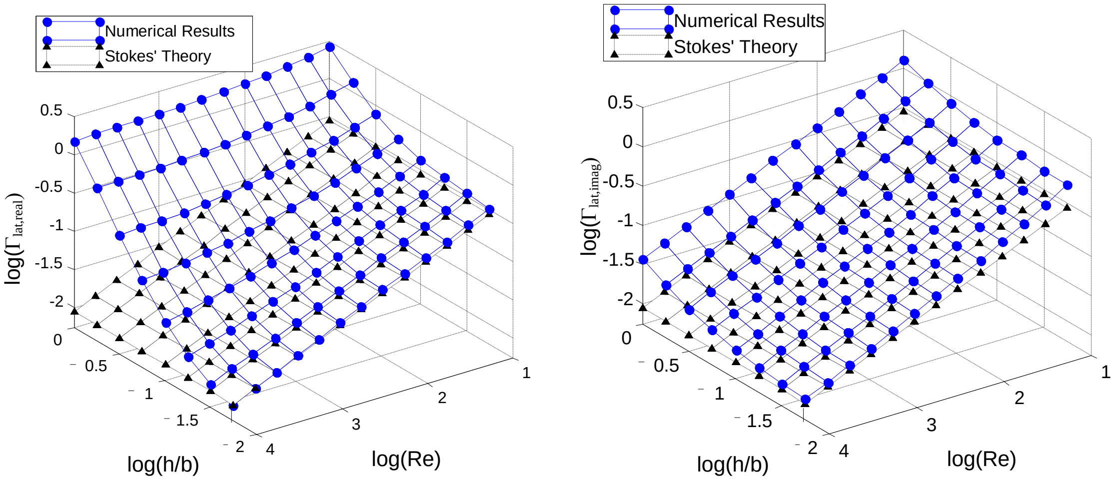

Figure 3-9. The real (left) and imaginary (right) parts of the hydrodynamic function for a laterally vibrating beam calculated using FEA as a function of *h/b* and Re compared to the results for the hydrodynamic function found using Stokes' theory, which are independent of *h*/*b*.

Figure 3-10 shows the results of the real and imaginary parts of the hydrodynamic function for *h/b*=~1/56 compared with the approximation of the hydrodynamic function found using Stokes' solution. The results from Ref. 97, which uses a numerical technique similar to that of Ref. 102, for an infinitely thin laterally vibrating microcantilever are also shown. The difference between Stokes' solution and the results from Ref. 97 is due to Ref. 97 accounting for edge effects.

The real and imaginary parts of the hydrodynamic function calculated for a laterally vibrating microcantilever using an aspect ratio of 1/56 still diverges from Stokes' solution by as much as 16.8% and 93.6%, respectively. The largest difference in the hydrodynamic function occurs for the smallest Reynolds number.

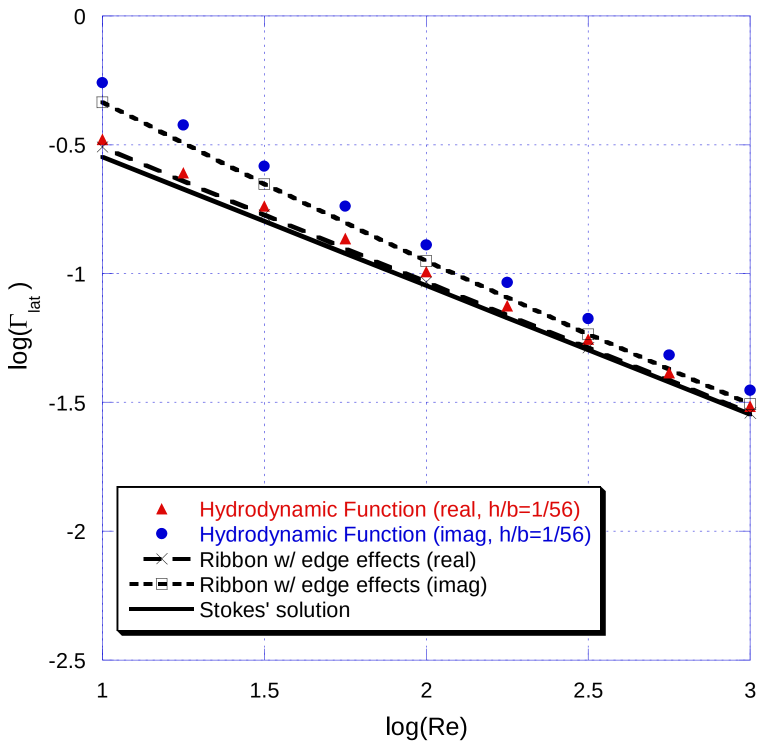

Figure 3-10. The real and imaginary parts of Γ_{lat} as a function of the Reynolds number found using a finite element model (*h/b*= 1/56) compared to the analytical results found using Stokes' theory and the numerical results for an infinitely thin microcantilever which accounts for edge effects given by Ref. 97.

While the real part of the hydrodynamic function generally follows the same trend as Stokes' solution, a large portion of the viscous damping from the edge effects is not accounted for when using Stokes' solution. This causes a large difference in the estimate of the imaginary part of the hydrodynamic function when using Stokes' solution. The edge effects can be taken into account using the results given in Ref. 97. Comparing the numerical results found using ANSYS to the results predicted from Ref. 97 for an infinitely thin microcantilever, the maximum difference in the real and imaginary parts of the hydrodynamic function decreases to 9.5% and 18.9%, respectively. This shows that the edge effects have a significant effect on the imaginary part of the hydrodynamic function when the Reynolds number is low and should be taken into account. However, there still is a discrepancy between the numerical results for a microcantilever of small yet finite thickness compared to the results for an infinitely thin microcantilever.

The majority of the remaining discrepancy comes from the additional hydrodynamic forces from the pressure incident on the leading and trailing edges of the microcantilever. Stokes' solution does not consider the effects of the pressure force on the microcantilever. Figure 3-11 shows the percent magnitude of the hydrodynamic force coming from the pressure as a function of both aspect ratio and Reynolds number. Even with an aspect ratio of 1/56, roughly 10% of the hydrodynamic force comes from the pressure acting on the leading and trailing edges of the microcantilever. For larger aspect ratios and higher Reynolds numbers, the pressure becomes the dominant force. This was seen previously in the results presented in Fig. 3-6.

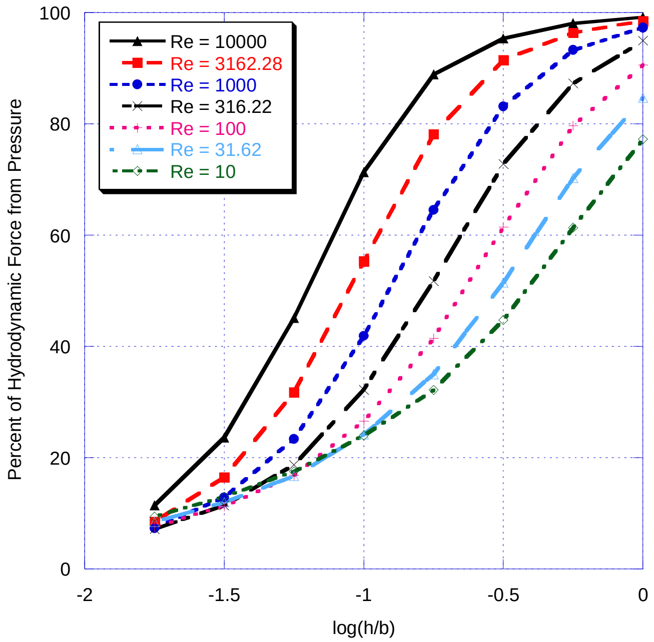

Figure 3-11. The percent of the hydrodynamic force from the fluid's pressure acting on a laterally vibrating microcantilever as a function of the aspect ratio and the Reynolds number.

For a microcantilever with an aspect ratio of 1/10 and a Reynolds number of 1000, 41.8% of the hydrodynamic force comes from the pressure. When the Reynolds number is increased to 10,000, this percentage increases to 71.3%. This is because the hydrodynamic force from the pressure increases at a rate faster than the shear force as the Reynolds number is increased.

The pressure also affects the real and imaginary parts of the hydrodynamic function differently. Figure 3-12 shows the percent of the real and imaginary parts of the hydrodynamic function coming from the pressure on the leading and trailing edges. The pressure's effect on the imaginary part of the hydrodynamic function is mostly independent of the Reynolds number. This means that both the shear force per unit length and the pressure per unit length in-phase with the velocity have approximately the same dependency on the Reynolds number.

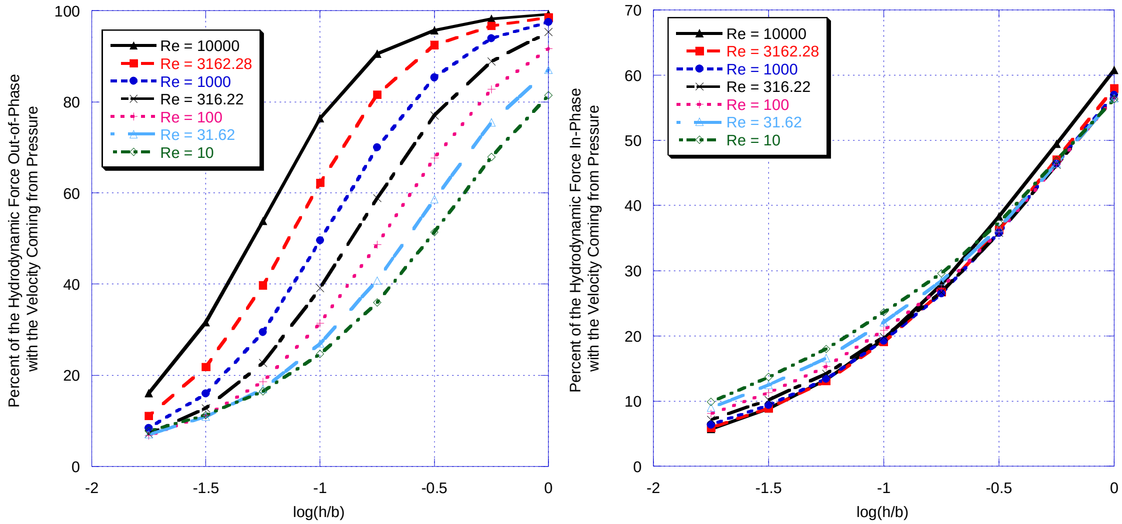

Figure 3-12. The percent of the real (left) and imaginary (right) parts of the hydrodynamic function coming from the fluid's pressure acting on a laterally vibrating microcantilever as a function of aspect ratio and Reynolds number.

The effect of the pressure on the real part of the hydrodynamic function as shown in Fig. 3-12, however, is a function of the aspect ratio and the Reynolds number. Analyzing Fig. 3-9 again, it can be seen that, for thick microcantilevers, the discrepancy between the real part of the numerical results and Stokes' solution increases as the Reynolds number is increased. This trend is opposite of what is expected from the derivation of Stokes' solution and opposite the trend seen in the numerical results for the imaginary part of the hydrodynamic function. This discrepancy arises from the fact that microcantilevers with a non-zero thickness vibrating laterally in an inviscid medium will have a non-zero displaced mass. The hydrodynamic function for a laterally vibrating microcantilever of non-zero thickness in an inviscid medium as a function of the aspect ratio has been approximated in the literature as [97]

$$\Gamma_{lat,inviscid}(h/b) = \frac{2}{\pi^2}\left(\frac{h}{b}\right)^2\left(1+2\ln\left(\frac{4\pi b}{h}\right)\right), \quad \left(\frac{h}{b}\right) << 1 \ . \qquad \textbf{(Eq. 3-26)}$$

Figure 3-13 plots the real and imaginary parts of the hydrodynamic function as a function of the Reynolds number for an aspect ratio of 1/10. The results are also compared to both Stokes' solution and the inviscid solution of Eq. 3-26. Note that the real part of the hydrodynamic function converges to the inviscid solution as the Reynolds number is increased, while the imaginary part of the hydrodynamic function converges to Stokes' solution. For thicker microcantilevers, the inviscid solution is larger and the numerical results for the real part of the hydrodynamic function diverge from Stokes' solution at lower Reynolds numbers.

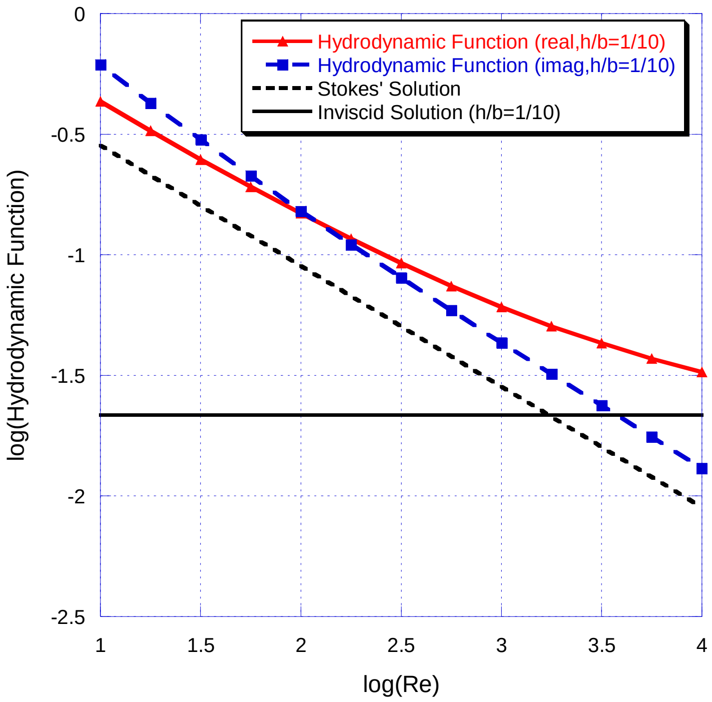

Figure 3-13. The real and imaginary parts of the hydrodynamic function as a function of the Reynolds number found using a finite element model (*h/b*=1/10) compared to the analytical results found using Stokes' theory which are independent of *h/b* and the Reynolds number-independent inviscid solution from Ref. 97.

While it is logical to expect the effects of pressure force per unit length to change as a function of the microcantilever's thickness, the shear force per unit length can also have a dependency on the microcantilever's thickness. The hydrodynamic force per unit length from the shear and pressure, both in-phase and out-of-phase with velocity and with a Reynolds number of 1000, is plotted as a function of h/b in Fig. 3-14. The hydrodynamic force per unit length, as compared to the hydrodynamic function, is not only dependent on the aspect ratio and Reynolds number but also on the dynamic viscosity and density of the medium and width of the microcantilever.

The microcantilever in Fig. 3-14 has a width of 20 μm and is assumed to be operating in water. The shear force per unit length increases when the microcantilever's thickness is increased. However, this increase in shear force per unit length is insignificant when compared to the increase in the pressure, since the pressure is the dominant force per unit length when the microcantilever is thick (or when the aspect ratio approaches one). The results show that both the edge effects and the effect of thickness are accounted for using this method.

Another method found in the literature that accounts for these effects is illustrated by the numerical results for the hydrodynamic function calculated in Ref. 97. The hydrodynamic function calculated for particular aspect ratios and Reynolds numbers using both methods can be compared. However, because the set of aspect ratios and Reynolds numbers investigated in Ref. 97 is different from the set used in this investigation, only aspect ratios of 1/10 and 1 were studied in both investigations. The results for these two particular aspect ratios are shown in Table 3-3.

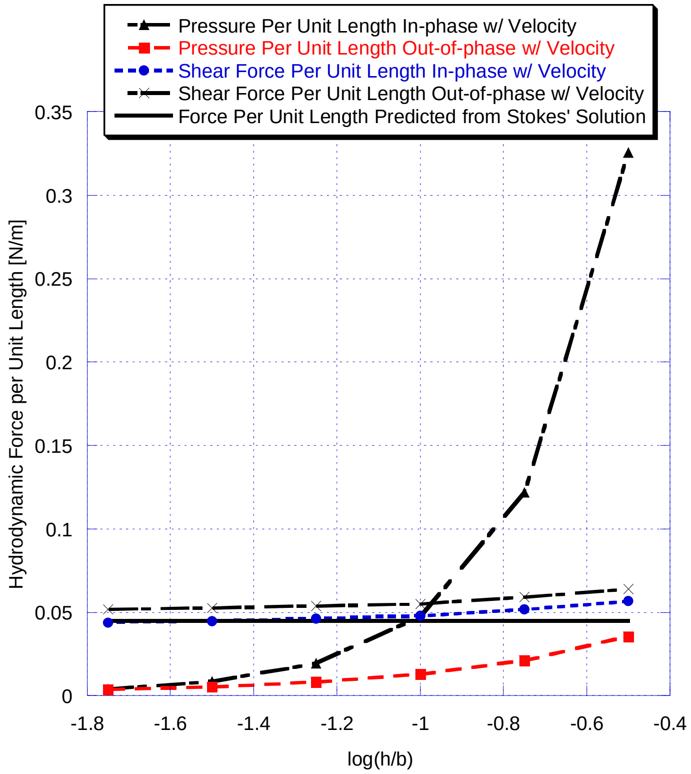

Figure 3-14. The hydrodynamic force per unit length from the shear and pressure both in-phase and out-of-phase acting on a laterally vibrating microcantilever in water (*b*=20 μm, Re=1000) as a function of *h*/*b*.

Aspect Ratio (*h*/*b*)	1	1	1	1	1	1/10	1/10	1/10	1/10	1/10
Reynolds Number (Re)	10	31.622	100	316.22	1000	10	31.622	100	316.22	1000
$\Gamma_{\text{lat,real}}$	2.63786	2.14498	1.86329	1.6966	1.6077	0.431921	0.248093	0.148863	0.092239	0.060745
$\Gamma_{\text{lat,real}}$ from Ref. 97	2.68270	2.17551	1.88862	1.7259	1.6336	0.435349	0.249659	0.148772	0.093131	0.062098
$\Gamma_{\text{lat,imag}}$	1.30009	0.691868	0.378749	0.211151	0.118406	0.614016	0.300438	0.151914	0.080176	0.043274
$\Gamma_{\text{lat,imag}}$ from Ref. 97	1.31768	0.703142	0.384789	0.213840	0.119870	0.575374	0.283225	0.145302	0.076988	0.041760

Table 3-3. Comparison of the numerical results for the hydrodynamic function calculated using FEA and the method given in Ref. 97.

Using the FEA results in the denominator, the numerical results had an average absolute difference of 1.2% (maximum of 2.2% for Re = 1000 and *h/b* = 1/10) in the real part of the hydrodynamic function and an average absolute difference of 3.09% (maximum of 6.2% for Re = 10 and *h/b* = 1/10) in the imaginary part of the hydrodynamic function. The differences between the two results could be attributed to the fact that the solution is not completely convergent. The FEA model also takes into account the convective terms of the equation of motion of the fluid, which might more accurately reflect the physical system. If an analytical expression for the hydrodynamic function that covered all the combinations of aspect ratios and Reynolds numbers used in this investigation could be found, the two techniques could be more accurately compared. The development of such an analytical expression is discussed in the next section.

3.5 Analytical Approximation for the Hydrodynamic Function

The hydrodynamic function of a laterally vibrating microcantilever can be found numerically using the procedure described in section 3.4. However, the time required in finding the hydrodynamic function at a particular Reynolds number and aspect ratio is prohibitive. Therefore, a simple analytical form for the hydrodynamic function is desired so that the trends in the hydrodynamic function with respect to the geometry and medium of operation can be investigated. A simple analytical expression for the hydrodynamic function, Eq. 3-19, was found in section 3.3 for a well-known limiting case. Equation 3-19 can be modified using a correction factor to account for both edge effects and the effect of thickness using the results from section 3.4. A set of correction factors, C_R and C_I, can be found so that

$$\Gamma_{lat}(\mathrm{Re}, h/b) = \frac{2\sqrt{2}}{\pi\sqrt{\mathrm{Re}}}(C_R + jC_I) \qquad \textbf{(Eq. 3-27)}$$

where,

$$C_R = \frac{\pi\sqrt{\mathrm{Re}}}{2\sqrt{2}}\Gamma_{lat,numerical,R}(\mathrm{Re}, h/b) \qquad \textbf{(Eq. 3-27a)}$$

$$C_I = \frac{\pi\sqrt{\mathrm{Re}}}{2\sqrt{2}}\Gamma_{lat,numerical,I}(\mathrm{Re}, h/b) \qquad \textbf{(Eq. 3-27b)}$$

It can be seen from Fig. 3-15 that C_R is roughly a linear function of $\mathrm{Re}^{1/2}$. This linearity arises from the fact that the real part of the hydrodynamic function converges to the inviscid solution when $h/b \ll 1$ [97]. The ratio of the inviscid solution and the real part of Stokes' solution is

$$\frac{\Gamma_{lat,inviscid}(h/b)}{\Gamma_{lat,Stokes,real}(\mathrm{Re})} = \sqrt{\mathrm{Re}}\left(\frac{h}{b}\right)^2\left(1 + 2\ln\left(\frac{4\pi b}{h}\right)\right) \quad . \qquad \textbf{(Eq. 3-28)}$$

However, due to the additional viscous damping from the medium, the dependency on the aspect ratio is not the same as in the inviscid solution case and it is expected that this trend would not hold for microcantilevers operating in media with high viscosities. If each C_R vs. $\mathrm{Re}^{1/2}$ curve is projected back to the case of a zero Reynolds number (infinite viscosity), the correction factor is found to be non-zero. This is due to edge effects. The slope and intercept of each C_R vs. $\mathrm{Re}^{1/2}$ curve can be found. Plotting the slope of each curve as a function of $(h/b)^2$, it can be seen that the trend is again roughly linear. However, there is a slight inflection in the curve due to the missing second term from the inviscid solution. It is then found that using $(h/b)^{1.83}$ gives a better fit of the curve, as shown in Fig. 3-16. Using (h/b)$^{1.83}$ instead of (h/b)^{2}, the slope of the curve in Fig. 3-16 is approximately 1.658.

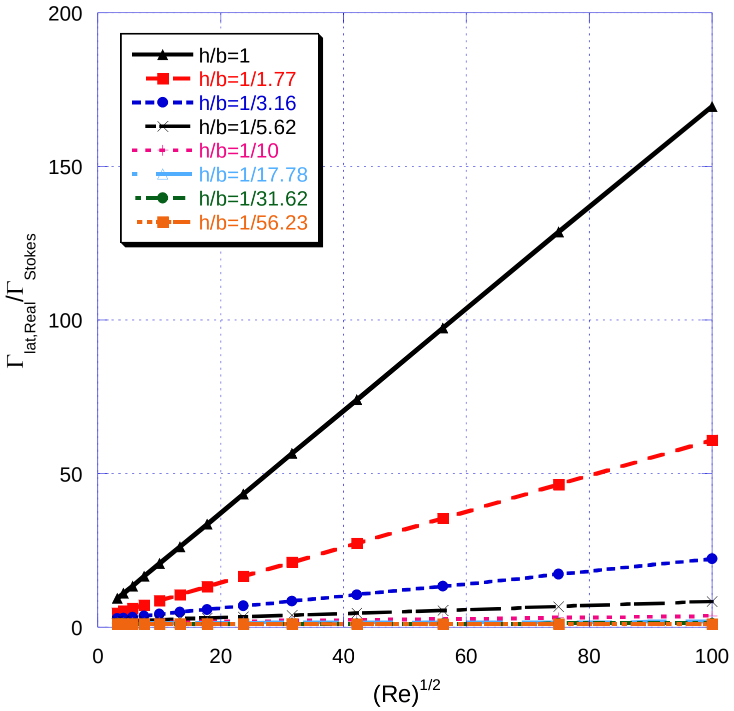

Figure 3-15. The ratio of the real part of the simulated hydrodynamic function to Stokes' solution as a function of Re$^{1/2}$ for eight different aspect ratios.

When the Reynolds number goes to zero (or as the viscosity goes to infinity), it is shown in Fig. 3-15 that the ratio of the numerical data to Stokes' solution goes to a particular value. This value (the estimated y-intercept of the curves in Fig. 3-15) is found to be a function of aspect ratio. Since Stokes' solution was derived for an infinitely thin microcantilever, this value should be one at h/b = 0. It is found that the estimated value of C_R when Re = 0, as shown in Fig. 3-17, is roughly linear with respect to h/b. The power by which the aspect ratio is raised can again be adjusted, correcting for the slight inflection of the curve. Investigating the R^{2} values for different exponents, (h/b)$^{0.85}$ is found to be the best exponent to fit the curve. The slope of the curve in Fig. 3-17 is approximately 3.08.

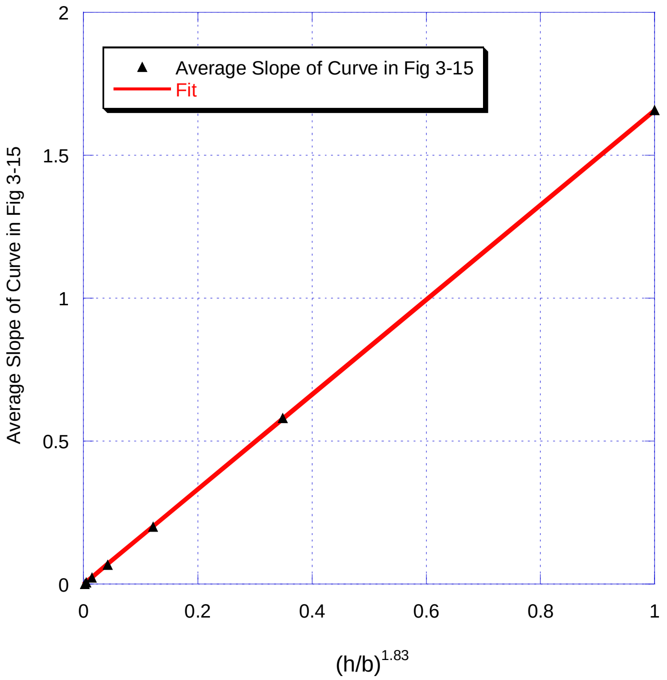

Figure 3-16. The average slope of each C_R vs. $\mathrm{Re}^{1/2}$ curve in Fig. 3-15 as a function of $(h/b)^{1.83}$.

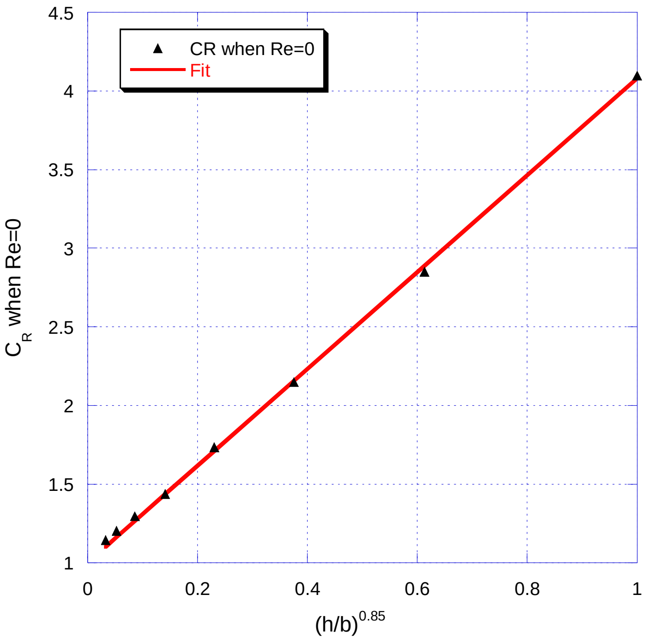

Figure 3-17. The estimated value of C_R when the Reynolds number is zero as a function of $(h/b)^{0.85}$.

The same procedure can be used to find C_I. It is found that C_I depends on $Re^{-1/2}$, as seen in Fig. 3-18. The slope and *y*-intercept of each curve can again be found for each particular aspect ratio. Figure 3-19 shows the slope of each curve as a function of *h/b*. Figure 3-19 shows that the slopes of the curves in Fig. 3-18 have a linear dependence on *h/b*. However, when the microcantilever's thickness is zero, the hydrodynamic function is not equal to Stokes' solution. This arises from the edge effects and can be clearly seen in Fig. 3-9. It is found that the best exponent to fit the curve found in Fig. 3-19 is exactly one. The slope of the line is approximately -1.321, with a *y*-intercept of approximately 2.56.

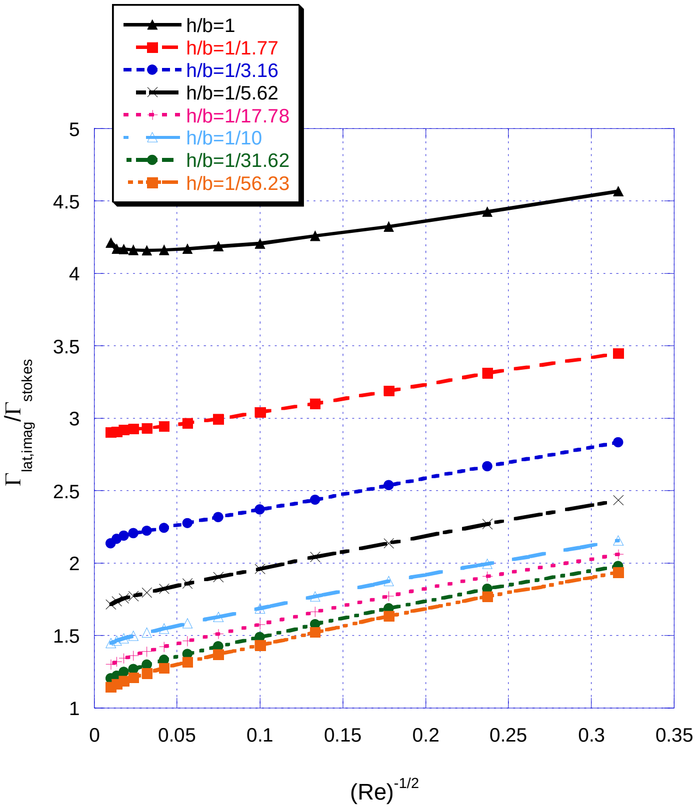

Figure 3-18. C_I as a function of $Re^{-1/2}$ plotted for eight different aspect ratios.

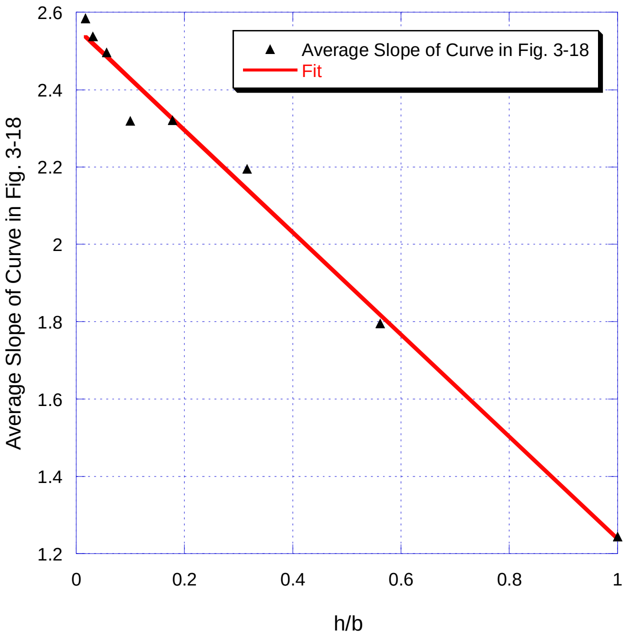

Figure 3-19. The average slope of each C_I vs. $Re^{-1/2}$ curve as a function of the aspect ratio.

The value of C_I when the Reynolds number goes to infinity (or when the medium becomes inviscid) converges to a particular value. These values are a function of the aspect ratio and are plotted in Fig. 3-20. There is again a slight inflection, and $(h/b)^{0.85}$ is found to provide the best fit to the curve with a slope of approximately 3.108. Note that the power is the same as in the second term of C_R, only with a different slope.

The correction factor for the real and imaginary part of the hydrodynamic function can then be given as

$$C_R = 1.658\left(\frac{h}{b}\right)^{1.83}\sqrt{\mathrm{Re}} + 3.08\left(\frac{h}{b}\right)^{0.85} + 1 \qquad \textbf{(Eq. 3-29)}$$

$$C_I = \left(2.56 - 1.321\left(\frac{h}{b}\right)\right)\frac{1}{\sqrt{\mathrm{Re}}} + 3.108\left(\frac{h}{b}\right)^{0.85} + 1 \qquad \textbf{(Eq. 3-30)}$$

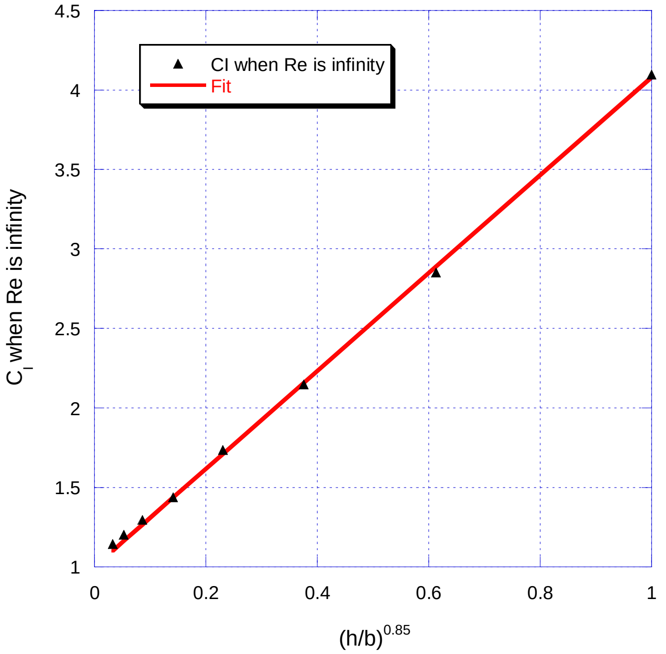

Figure 3-20. The value of C_I when the Reynolds number is infinity as a function of $(h/b)^{0.85}$.

This shows that if the thickness is zero and Re>>1, Stokes' solution can be used. However, even with an aspect ratio of 1/56, the real part of the hydrodynamic function is at least 10% greater (when Re= 10) than what is calculated using Stokes' solution. Increasing the Reynolds number will increase this discrepancy. For an aspect ratio of 1/10 and a Reynolds number of 10, the displaced mass will be a factor of ~1.5 times greater than what is calculated using Stokes' solution. When the Reynolds number is increased to 10,000, the displaced mass will be a factor of ~3.77 times greater than the results obtained using Stokes' solution. The same trends are seen for C_I. Thus, Stokes' solution cannot be used to predict the displaced mass without first using Eqs. 3-29 and 3-30 to correct for the edge effects and the effect of thickness.

These correction factors can be used to find the hydrodynamic function for every simulated combination of aspect ratio and Reynolds number. The hydrodynamic function found from Eq. 3-27 can then be compared to the numerical results. This gives a measure of the quality of the fit of the numerical data. For microcantilevers with an aspect ratio $h/b \geq 1/56$ and Reynolds numbers between 10 and 10,000, the obtained imaginary part of the hydrodynamic function is within 5.7% of the numerical results. For Reynolds numbers between 10 and 1000 and $h/b \geq 1/56$, the calculated real part of the hydrodynamic function is also within 5.7% of the numerical results. At higher Reynolds numbers, the calculated real part of the hydrodynamic function shows a difference of up to 20.5% for microcantilevers with $h/b < 1/10$. A more complicated fitting model could be used to improve the semi-analytical method; however, at a high Reynolds number, the microcantilever's mass is usually much larger than the displaced fluid mass.

Another test of the accuracy of Eq. 3-27 is to compare it to other values found in the literature. As mentioned previously, Ref. 97 used a similar procedure to that found in Ref. 102 to find the hydrodynamic function as a function of both Reynolds number and aspect ratio. Using Eq. 3-27 to calculate the hydrodynamic function, the real and imaginary part of the hydrodynamic function can be compared to the results given in the literature using

$$\%|Diff_{real}| = \frac{|\Gamma_{lat,real}(\mathrm{Re}, h/b) - \Gamma_{lat,literature,real}(\mathrm{Re}, h/b)|}{\Gamma_{lat,real}(\mathrm{Re}, h/b)} * 100\% \qquad \textbf{(Eq. 3-31)}$$

and

$$\%|Diff_{imag}| = \frac{|\Gamma_{lat,imag}(\mathrm{Re}, h/b) - \Gamma_{lat,literature,imag}(\mathrm{Re}, h/b)|}{\Gamma_{lat,imag}(\mathrm{Re}, h/b)} * 100\%, \qquad \textbf{(Eq. 3-32)}$$

where $\Gamma_{lat,literature}$ is the value given by Ref. 97. Table 3-4 gives the absolute percent difference of the real part of the hydrodynamic function between the two methods for a range of aspect ratios and Reynolds numbers.

	Log(Re)=1	1.5	2	2.5	3
h/b=1	1.07%	1.39%	1.55%	1.58%	1.56%
0.5	1.11%	0.63%	0.02%	0.44%	0.73%
0.2	1.02%	1.81%	1.65%	1.06%	0.42%
0.1	1.09%	0.87%	1.66%	1.69%	1.33%
0.05	3.49%	0.87%	0.66%	1.35%	1.53%
0.02	5.88%	2.79%	0.89%	0.22%	0.82%

Table 3-4. The absolute percent difference in the real part of the hydrodynamic function calculated using Eq. 3-27 compared to the values given in Ref. 97 as a function of aspect ratio and Reynolds number.

There is an average absolute percent difference of 1.37% over the range of values considered in both methods. The maximum percentage difference between the two techniques when calculating the real parts of the hydrodynamic function is 5.88% when using an aspect ratio of 1/50 and a Reynolds number of 10.

Table 3-5 gives the absolute percent difference of the imaginary part of the hydrodynamic function between the two methods for a range of aspect ratios and Reynolds numbers. There is an average absolute difference of 3.8% over the range of aspect ratios and Reynolds numbers simulated by both methods. The maximum percentage difference between the two techniques when calculating the imaginary part of the hydrodynamic function is 9.85%.

	Log(Re)=1	1.5	2	2.5	3
h/b=1	2.86%	1.47%	1.00%	1.11%	1.53%
0.5	3.25%	3.30%	3.22%	2.95%	2.52%
0.2	7.06%	5.37%	4.61%	4.19%	3.85%
0.1	8.42%	5.44%	4.03%	3.48%	3.23%
0.05	9.20%	5.21%	3.16%	2.36%	2.15%
0.02	9.85%	4.93%	2.26%	1.12%	0.83%

Table 3-5. The absolute percent difference in the imaginary part of the hydrodynamic function calculated using Eq. 3-27 compared to the values given in Ref. 97 as a function of aspect ratio and Reynolds number.

.

This again occurs when using an aspect ratio of 1/50 and a Reynolds number of 10. Due to the lower viscous damping predicted from Ref. 97, the quality factors calculated using Eq. 3-27 will be slightly lower than those calculated using the method found in Ref. 97. The effects of using this method as opposed to the one found in Ref. 97 to find sensor characteristics (such as the quality factor) will be investigated in chapter 4.

4. Characteristics of Laterally Vibrating Microcantilevers

4.1 Introduction

The characteristics of laterally vibrating microcantilevers in viscous liquid media are theoretically evaluated in this chapter. The characteristics investigated in this work include the beam’s resonant frequency, quality factor, and mass sensitivity, which can be calculated from the frequency response of the beam’s deflection. The deflection of the microcantilever’s tip was found in chapter 2 as a function of the properties of the beam, the total hydrodynamic force applied by the medium, and the frequency of excitation. An approximation of the hydrodynamic force was found in chapter 3 as a function of the Reynolds number and the beam’s aspect ratio. Using this expression with the expression for the deflection of the microcantilever’s tip, the frequency spectrum of the beam can be found. From the frequency spectrum, relevant characteristics of the system can be modeled and investigated as a function of both the properties of the medium and the beam’s geometry. The characteristics of transversely vibrating beams can also be modeled using Eq. 3-23. This will allow the characteristics of both laterally and transversely vibrating beams of similar geometry to be compared and contrasted.

4.2 Resonant Frequency

The resonant frequency (of a given mode) of a dynamically driven microcantilever is defined as the applied excitation frequency that maximizes the amplitude of deflection of a particular mode of vibration [124]. In sensing applications, changes in the resonant frequency of the microcantilever can be used to monitor changes in the microcantilever's operational environment. For example, if a sensing layer is applied to the top surface of the microcantilever, the resonant frequency will change as a function of the amount of analyte sorbed into the sensing layer due to added mass and changes in the viscoelastic properties of the layer. The resonant frequency can then be used to track the concentration of particular analytes in the medium of operation. It is also important to know the resonant frequency when evaluating other characteristics of the microcantilever, such as the quality factor, mass sensitivity, and chemical sensitivity.

Eq. 2-31 can be used to find the tip displacement as a function of the frequency of excitation, and is repeated below for convenience:

$$\left|V(L)\right| = \left|\sum_{i=1}^{\infty} \frac{\int_0^L F_y(x)\phi_i(x)dx}{\sqrt{\left(EI_{lat}\beta_j^4 - \left(\rho_B bh + g_{2,lat}\right)\omega^2\right)^2 + \left(g_{1,lat}\omega\right)^2}\int_0^L \phi_i{}^2(x)dx}\phi_i(L)\right| .$$

(Eq. 4-1)

Any point along the length of the beam may be chosen to investigate the response as a function of frequency of excitation as long as the point is not a vibrational node for the particular in-plane flexural mode under investigation. The tip is chosen for convenience. It was noted in chapter 2 that all parameters in Eq. 4-1 could be estimated except for F_y,

$g_{1,\mathrm{lat}}$ and $g_{2,\mathrm{lat}}$. The excitation force per unit length, F_y, is not frequency-dependent and thus only acts to scale the magnitude of the tip deflection. However, $g_{1,\mathrm{lat}}$ and $g_{2,\mathrm{lat}}$ are related to the viscous damping per unit length and displaced mass per unit length of the medium of operation, respectively. They can be calculated using Eqs. 2-4 and 2-5, repeated here for convenience:

$$g_{1,lat} = \frac{\pi}{4}\rho_L b^2 \Gamma_{lat,I}(\mathrm{Re}, h/b)\omega, \qquad \textbf{(Eq. 4-2)}$$

$$g_{2,lat} = \frac{\pi}{4}\rho_L b^2 \Gamma_{lat,R}(\mathrm{Re}, h/b), \qquad \textbf{(Eq. 4-3)}$$

where the subscripts R and I stand for the real and imaginary part of the hydrodynamic function Γ_{lat} , respectively. The hydrodynamic function was found in chapter 3 as

$$\Gamma_{lat}(\mathrm{Re}, h/b) = \frac{2\sqrt{2}}{\pi\sqrt{\mathrm{Re}}}(C_R + jC_I) \qquad \textbf{(Eq. 4-4)}$$

where C_R and C_I are correction factors to account for the edge effects and the effects of beam thickness and are given as

$$C_R = 1.658\left(\frac{h}{b}\right)^{1.83}\sqrt{\mathrm{Re}} + 3.08\left(\frac{h}{b}\right)^{0.85} + 1, \qquad \textbf{(Eq. 4-4a)}$$

$$C_I = \left(2.56 - 1.321\left(\frac{h}{b}\right)\right)\frac{1}{\sqrt{\mathrm{Re}}} + 3.108\left(\frac{h}{b}\right)^{0.85} + 1. \qquad \textbf{(Eq. 4-4b)}$$

Equation 4-1 also requires the microcantilever's dimensions, density, and Young's modulus to be specified in order to calculate the frequency spectrum. In this investigation, the theoretical results predicted from Eq. 4-1 will be compared to experimentally determined results given in the literature. When experimental data cannot be found in the literature, the theoretical results for laterally vibrating beams with an assumed density of 2330 kg/m^3 and an assumed Young's modulus of 169 GPa (silicon cut along the <110> direction [119]) will be given unless otherwise specified. The length of the beam is chosen as 400 μm, which is assumed large enough to neglect shear and rotational inertia, while still short enough to illustrate the high resonant frequencies and quality factors associated with laterally vibrating beams. Figure 4-1 shows the frequency spectrum of a 400x45x12 μm laterally vibrating silicon beam in air (ρ_L = 1.205 kg/m^3 and η = 0.01827 cP for 20° C) [125-126]. The forcing function, $F_y(x)$, is assumed to be uniform along the length of the beam.

Figure 4-1 is normalized to the maximum deflection of the tip when vibrating laterally. The higher-order modes have higher resonant frequencies yet smaller tip deflections compared with the fundamental mode. Note that the tip deflection calculated from Eq. 4-1 is the infinite sum of the contributions from each mode. It is noted from Fig. 4-1 that each mode is dominant around (within the 3 dB bandwidth) its resonant frequency. Thus, only the ith term of Eq. 4-1 is significant in air when calculating the ith in-plane flexural mode's resonant frequency.

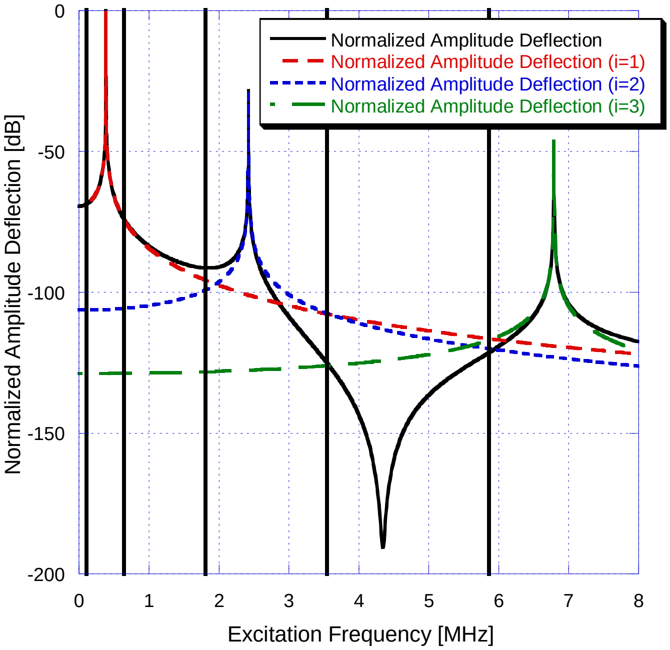

Figure 4-1. The simulated frequency spectrum of a 400x45x12 μm silicon microcantilever in air found from Eq. 4-1 normalized to its maximum deflection. The contributions of the first three in-plane flexural modes are plotted separately. The resonant frequencies of the first 5 out-of-plane flexural modes in air are indicated as vertical lines.

This trend also generally holds true for beams operating in liquid as long as the mode number is low and viscous damping is not significant. The resonant frequencies of the first five transverse modes calculated for a 400x45x12 μm silicon beam are also indicated using vertical lines in Fig. 4-1. Note that the 1st lateral mode's resonant frequency is roughly 3.75 times higher than the 1st transverse mode's resonant frequency. This is due to the beam's greater stiffness when vibrating in the lateral direction.

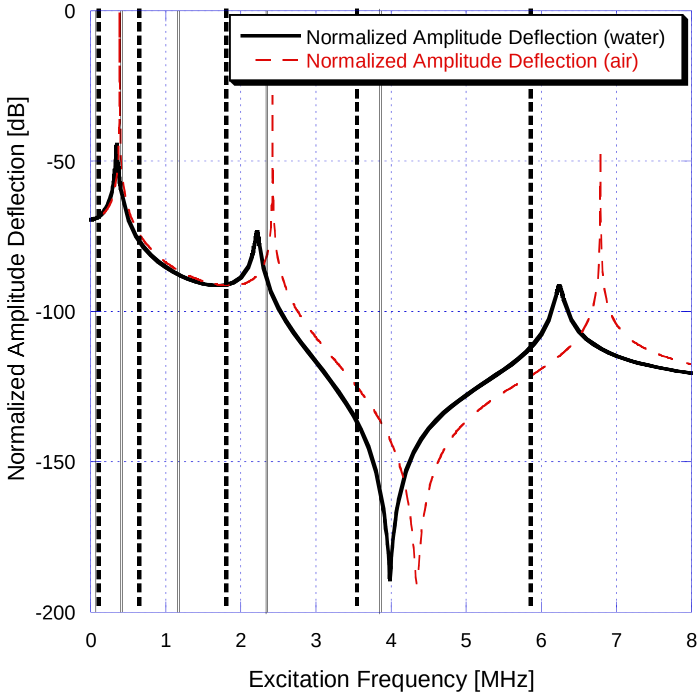

Figure 4-2. The simulated frequency spectrum of a 400x45x12 μm silicon microcantilever operating in the in-plane flexural mode in both air and water. The resonant frequencies of the first 5 transverse flexural modes in air and water are also given as dotted and solid vertical lines, respectively.

Figure 4-2 gives the frequency spectrum of a 400x45x12 μm microcantilever laterally vibrating in water (ρ_L = 1000 kg/m^3 and η = 1 cP for 20° C) [125], compared to the same beam's frequency spectrum in air. The deflection in Fig. 4-2 is normalized to the maximum deflection of the tip in the first in-plane mode in air. Using the same value for F_y, the maximum deflection is 167 times larger in air compared to water. It is noted that in order to cause the same maximum deflection, the amount of force needed to drive the microcantilever for this geometry must be more than two orders of magnitude larger in water compared to air. It is also noted that both the lateral and transverse resonant frequencies shift downward and the spectrum is broader due to the higher viscous damping and displaced mass from the medium of operation. For this particular geometry, while the fundamental resonant frequency for the transverse mode drops by 37.7% due to the increased displaced fluid mass and viscous damping, the lateral mode's fundamental resonant frequency drops by only 10.14%. The same trend is seen in the higher-order modes. This substantially smaller drop in resonant frequency for laterally vibrating beams compared to transversely vibrating beams of similar geometry indicates that the amount of fluid damping is smaller for laterally excited beams and thus the characteristics of the device will be less affected by operating in viscous liquid media. This indicates that lateral excitation is a more suitable method of excitation for dynamically driven microcantilevers compared to transverse excitation when operating in viscous liquid media.

If an expression for the resonant frequency is found, the trends in the resonant frequency as a function of the microcantilever's geometry and as a function of medium properties (dynamic viscosity and fluid density) can be given. An expression for the resonant frequency of a laterally vibrating beam can be derived using the procedures outlined in Ref. 124, as the form of the equation of motion is the same for both laterally and transversely vibrating beams. However, the values for the moment of inertia (I_{lat}) and the hydrodynamic function (Γ_{lat}) will be different from those given in Ref. 124 since the beam is vibrating laterally. It is noted that only the first part of Eq. 4-1 is frequency-dependent. This means, neglecting the effects of other modes, that the maximum deflection of the tip of the microcantilever for its *i*th mode can be found as the excitation frequency, ω, that satisfies

$$\frac{d}{d\omega}\left(\frac{1}{\sqrt{\left(EI_{lat}\beta_i^4-\left(\rho_B bh+g_{2,lat}\right)\omega^2\right)^2+\left(g_{1,lat}\omega\right)^2}}\right)=0$$

(Eq. 4-5)

and

$$\frac{d^2}{d\omega^2}\left(\frac{1}{\sqrt{\left(EI_{lat}\beta_i^4-\left(\rho_B bh+g_{2,lat}\right)\omega^2\right)^2+\left(g_{1,lat}\omega\right)^2}}\right)<0.$$

(Eq. 4-6)

The excitation frequency that satisfies both of these conditions is the resonant frequency of the *i*th lateral flexural mode and can be expressed in the form

$$f_{res,lat,i}=\frac{\left(\beta_i L\right)^2}{2\pi}\sqrt{\frac{k_{lat}}{M_{lat}}}\ ,$$

(Eq. 4-7)

where β_i is given by Eq. 2-22; and the effective spring constant, k_{lat}, and the effective mass, M_{lat} are defined as

$$k_{lat}=\frac{EI_{lat}}{L^3}\,,$$

(Eq. 4-7a)

$$\begin{aligned} M_{lat} &= \rho_B bhL + Lg_{2,lat} \\ &+ L\,\frac{\left(g_{1,lat}/\omega_{lat}\right)+\left(\frac{\omega_{lat}}{2}\right)\frac{d}{d\omega}\left(g_{1,lat}/\omega_{lat}\right)}{\left(\rho_B bh+g_{2,lat}+\left(\frac{\omega_{lat}}{2}\right)\frac{d}{d\omega}\left(g_{2,lat}\right)\right)}\left(g_{1,lat}/\omega_{lat}\right). \end{aligned}$$

(Eq. 4-7b)

Equation 4-7a indicates that shorter beams and beams with higher flexural rigidities (EI_{lat}) have higher resonant frequencies due to their increased stiffness. However, changing the resonant frequency will also change the effective mass. As the Reynolds number is a function of the frequency of excitation, Eq. 4-7 is a transcendental equation and any attempt at finding the system's resonant frequency must be done through iteration. The resonant frequency can be found through an iterative process by

$$f_{res,lat} = \lim_{n->\infty} F_1^{\,n}(f_{guess}) \qquad \textbf{(Eq. 4-8)}$$

where $F_1^{\,n}(f_{guess})$ is the function F_1 applied n times to f_{guess}, $F_1(f_{guess})$ is the right hand side of Eq. 4-7, and f_{guess} is a guess value of the resonant frequency. Since the resonant frequency of a laterally vibrating beam does not decrease significantly when operating in water compared to the same beam operating in air or in vacuum, a good initial guess for the resonant frequency of a laterally vibrating microcantilever in a viscous liquid medium is the resonant frequency of the microcantilever in a vacuum, f_0, which is given by

$$f_0 = \frac{(\beta_i L)^2 b}{2\pi L^2}\sqrt{\frac{E}{12\rho_B}}\,. \qquad \textbf{(Eq. 4-9)}$$

It was noted in chapter 3 that, as Re approaches infinity, both the hydrodynamic function and its derivative with respect to Re approach zero. Taking the derivative of the real and imaginary parts of the hydrodynamic function as a function of the excitation frequency and using Eqs. 4-2 and 4-3,

$$\left(\frac{\omega_{lat}}{2}\right)\frac{d}{d\omega}\left(g_{1,lat}\big/\omega\right)=\frac{-\sqrt{2}\rho_L b^2}{4\mathrm{Re}}\left(2.56-1.321\left(\frac{h}{b}\right)\right)-\frac{\sqrt{2}\rho_L b^2}{8\sqrt{\mathrm{Re}}}\left(3.108\left(\frac{h}{b}\right)^{0.85}+1\right)$$

(Eq. 4-10)

and

$$\left(\frac{\omega_{lat}}{2}\right)\frac{d}{d\omega}\left(g_{2,lat}\right)=\frac{-\sqrt{2}\rho_L b^2}{8\sqrt{\mathrm{Re}}}\left(3.08\left(\frac{h}{b}\right)^{0.85}+1\right). \qquad \textbf{(Eq. 4-11)}$$

When the Reynolds number is large, Eq. 4-10 and 4-11 approach zero (meaning that the hydrodynamic function is roughly frequency-independent) and Eq. 4-7 can be simplified to

$$f_{res,lat,i} = \frac{(\beta_i L)^2}{2\pi L^2}\sqrt{\frac{EI_{lat}\left(\rho_B bh + g_{2,lat}\right)}{\left(\rho_B bh + g_{2,lat}\right)^2 + \left(g_{1,lat}/\omega\right)^2}} \ . \qquad \textbf{(Eq. 4-12)}$$

Iteration must still be used, as $g_{1,lat}$ and $g_{2,lat}$ still depend on the resonant frequency. This approximation can be compared with the exact expression given by Eq. 4-7 with the same set of nine aspect ratios and Reynolds numbers that were used to test for solution convergence in chapter 3. As the geometry of the beam is determined by three parameters, a constant length of 400 μm will be assumed for all nine test geometries. Assuming operation in water, the width can be varied over a range of values until the resonant frequency of the particular geometry yields the desired Reynolds number. The minimum and maximum Reynolds number used in chapter 3 will be investigated. A Reynolds number in-between these two values (on a log scale), $10^{2.5}$ or 316.23, is also investigated. The thickness is also varied to maintain the desired aspect ratio. The nine test geometries are given in Table 4-1 along with the first mode's resonant frequency as calculated by Eq. 4-7. It should be noted that these geometries are selected only for illustrating the accuracy of the approximations over the range of aspect ratios and Reynolds numbers investigated. Some of the microcantilevers with geometries given in Table 4-1 would make poor sensing platforms, while others would be too stiff to excite laterally.

Aspect Ratio (*h/b*)	1	1	1	1/10	1/10	1/10	1/56	1/56	1/56
Reynolds Number (Re)	10	316.23	10000	10	316.23	10000	10	316.23	10000
h (μm)	10.1367	30.8836	97.0374	1.13381	3.01424	9.22685	0.263799	0.598508	1.666543
b (μm)	10.1367	30.8836	97.0374	11.3381	30.1424	92.2685	14.8345	33.6566	93.7166
L (μm)	400	400	400	400	400	400	400	400	400
f_{res} Using Eq. 4-7 (kHz)	62.170	211.710	678.120	49.869	222.31	750.037	29.226	178.625	727.157
f_{res} Using Eq. 4-12 (kHz)	61.759	211.652	678.114	46.098	221.13	749.882	25.932	173.395	724.898
f_{res} Using Eq. 4-12, Numerical Results (kHz)	61.822	211.706	678.326	47.636	221.805	752.584	27.084	172.179	734.92
f_{res} Using Eq. 4-7, C_R=C_I=1 (kHz)	83.830	263.554	833.245	69.960	238.783	781.668	48.364	192.796	739.716
f_0 (kHz)	87.161	265.554	834.382	97.491	259.181	793.376	127.555	289.398	805.828

Table 4-1. The resonant frequency calculated using Eq. 4-7 and the resonant frequency calculated using several different approximations for nine different laterally vibrating beams assuming operation in water, a beam density of 2330 kg/m^3, and a Young's modulus of 169 GPa.

Table 4-1 also gives the approximation of the resonant frequency for high Reynolds numbers calculated from Eq. 4-12. It is shown that Eq. 4-12 is a good approximation of the resonant frequency over the range of aspect ratios investigated if the Reynolds number is large. As the thickness decreases, the difference between the resonant frequencies calculated using Eq. 4-7 and Eq. 4-12 increases due to the decreasing beam mass. The approximation only affects the displaced mass and viscous damping. If the beam mass is much larger than the displaced mass and viscous damping, the approximation of the resonant frequency given by Eq. 4-12 should be equal to the value given by Eq. 4-7.

The approximation of the resonant frequency for high Reynolds numbers calculated from Eq. 4-12 in the seventh row of Table 4-1 uses the approximation for the hydrodynamic function given in chapter 3. Since there is some discrepancy between the approximation of the hydrodynamic forces and the numerical results, a more accurate method of finding the resonant frequency is to use the numerical results directly. The eighth row of Table 4-1 uses Eq. 4-12 using the numerical results found in chapter 3. The resonant frequency calculated using the numerical results for the hydrodynamic function are found to be within 4.4% of the values given in the seventh row. The largest difference was again seen for thin beams, as variations in the hydrodynamic function affects the resonant frequency more when the beam mass is small. The resonant frequency can also be calculated using Stokes' solution (C_R=C_I=1) for the hydrodynamic function. These values are given in the ninth row of Table 4-1. As expected, when the beam is not thin and the Reynolds number is small, there is a significant discrepancy in the resonant frequency (up to 65%). The last row of Table 4-1 gives the resonant frequency in a vacuum of the particular beam geometry, f_0, for comparison.

Reference 97 also gives the hydrodynamic function of laterally vibrating beams for several different aspect ratios and Reynolds numbers using the boundary integral technique given by Ref. 102. The resonant frequency calculated using the method in Ref. 97 and the method given in chapter 3 can be compared. As Ref. 97 does not specify the derivative of $g_{1,lat}$ and $g_{2,lat}$ with respect to the frequency of excitation, Eq. 4-7 cannot be used with the results given in Ref. 97 to find the resonant frequency. As Eq. 4-12 was found to be a good approximation for the resonant frequency in Table 4-1 and does not depend on the derivatives of $g_{1,lat}$ and $g_{2,lat}$, it can be used to compare the resonant frequency calculated from using the hydrodynamic function given by Eq. 4-4 and the values for the hydrodynamic function given by Ref. 97. A set of nine geometries are again determined having lengths of 400 μm, aspect ratios ranging from 1/50 to 1, and Reynolds numbers ranging from 10 to 1000. These ranges cover the intersection of the range of aspect ratios and Reynolds numbers used in both investigations. It is assumed that the beam is operating in water.

There is good agreement (<1% difference) between the resonant frequencies calculated using both methods for Reynolds numbers above 100. For the lowest Reynolds number tested, the resonant frequencies calculated using the values for the hydrodynamic function in Ref. 97 were slightly higher (7.6% for the thinnest beam) due to the lower viscous damping predicted. However, the beams with Reynolds numbers of 10 are the beams with lower resonant frequencies and thus the lower quality factors and mass sensitivities. Beams with higher Reynolds numbers are desired and these beams show good agreement for the two methods.

Aspect Ratio (*h*/*b*)	1	1	1	0.1	0.1	0.1	0.02	0.02	0.02
Reynolds Number (Re)	10	100	1000	10	100	1000	10	100	1000
h (μm)	10.156	21.176	45.177	1.1534	2.1272	4.3501	0.297	0.497	0.924
b (μm)	10.156	21.176	45.177	11.534	21.272	43.501	14.864	24.859	46.188
L (μm)	400	400	400	400	400	400	400	400	400
f_{res} Using Eq. 4-12, and Eq. 4-4 for Γ_{lat} (kHz)	61.904	142.395	312.863	48	141.113	337.421	28.898	103.322	299.316
f_{res} Using Eq. 4-12, and Ref. 97 for Γ_{lat} (kHz)	61.677	141.969	312.011	49.705	142.009	337.955	31.101	104.101	299.946

Table 4-2. The resonant frequencies calculated from the approximate expression given by Eq. 4-12 of nine laterally vibrating beams assuming operation in water, a beam density of 2330 kg/m^3, and a Young's modulus of 169 GPa using Eq. 4-4 for the values of the hydrodynamic function compared to using the values given in Ref. 97 for the values of the hydrodynamic function.

4.2.1 Effects of the Medium's Density and Viscosity on the Resonant Frequency

From Tables 4-1 and 4-2, it is noted that increasing the Reynolds number drastically increases the resonant frequency. However, it is noted that in this case, the changes in the Reynolds number come from changes in the beam geometry. To investigate the effect the medium of operation has on the resonant frequency, the Reynolds number can be changed by using different dynamic viscosity and density values for the medium of operation. Using Eq. 4-7 and Eq. 4-9, it is shown that

$$f_{res} = f_0 \sqrt{\frac{\rho_B bhL}{M_{lat}}} \qquad \textbf{(Eq. 4-13)}$$

Using Eqs. 4-2, 4-3, 4-4, and 4-7, the ratio of the effective mass to the beam mass is given by

$$\frac{M_{lat}}{\rho_B bhL} = 1 + \frac{\rho_L}{\rho_B}\frac{b}{h}\frac{1}{\sqrt{\text{Re}}}\left(\frac{\sqrt{2}}{2}C_R + C_I{}^2\left(2\sqrt{\text{Re}}\frac{h\rho_B}{b\rho_L} + \sqrt{2}C_R\right)^{-1}\right). \qquad \textbf{(Eq. 4-14)}$$

Note that as the Reynolds number goes to infinity, the ratio does not approach one, as one of the terms in C_R depends on $\sqrt{\text{Re}}$. This is due to the fact that the beam will still displace mass even in an inviscid medium, thus dropping the resonant frequency from that found for the same beam operating in vacuum. Also note that the ratio is a function of the excitation frequency, both through the Reynolds number and C_R and C_I which depend on the Reynolds number.

The effects of the dynamic viscosity or density of the medium of operation could be investigated by fixing one quantity and varying the other. However, these values would not correspond to realistic examples of operational media. One way of investigating the effects of the medium of operation on the resonant frequency is to simulate the resonant frequency of a beam in various aqueous mixtures of glycerol. Simulating a 400x45x12 μm laterally vibrating silicon microcantilever and varying the dynamic viscosity and density properties for aqueous mixtures of glycerol ranging from 0% (pure water) to 72 w/w% (ρ_L = 1183 kg/m^3 and η = 27.57 cP) [125], the resonant frequency can be plotted as a function of the Reynolds number using Eq. 4-7. The results are shown in Fig. 4-3. Also plotted in Fig. 4-3 is the beam's resonant frequency in vacuum, the high Reynolds number approximation of the resonant frequency calculated from Eq. 4-12, and the resonant frequency calculated for the case of an inviscid medium (Eq. 4-7 where the hydrodynamic function is given by Eq. 3-26).

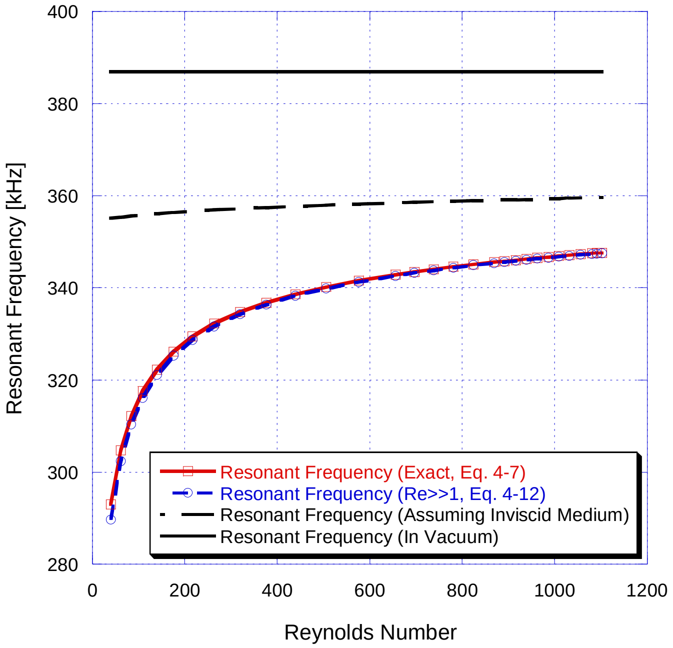

Figure 4-3. The resonant frequency of a 400x45x12 μm laterally vibrating silicon microcantilever calculated using the exact expression (Eq. 4-7), the approximate expression, (Eq. 4-12), valid for high Reynolds numbers, and assuming the medium is inviscid (Eq. 4-7 using Eq. 3-27 for Γ_{lat}) as a function of Reynolds number. The Reynolds number is varied assuming different mixtures of aqueous glycerol. The resonant frequency in a vacuum is also given.

It is shown in Fig. 4-3 that as the Reynolds number increases, the error in using Eq. 4-12 to approximate the resonant frequency decreases. The resonant frequency calculated from Eq. 4-7 approaches the resonant frequency calculated assuming an inviscid medium as the Reynolds number increases. Note that the resonant frequency calculated for the case of an inviscid medium changes due to the fact that the medium's density changes, which will change the amount of displaced mass.

The main change in the Reynolds number in Fig. 4-3 comes from the change in the medium's dynamic viscosity. This changes the hydrodynamic function, which will shift the resonant frequency. Changing the medium's density will also shift the resonant frequency. However, since $g_{1,lat}$ and $g_{2,lat}$ are multiplied by ρ_L, the shift in the resonant frequency will not solely come from the change in the hydrodynamic function. Due to this dependency, beams with higher Reynolds numbers will occasionally have lower resonant frequencies. For example, for a 400x45x12 μm laterally vibrating silicon microcantilever, the resonant frequency of the fundamental mode is 10.14% lower when the beam is operating in water as opposed to air. However, the Reynolds number of this beam in air is 81.1 and is 1102.44 in water. The Reynolds number is higher in water because the Reynolds number is inversely dependent on the kinematic viscosity (the ratio of the dynamic viscosity, η, to the medium's density). Since air has a higher kinematic viscosity than water, the Reynolds number will be lower. Yet, the resonant frequency will be higher due to the lower density of the medium of operation. In general, beams laterally vibrating in media with lower densities or dynamic viscosities will have higher resonant frequencies.

4.2.2 Trends in the Resonant Frequency as a Function of Beam Geometry

The resonant frequency can also be investigated as a function of the geometry of the beam. In a vacuum, Eq. 4-9 shows that the resonant frequency is dependent on b/L^2 with no dependency on the microcantilever's thickness, h. The resonant frequency was reported in Ref. 61 for laterally vibrating microcantilevers of various geometries in both air and water. The lengths of the beams used were 200, 400, 600, 800, and 1000 μm and the widths of the beams used were 45, 60, 75, and 90 μm. An average beam thickness of 14.48 μm was reported. The beam was primarily made of silicon with an average thickness of 12.61 μm. However, there was a 0.67 μm thick layer of thermal oxide on the top of the beam. In addition, several layers of silicon nitride (0.48 μm total) and silicon oxide (0.72 μm total) were also deposited onto the beam in order to mitigate the effects of pinholes on the circuitry used to excite the microcantilever [61]. The density of the beam can be assumed to be approximately that of pure silicon, or 2330 kg/m^3. However, the Young's modulus of the composite system is a function of the Young's modulus of the individual layers. An effective Young's modulus for each beam can be found by varying the Young's modulus and attempting to match the reported resonant frequency in air using Eq. 4-7. The average effective Young's modulus of the microcantilevers used in air is found to be approximately 127.5 GPa. The resonant frequencies in air can then be calculated using Eq. 4-7 and are given in Fig. 4-4.

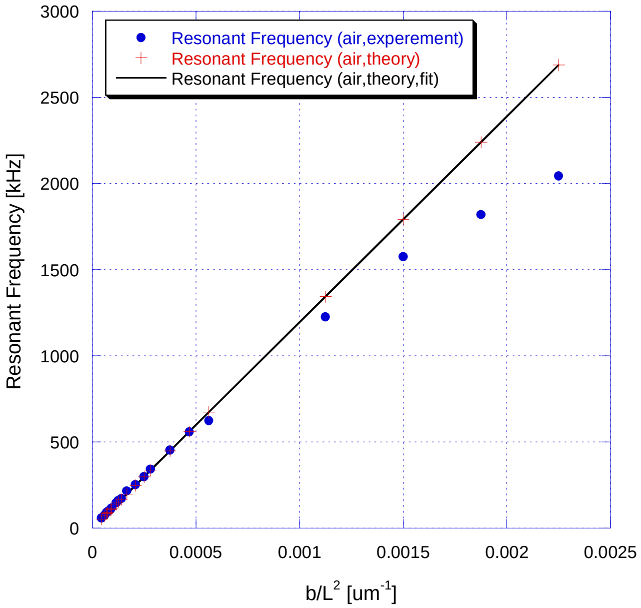

Figure 4-4. The simulated resonant frequencies of laterally vibrating microcantilevers in air compared to experimental data as a function of b/L^2 for widths of 45, 60, 75, and 90 μm, lengths of 200, 400, 600, 800 and 1000 μm, and a thickness of 14.48 μm. The experimental data is from Ref. 61.

Note that the resonant frequencies only follow the b/L^2 dependency for beams where b/L^2<0.001 μm^{-1}. The discrepancy between the theoretically and experimentally determined resonant frequencies for b/L^2>0.001 μm^{-1} is likely due to not taking into account the support compliance and due to the fact that the shear deformation and rotational inertia effects were neglected in the equation of motion. These effects significantly decrease the resonant frequency of the beam when the beam's length is on the order of its width. This particular limit (b/L^2<0.001 μm^{-1}) arises from the particular thickness and materials chosen for the beam, and may be higher or lower for devices made from different materials and with different thicknesses.

Using the effective Young's modulus of 127.5 GPa found previously, the resonant frequencies of each beam in water can also be calculated from Eq. 4-7 and are plotted in Fig. 4-5. Again, the experimentally determined resonant frequencies are lower compared to the theoretically determined resonant frequencies for beams where $b/L^2<0.001$. There is a slight dependency on the beam's aspect ratio. However, for long beams, the b/L^2 linear dependency still holds.

When the microcantilever is laterally vibrating in water, the resonant frequency also has a slight dependency on the microcantilever's thickness. Figure 4-6 shows the simulated resonant frequency of a 400x45 μm beam with a Young's modulus of 127.5 GPa as a function of beam thickness. A thin beam's effective mass will mostly come from the fluid's displaced mass. While the displaced fluid mass ranges from 11%-35% of the total effective mass for the geometries given in Fig. 4-5, the displaced fluid mass will be much larger than the beam mass as the thickness goes to zero. Increasing the thickness will then increase the stiffness more quickly than it increases the effective mass. However, as seen in the chosen geometries of Table 4-1 for thick beams, increasing the thickness increases the effective mass of the microcantilever including the liquid contribution quicker than it increases its stiffness (which is proportional to the thickness and not the fluid properties), which reduces the resonant frequency. For this particular length and width in water, the highest resonant frequency is found when the thickness is 6.548 μm.

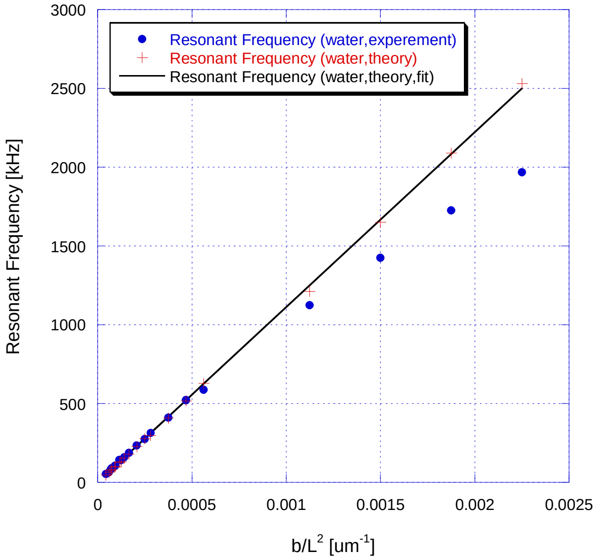

Figure 4-5. The simulated resonant frequencies of laterally vibrating microcantilevers in water compared to experimental data as a function of *b/L*^{2} for widths of 45, 60, 75, and 90 μm, lengths of 200, 400, 600, 800 and 1000 μm, and a thickness of 14.48 μm. The experimental data is from Ref. 61.

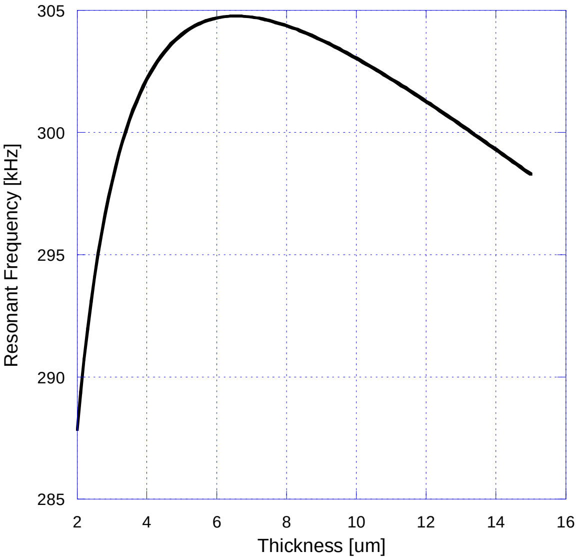

Figure 4-6. The simulated resonant frequency of a laterally vibrating microcantilever 400 μm long and 45 μm wide in water as a function of beam thickness.

In general, shorter and wider beams have higher resonant frequencies following a roughly linear *b/L*^{2} dependency. In air, the resonant frequency has little to no dependence on the beam's thickness. However, in water, the effective mass is not a perfectly linear function of the thickness, which causes the resonant frequency to become dependent on the thickness.

4.2.3 Comparison of the Resonant Frequency of Laterally and Transversely Vibrating Beams

One of the main benefits of using lateral excitation over transverse excitation is that the stiffness and, thus, the resonant frequency for beams vibrating laterally are higher. The other advantage is the increase in the quality factor, which will be investigated in section 4.3. The amount that the resonant frequency increases is a function of the aspect ratio. Since Eq. 4-7 is the same for both laterally and transversely vibrating microcantilevers, the ratio of the two resonant frequencies can be given as

$$\frac{f_{res,lat}}{f_{res,trans}} = \frac{b}{h}\sqrt{\frac{M_{trans}}{M_{lat}}} \qquad \textbf{(Eq. 4-15)}$$

where

$$\begin{aligned} M_{trans} &= \rho_B bhL + Lg_{2,trans} \\ &+ L\frac{\left(g_{1,trans}/\omega_{trans} \right) + \left(\frac{\omega_{trans}}{2} \right)\frac{d}{d\omega}\left(g_{1,trans}/\omega_{trans} \right)}{\left(\rho_B bh + g_{2,trans} + \left(\frac{\omega_{trans}}{2} \right)\frac{d}{d\omega}\left(g_{2,trans} \right) \right)}\left(g_{1,trans}/\omega_{trans} \right). \end{aligned} \qquad \textbf{(Eq. 4-15a)}$$

In vacuum or a low density medium, the effective mass, *M*, is the mass of the beam, and the ratio of the resonant frequencies in Eq. 4-15 is *b/h*. When the viscous damping is significant, the ratio of the resonant frequencies becomes a function of the Reynolds number and fluid density. The predicted ratio of the in-plane and out-of-plane flexural mode's fundamental resonant frequencies of a 400x45x12 μm silicon microcantilever is plotted as a function of percent aqueous glycerol of the operational medium in Fig. 4-7. The ratio cannot be plotted as a function of the Reynolds number as the Reynolds number will be different for the cases of lateral and transverse excitation. However, the Reynolds numbers using both excitations still decrease as the percent aqueous glycerol increases.

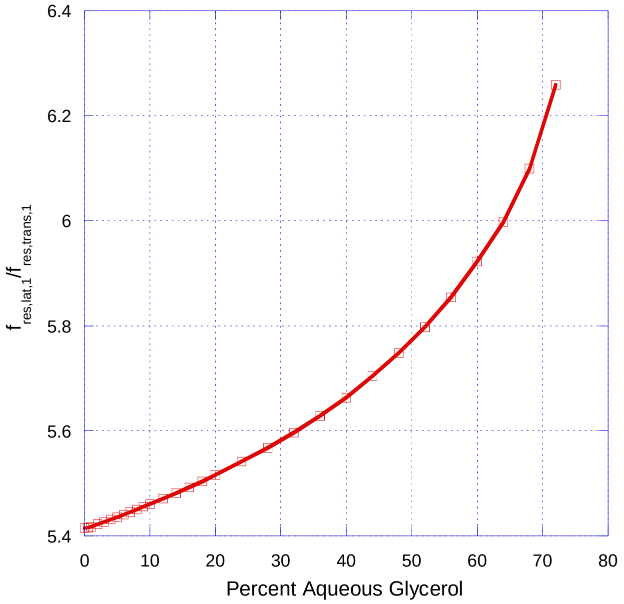

Figure 4-7. The simulated ratio of the fundamental resonant frequency of a 400x45x12 μm silicon microcantilever vibrating laterally to the resonant frequency of the same microcantilever vibrating transversely as a function of percent aqueous glycerol found in the operational medium.

As shown in Fig. 4-7, the increase in the resonant frequency using lateral excitation compared to transverse excitation is larger for lower Reynolds numbers (or higher percent glycerol). However, the overall resonant frequency will also decrease as the Reynolds number is increased. The main increase in the ratio is due to the transverse resonant frequency dropping drastically in media with high viscosities. In general, the resonant frequency of a laterally vibrating microcantilever will be a factor of b/h or higher than the resonant frequency of a transversely vibrating microcantilever. Larger ratios are seen in media of higher density and dynamic viscosity due to the smaller effective mass encountered when exciting the beam laterally.

4.3 Quality Factor

A fundamental problem encountered by microcantilevers operating in the liquid-phase is the dramatic decrease in the microcantilevers' quality factors compared to the quality factors of microcantilevers operating in the gas-phase. This decrease in the quality factor increases the frequency noise (which is proportional to $f_{res,lat}/Q_{lat}$ when operating in an oscillator configuration [89]), thus increasing the limit of detection (LOD) in biochemical sensing applications. The quality factor is defined as 2π times the ratio of the maximum energy stored in a resonating system to the amount of energy dissipated in one cycle [87]. The 2π keeps the definition consistent with a second definition, which is the ratio of the resonant frequency to the 3 dB bandwidth of the system,

$$Q_{lat,3dB} = {}^{f_{res,lat}}\!\big/_{\Delta f_{3dB}} \quad . \qquad \textbf{(Eq. 4-16)}$$

When the loss is low, the two definitions are equivalent.

While the viscous damping from the medium may be the primary source of loss when a microcantilever is vibrating in a viscous liquid medium, it is not the only source of loss. Other common loss sources arise out of the support losses, squeeze film effects, and the viscoelastic damping of the sensing layer if the sensing layer is a viscoelastic material. If the sensing layer is thin enough, the viscoelastic losses can be assumed negligible. The squeeze film effect comes from the beam's interaction with the boundaries of the fluidic cell in which it operates. Since the operational medium in this work is considered infinite, this source of loss will not be considered. The support loss depends on the length of the beam [93]. However, when operating in a viscous liquid medium, the support loss is negligible when compared to the losses from the medium [92].

The frequency spectrum of a 400x45x12 μm silicon microcantilever both laterally and transversely vibrating in water are found using Eq. 4-1 and plotted in Fig. 4-8. Only the resonant frequency of the first in-plane flexural mode is shown, while the resonant frequencies of both the first and second out-of-plane flexural modes are shown. It is noted that in Fig. 4-8 the 3 dB bandwidth of the beam laterally vibrating is about three times larger than that of the same beam vibrating transversely. However, since the resonant frequency is ~5.4 times larger, the quality factor is about two times larger for the laterally vibrating beam compared to the transversely vibrating beam.

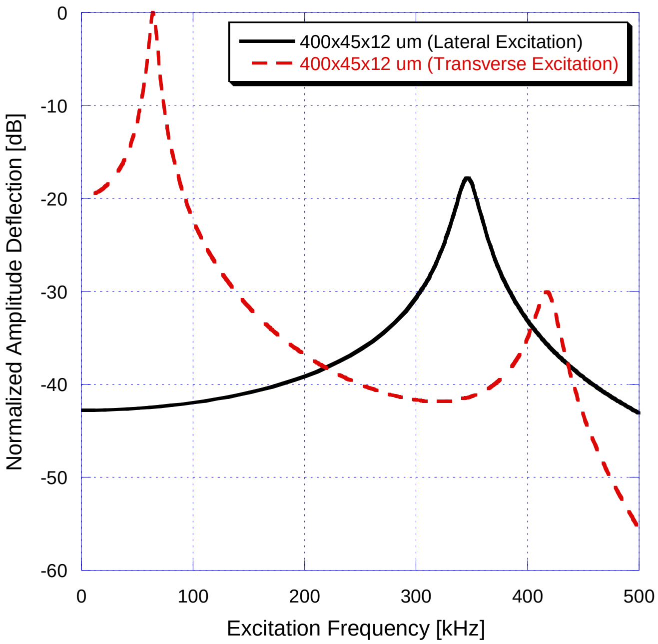

Figure 4-8. The simulated frequency spectrum of a 400x45x12 μm silicon microcantilever in water vibrating both laterally and transversely. Each spectrum is normalized to the maximum tip deflection of the transverse beam, and is excited using the same magnitude force.

If the transversely vibrating beam's length was shortened to 175 μm, the beam's resonant frequency (347.6 kHz) would be the same as that of the 400 μm long laterally vibrating beam in water. The spectra of a 400x45x12 μm beam vibrating laterally and a 175x45x12 μm beam vibrating transversely in water are given in Fig. 4-9. The two beams' quality factors are roughly the same (17.15 for the laterally vibrating beam and 19.41 for the transversely vibrating beam). However, the laterally vibrating beam has more than double the surface area and, thus, can absorb more than two times the mass of a particular analyte into its sensing layer. Whether the frequency shift due to this sorption is larger for laterally vibrating beams compared to transversely vibrating beams is a function of the mass sensitivity and the chemical sensitivity, which will be investigated in section 4.4.

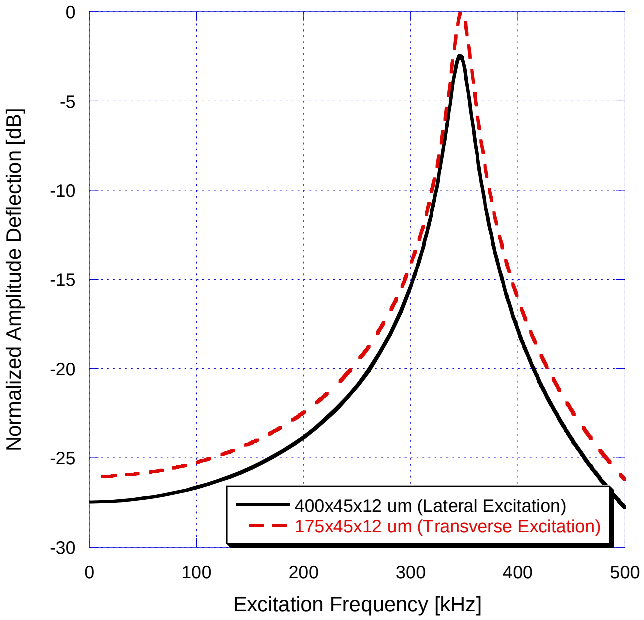

Figure 4-9. The simulated frequency spectrum of a 400x45x12 μm silicon microcantilever in water vibrating laterally and a 175x45x12 μm silicon microcantilever in water vibrating transversely. Both beams are excited by the same force and normalized to the maximum transverse deflection.

An analytical expression for the quality factor is given by Eq. 4-16 when the loss of the medium of operation is low. When determining the quality factor experimentally, the 3 dB bandwidth definition of the quality factor is normally used. In this work, the quality factor will be found using the 3 dB bandwidth definition as opposed to the quality factor found from the energy definition. The resonant frequency was already found in section 4.2. Since the deflection is proportional to the square root of the power stored in the system, the half power bandwidth of the system is the excitation frequency which causes the beam to deflect a factor of ~0.707 that of its maximum value. Two excitation frequencies, ω_{3dB}, satisfy this condition. These two frequencies can be found by solving for ω_{3dB} in

$$\begin{aligned}&\frac{1}{\sqrt{2}}\frac{1}{\sqrt{\left((EI_{lat})(\beta_1 L)^4 - m\omega_{res}{}^2 L^3 - g_{2,lat}\omega_{res}{}^2 L^4\right)^2 + \left(g_{1,lat}\omega_{res}L^4\right)^2}} \\ &= \frac{1}{\sqrt{\left((EI_{lat})(\beta_1 L)^4 - m\omega_{3dB}{}^2 L^3 - g_{2,lat,3dB}\omega_{3dB}{}^2 L^4\right)^2 + \left(g_{1,lat,3dB}\omega_{3dB}L^4\right)^2}}.\end{aligned} \qquad \textbf{(Eq. 4-17)}$$

The procedures to find these two frequencies are again the same for both transverse and lateral excitation. Using the method outlined in Ref. 124, if the hydrodynamic function is assumed to be frequency-independent in the considered frequency range, the quality factor can be given as

$$Q_{lat} = \left(2\left(1 - \sqrt{1 - \frac{g_{1,lat}/\omega_{lat}}{\rho_B bh + g_{2,lat}}}\right)\right)^{-1} \qquad \textbf{(Eq. 4-18)}$$

When the resonant frequency is solved iteratively, the $g_{1,lat}$ and $g_{2,lat}$ values are also found. Thus, no further iteration is needed to evaluate Eq. 4-18. Using a binomial expansion of the denominator of Eq. 4-18,

$$2\left(1 - \sqrt{1 - \frac{g_{1,lat}/\omega_{lat}}{\rho_B bh + g_{2,lat}}}\right) = \frac{g_{1,lat}/\omega_{lat}}{\rho_B bh + g_{2,lat}} + H.O.T.. \qquad \textbf{(Eq. 4-19)}$$

When the loss is low, the quality factor calculated from the 3 dB bandwidth can be approximated as

$$Q_{lat,approx} = 2\pi f_{res,lat}\frac{\rho_B bh + g_{2,lat}}{g_{1,lat}} . \qquad \textbf{(Eq. 4-20)}$$

Equation 4-20 shows that the quality factor is related to the ratio of the amount of beam mass plus displaced mass over the amount of viscous damping. As expected, increasing the beam mass or the displaced mass while maintaining the damping constant will increase the quality factor, while increasing the damping will decrease the quality factor. However, the resonant frequency will also change when the total displaced mass or viscous damping changes.

The nine geometries used in Table 4-1 can be used in comparing and contrasting the different approximations for the quality factor in Table 4-3. From Table 4-3, it is noted that the quality factor is higher for thicker and wider beams with higher Reynolds numbers. Comparing the quality factor found from the spectrum (Eq. 4-16) and from Eq. 4-18, the approximation that the hydrodynamic function is frequency-independent is found to be a good approximation unless the quality factor is very low. The quality factors approximated using Eq. 4-20 are slightly higher than the quality factors calculated from Eq. 4-18.

Aspect Ratio (*h*/*b*)	1	1	1	1/10	1/10	1/10	1/56	1/56	1/56
Reynolds Number (Re)	10	316.23	10000	10	316.23	10000	10	316.23	10000
h (μm)	10.1367	30.8836	97.0374	1.13381	3.01424	9.22685	0.263799	0.598508	1.666543
b (μm)	10.1367	30.8836	97.0374	11.3381	30.1424	92.2685	14.8345	33.6566	93.7166
L (μm)	400	400	400	400	400	400	400	400	400
$Q_{\mathrm{lat,3\ dB}}$ (Eq. 4-16)	4.125	21.770	121.177	0.863	4.652	24.990	0.545	1.438	6.013
Q_{lat} (Eq. 4-18)	4.129	21.850	121.190	0.794	4.654	24.990	0.635	1.437	6.025
Q_{approx} (Eq. 4-20)	4.395	22.103	121.44	1.159	4.918	25.243	0.677	1.740	6.286
Q_{lat} (Eq. 4-18, Using Numerical Results)	4.051	21.874	118.486	0.83	4.597	25.083	0.641	1.319	5.751
Q_{lat} (Eq. 4-18, Using C_R=C_I= 1)	12.884	66.325	367.111	1.954	6.833	34.488	0.893	1.797	6.669

Table 4-3. The quality factors calculated using several different approximations for nine different laterally vibrating beams assuming operation in water, a beam density of 2330 kg/m^3, and a Young's modulus of 169 GPa.

The effects of using the analytical approximation for the hydrodynamic function as opposed to directly using the numerical results are also given in row 9 of Table 4-3. Using Eq. 4-18 to calculate the quality factor, there is a difference of 0.1% to 4.5% in the quality factor in all cases except one. For an aspect ratio of 1/56 and a Reynolds number of 316.23, using the analytical approximation for the hydrodynamic function instead of using the numerical results directly causes a variation in the quality factor by 8.21% (1.437 vs. 1.319) due to the higher viscous damping predicted by the numerical results. Since the viscous damping does not directly depend on the beam mass, variations in the hydrodynamic function affect the denominator of Eq. 4-2 much more than the numerator. Because of this, the quality factor, compared to the resonant frequency, is much more sensitive to variations in the estimate of the hydrodynamic function. Table 4-3 also indicates that using Stokes' solution without correcting for the edge effects and the effects of thickness (row 10) produces drastically larger quality factors due to the neglected additional viscous damping.

The quality factor can also be calculated using the values given for the hydrodynamic function found in Ref. 97. Using the same set of nine geometries found in Table 4-2, the quality factor can be found from Eq. 4-18 using the hydrodynamic function calculated from both methods. Since the derivative of $g_{1,lat}$ and $g_{2,lat}$ with respect to excitation frequency is not given in Ref. 97, Eq. 4-12 will be used to calculate the resonant frequency. These quality factors are given in Table 4-4.

Aspect Ratio (h/b)	1	1	1	0.1	0.1	0.1	0.02	0.02	0.02
Reynolds Number (Re)	10	100	1000	10	100	1000	10	100	1000
h (μm)	10.156	21.176	45.177	1.1534	2.1272	4.3501	0.297	0.497	0.924
b (μm)	10.156	21.176	45.177	11.534	21.272	43.501	14.864	24.859	46.188
L (μm)	400	400	400	400	400	400	400	400	400
Q_{lat} (Γ_{lat} from Eq. 4-4)	4.128	12.436	38.576	0.794	2.688	8.095	0.639	0.97	2.441
Q_{lat} (Γ_{lat} from Ref. 97)	4.027	12.386	38.199	0.932	2.797	8.354	0.667	1.013	2.456

Table 4-4. The quality factors, Q_{lat}, of nine laterally vibrating beams assuming operation in water and a Young's modulus of 169 GPa and a beam density of 2330 kg/m^3, calculated using Eq. 4-4 for Γ_{lat} compared to using the values given in Ref. 97 for $\Gamma_{\text{lat.}}$

Again, there is good agreement (<4.1%) for the quality factors calculated using both methods for Reynolds numbers above 100. When the Reynolds number is 10, the imaginary hydrodynamic function given by Ref. 97 is smaller than what is found using Eq. 4-4. This caused a discrepancy between the two values found for the quality factor of up to 17.4% (0.932 vs. 0.794). However, the geometries that have the largest discrepancies are the ones with quality factors on the order of 1, which is too low a quality factor to use in liquid-phase chemical sensing applications.

4.3.1 Effects of the Medium's Density and Viscosity on the Quality Factor

It is noted in Fig. 4-2 that the sharpness of the peaks of the frequency spectrum is drastically reduced when operating in a viscous liquid medium such as water. Table 4-3 also indicates that microcantilevers with lower Reynolds numbers have lower quality factors. Using Eqs. 4-2, 4-3 and 4-4, Eq. 4-20 can be rewritten as

$$Q_{lat,approx} = \sqrt{\mathrm{Re}}\,\frac{\rho_B}{\rho_L}\frac{h}{b}\frac{\sqrt{2}}{C_I} + \frac{C_R}{C_I} \quad . \qquad \textbf{(Eq. 4-21)}$$

The first term in Eq. 4-21 is proportional to the square root of the Reynolds number multiplied by the aspect ratio and the ratio of the beam's density to the medium's density. The correction factors are functions of the aspect ratio and Reynolds number, and are found in both terms of Eq. 4-21. However, for thin beams, the correction factors are small and the quality factor is roughly proportional to the square root of the Reynolds number. The Reynolds numbers in Table 4-3 vary due to changes in the beam's geometry. The effects of the medium of operation can again be investigated by changing the density and dynamic viscosity of the medium of operation. The trend as a function of the Reynolds number can again be investigated by using the density and dynamic viscosity of various percent aqueous glycerol mixtures (0% to 72%). Figure 4-10 plots the quality factor of a 400x45x12 μm laterally vibrating silicon microcantilever as a function of the Reynolds number. Also shown is the approximation of the quality factor calculated from Eq. 4-21. It is noted in Fig. 4-10 that as the Reynolds number increases, the quality factor increases with a trend approximately equal to the square root of the Reynolds number.

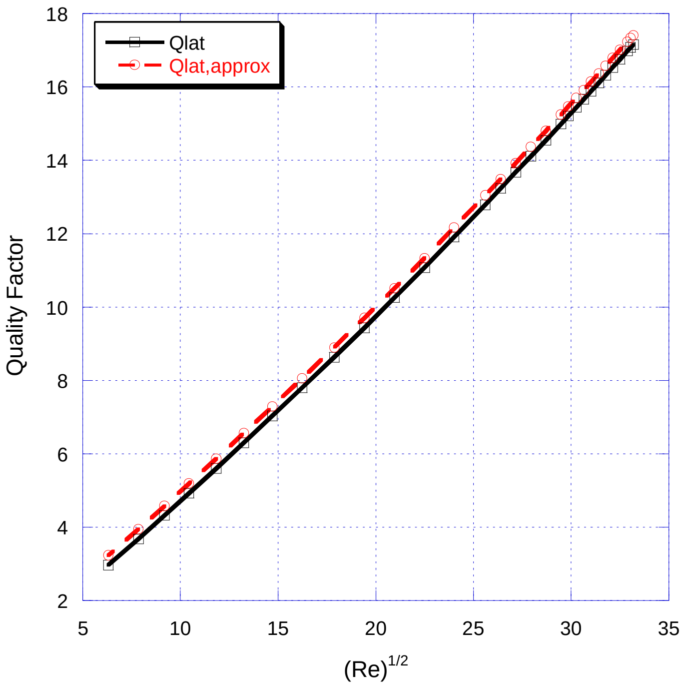

Figure 4-10. The quality factor, Q_{lat}, and its approximation for high Reynolds numbers, $Q_{lat,approx}$, calculated for a 400x45x12 μm laterally vibrating silicon microcantilever as a function of $(\mathrm{Re})^{1/2}$. The Reynolds number is varied by using different values for density and dynamic viscosity corresponding to various aqueous solutions (0% to 72%) of glycerol.

The density of the medium also affects the quality factor independently of the Reynolds number. When the beam mass is much larger than the displaced mass $(\rho_B hbL >> Lg_{2,lat})$, the quality factor can be approximated as

$$Q_{lat,approx} = \frac{\rho_B h\sqrt{\omega_{lat}}}{\sqrt{2\eta\rho_L C_I}} \quad , \ (\rho_B hbL >> Lg_{2,lat}). \qquad \textbf{(Eq. 4-22)}$$

The quality factors calculated from Eq. 4-22 will be lower than those calculated from Eq. 4-18, as the effects of the displaced fluid are not accounted for. Equation 4-22 shows, contrary to intuition, that the drop in the system's quality factor when operating in water as opposed to air mostly arises from the increase in the medium's density (1.205 to

998.23 kg/m^3 at 20° C, an increase of a factor of 828.4) instead of the increase in the medium's dynamic viscosity (0.01827 to 1 cP at 20° C, an increase of a factor of 54.7) [125]. As shown in section 4.2, the increase in the medium's dynamic viscosity and density will also decrease the resonant frequency, further decreasing the quality factor. Equations 4-21 and 4-22 also explain why the quality factor in air is higher, even though the Reynolds number is lower. In general, the quality factor of laterally vibrating microcantilevers decreases as the medium's density or dynamic viscosity increases.

4.3.2 Trends in the Quality Factor as a Function of Beam Geometry

The quality factor can also be investigated as a function of the beam's geometry. Since the resonant frequency in vacuum is linearly dependent on b/L^2, using Eq. 4-22 indicates that a good approximation for the dependency of the quality factor on the beam's geometry is $hb^{1/2}/L$. (This dependency might not hold when operating in highly viscous liquid media). The quality factors for various geometries are calculated using Eq. 4-18 as a function of $b^{1/2}/L$ in air and compared in Fig. 4-11 to the experimentally measured quality factors reported in Ref. 61. The hydrodynamic function is assumed given by Eq. 4-4. The trend in the thickness is neglected since the data in Ref. 61 only used one thickness of 14.48 μm. The Young's modulus is again assumed to be 127.5 GPa. There is a large discrepancy in Fig. 4-11 for the quality factor in air when $(b^{1/2}/L)>0.03$ μm$^{-1/2}$. This difference could be attributed to neglecting the shear and rotational inertia, neglecting the support loss, and neglecting the support's deformation.

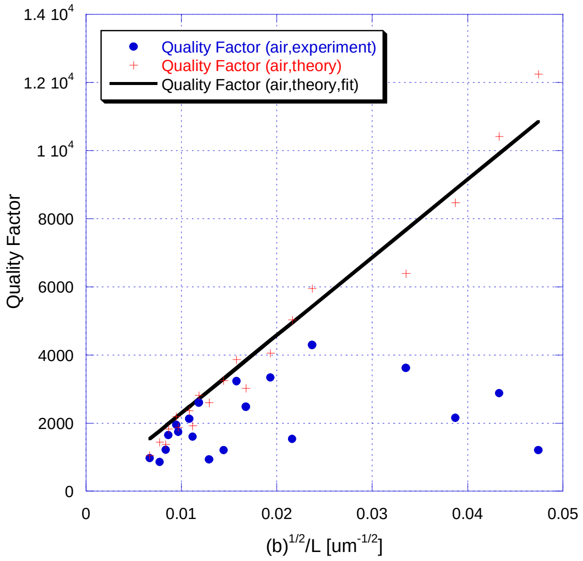

Figure 4-11. Simulated and experimentally determined quality factors of laterally vibrating microcantilevers in air. The width is varied between 45 and 90 μm, the length from 200 to 1000 μm, and the thickness is fixed at 14.48 μm. Discontinuities in the theoretical data arise from variations in the length. The experimental data is from Ref. 61.

The support loss is larger for shorter beams, and in air, may be the dominant source of loss for particular geometries [92]. For longer beams, the quality factors are roughly proportional to b/L^2.

The quality factors for the same geometries shown in Fig. 4-11 are calculated using Eq. 4-18 and plotted in Fig. 4-12 as a function of $b^{1/2}/L$ in water and compared to the experimentally determined quality factors reported in Ref. 61. The experimentally determined quality factors of beams laterally vibrating in water are found to follow the theoretically predicted trend. Shorter and wider beams were found to have higher quality factors. Quality factors as high as 66.8 were reported in Ref. 61 for laterally vibrating microcantilevers, whereas normal quality factors for transversely vibrating beams in water are on the order of 10 [24,45,71].

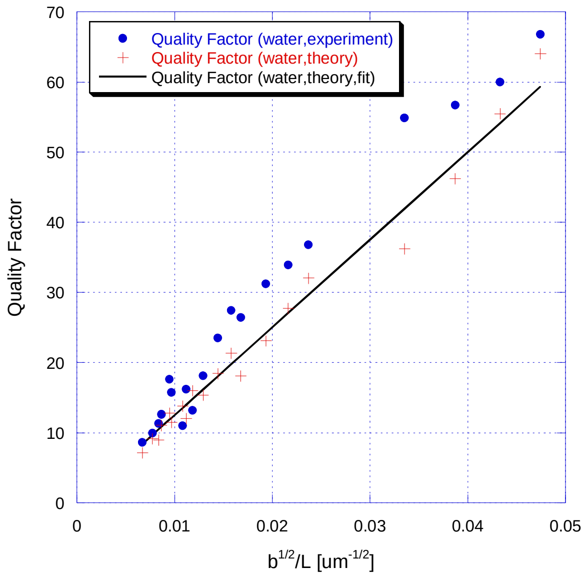

Figure 4-12. Simulated and experimentally determined quality factors of laterally vibrating microcantilevers in water. The width is varied between 45 and 90 μm, the length from 200 to 1000 μm, and the thickness is fixed at 14.48 μm. Discontinuities in the theoretical data arise from the variations in the length. The Young's modulus of the beam is assumed to be 127.5 GPa. The experimental data is from Ref. 61.

The beam's thickness will also change the quality factor. Equation 4-22 appears to show that the quality factor has a linear dependency with respect to the thickness. However, changing the thickness will also change the aspect ratio, which in turn will change the value of C_I. For small thicknesses and high Reynolds numbers, the quality factor will be roughly linearly dependent on the thickness. However, as the thickness increases, this trend will not continue due to the additional fluid damping encountered on the leading edge of the beam. The quality factor of a microcantilever 400 μm long and 45 μm wide as a function of beam thickness in water is given in Fig. 4-13. It is assumed that the beam's Young's modulus is 127.5 GPa. In general, when exciting a microcantilever laterally, shorter, thicker, and wider beams will have higher quality factors.

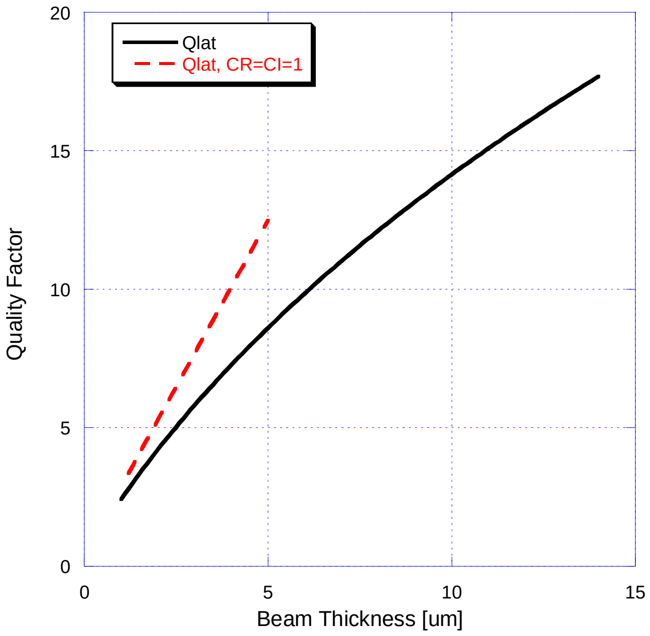

Figure 4-13. Simulated quality factors for a beam 400 μm long and 45 μm wide laterally vibrating in water as a function of beam thickness. Also plotted is the quality factor calculated assuming $C_R = C_I = 1$ (Stokes' solution).

4.3.3 Comparison of the Quality Factor of Laterally and Transversely Vibrating Beams

The quality factor, like the resonant frequency, also increases when exciting the beam in the in-plane direction. The improvement is again a function of both the microcantilever's aspect ratio and the properties of the medium of operation. Using the low-loss approximation for the quality factor calculated from Eq. 4-20, the ratio of the quality factor calculated for a particular geometry undergoing lateral excitation to that of the same beam undergoing transverse excitation can be written as

$$\frac{Q_{lat,approx}}{Q_{trans,approx}} = \frac{\rho_B bh + g_{2,lat}}{\rho_B bh + g_{2,trans}} \frac{\Gamma_{I,trans}}{\Gamma_{I,lat}} \qquad \textbf{(Eq. 4-23)}$$

The improvement in the quality factor is found to be the product of the ratio of the total mass (the beam mass plus the displaced mass) and the ratio of the imaginary parts of the hydrodynamic functions. Note that the first term is the laterally vibrating beam's total mass over the transversely vibrating beam's total mass. This factor is less than one (for $h/b<1$), as the transversely vibrating beam will displace more fluid than a laterally vibrating beam.

When $g_{2,lat}$ and $g_{2,trans}$ are small (for low density and viscosity media) the ratio of the quality factors is approximately the ratio of the imaginary part of the hydrodynamic function of the transversely vibrating beam to the laterally vibrating beam. This ratio of the two imaginary parts of the hydrodynamic functions is usually much greater than one. The ratio can be investigated as a function of the medium by again varying the density and dynamic viscosity of the medium using various concentrations of aqueous glycerol. The ratio of the quality factors of a 200x45x12 μm laterally vibrating silicon microcantilever is plotted as a function of percent aqueous glycerol in Fig. 4-14. It is noted in Fig. 4-14 that the improvement in the quality factor when using lateral excitation is a function of the operational medium. The improvement is larger for higher Reynolds numbers or lower viscosity media.

The improvement is also a function of the beam's geometry. Over the range of geometries investigated in Ref. 61, the predicted improvement in the quality factor in water ranged from 1.55 for the beam with the longest length and smallest width (1000x45x14.48 μm) to 2.53 for the shortest and widest beam (200x90x14.48 μm). This indicates that when comparing the quality factors of laterally and transversely vibrating beams, the improvement is larger for shorter and wider beams.

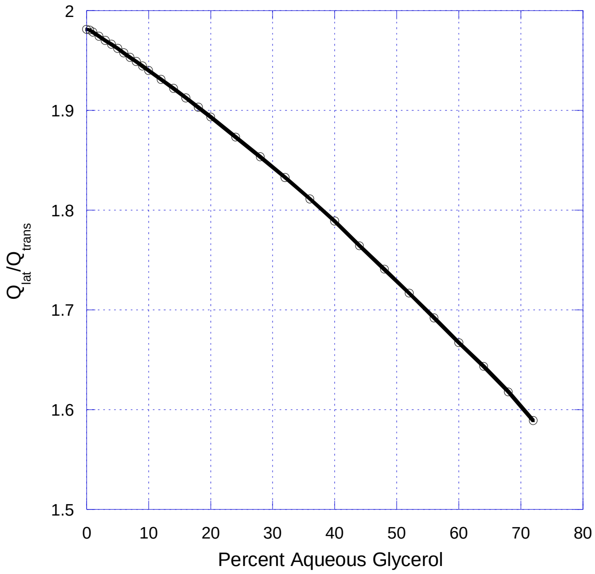

Figure 4-14. The ratio of the quality factors of a laterally and a transversely vibrating beam for a 200x45x12 μm silicon microcantilever as a function of percent aqueous glycerol in the operational medium.

In air, the improvement is much higher, with a predicted increase ranging from 3 to 4.5 for the beams studied in Ref. 61. However, this again neglects the effects of support loss. In general, the quality factor is higher for laterally vibrating beams compared to transversely vibrating beams. The improvement is larger for media with lower densities and dynamic viscosities. The improvement is also larger for shorter and wider beams.

4.4 Mass Sensitivity

In sensor applications, changes in the operational environment or changes in the mass of the microcantilever can be detected through changes in the resonant frequency. The resonant frequency’s sensitivity to changes in mass, or the mass sensitivity, can be defined as [12]

$$S_m = \left| \frac{\Delta f}{\Delta m} \right| . \quad \textbf{(Eq. 4-24)}$$

Using Eq. 4-1, the shift in the fundamental resonant frequency of a 400x45x12 μm laterally vibrating silicon microcantilever in water due to an increase in beam mass of ~5 nanograms (a 1% increase in beam density) is shown in Fig. 4-15. This added mass increase shifts the resonant frequency by ~1.40 kHz, and also increases the deflection and stored energy (and thus quality factor) of the system. Note that by changing the density, the added mass is assumed to be uniformly distributed over the entire length of the beam.

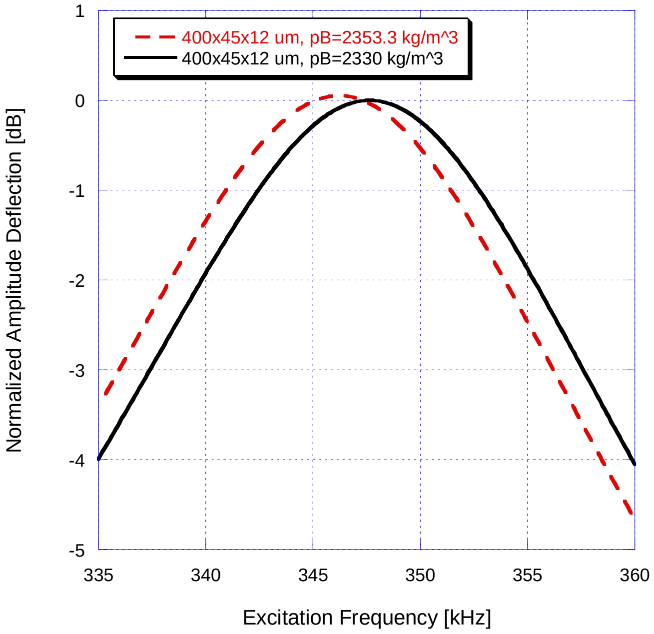

Figure 4-15. The simulated frequency spectrum of a 400x45x12 μm silicon microcantilever laterally vibrating in water. The spectrum is also plotted when the mass of the beam is uniformly increased over the length by 1%.

Adding the same amount of mass to just the tip of the microcantilever will cause a larger shift in the resonant frequency. However, it will be assumed in this work that the added mass is always uniformly distributed over the length of the beam.

Figure 4-16 shows the predicted frequency shift for four different geometries in water as a function of the change in the beam's mass in air. Note that the magnitude of the slope of the lines in Fig. 4-16 represents the mass sensitivity. The Young's modulus of the beam is assumed to be 169 GPa and the density of the beam is assumed to be 2330 kg/m^3. Note that the shift in the resonant frequency is roughly linear as a function of the change in beam mass, and the slope varies for different beam geometries. The frequency shift can be non-linear for large changes in mass. However, it will be assumed, in this work, that the mass absorbed by the sensing layer is always small enough as to have a linear frequency response.

The frequency shift of the four beams given in Fig. 4-16 as a function of the change in beam mass can also be investigated in water and is shown in Fig. 4-17. Note that there is now a slight dependence on the width. An analytical expression for the mass sensitivity can be found using the same procedures described in Ref. 124, using different values for the moment of inertia (I_{lat}), $g_{1,\mathrm{lat}}$, and $g_{2,\mathrm{lat}}$. The change in the resonant frequency as a function of change in mass is given by

$$\Delta f = \Delta m\left(f_{res,lat}\right)\left(\lambda_{m,lat}\right) \qquad \textbf{(Eq. 4-25)}$$

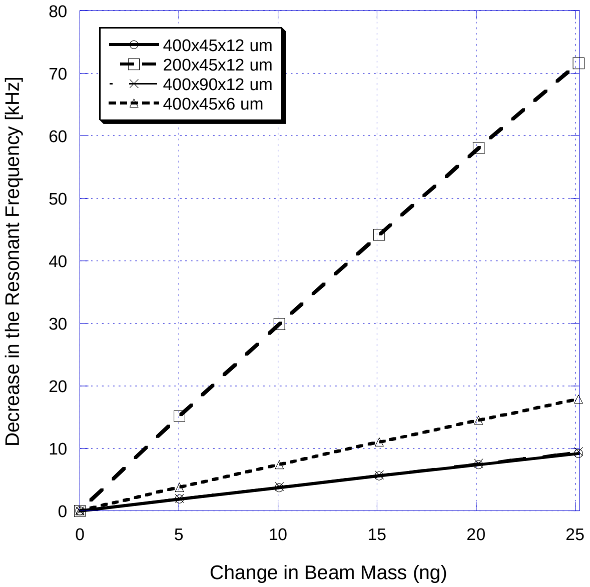

Figure 4-16. Predicted decrease in the resonant frequency of four microcantilevers in air as a function of the change in beam mass. Note that shorter and thicker beams are more sensitive to changes in beam mass (e.g., for a 400x45x12 μm silicon beam, S_m=0.369 Hz/pg while a 200x45x12 μm silicon beam will have a S_m=2.9 Hz/pg).

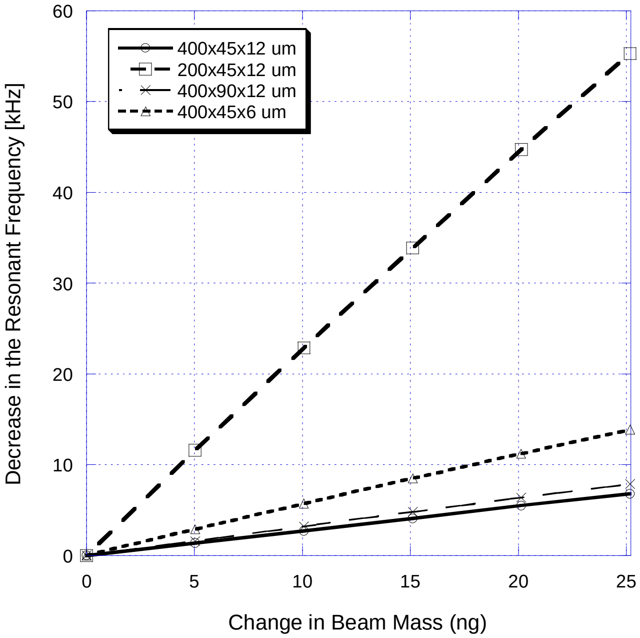

Figure 4-17. Predicted decrease in the resonant frequency of four microcantilevers in water as a function of the change in beam mass. Note that shorter and thicker beams are more sensitive to changes in beam mass. (e.g., for a 400x45x12 μm silicon beam, S_m=0.277 Hz/pg while a 200x45x12 μm silicon beam will have a S_m=2.33 Hz/pg).

where the normalized mass sensitivity is given by

$$\lambda_{m,lat} = \frac{\left(g_{1,lat}/\omega_{lat}\right)\left(g_{1,lat}/\omega_{lat} + \left(\frac{\omega_{lat}}{2}\right)\frac{d}{d\omega}\left(g_{1,lat}/\omega\right)\right)EI_{lat}}{2kLM_{lat}\left(\rho_B bhL + Lg_{2,lat} + L\left(\frac{\omega_{lat}}{2}\right)\frac{d}{d\omega}\left(g_{2,lat}\right)\right)^2} - \frac{1}{2M_{lat}}.$$

(Eq. 4-26)

The second term in Eq. 4-26 is the effect of the mass increase on M_{lat}, while the first term arises out of the fact that in Eq. 4-7b, the effect of the viscous damping is normalized to the total mass. When the beam's mass is increased, the ratio of the viscous damping to the total mass will be smaller, causing the resonant frequency to increase. This effect is modeled by the first term in Eq. 4-26. However, when the beam's mass is increased the effective mass will also increase which will result in a decrease in the resonant frequency. This effect is modeled by the second term in Eq. 4-26. When the beam mass is much larger than the displaced mass and viscous damping, the second term in Eq. 4-26 dominates the first term. The mass sensitivity can then be approximated as

$$S_{m,approx} = \left|\frac{(\beta_i L)^2}{2\pi}\frac{\sqrt{Eb^3hL^{-3}}}{4\sqrt{3}\left(M_{lat}\right)^{3/2}}\right|$$

(Eq. 4-27)

The approximation for the mass sensitivity given by Eq. 4-27 can be compared in Table 4-5 to the exact value given by Eq. 4-25 for the nine geometries given in Table 4-1.

Aspect Ratio (*h/b*)	1	1	1	1/10	1/10	1/10	1/56	1/56	1/56
Reynolds Number (Re)	10	316.23	10000	10	316.23	10000	10	316.23	10000
h (μm)	10.1367	30.8836	97.0374	1.13381	3.01424	9.22685	0.263799	0.598508	1.666543
b (μm)	10.1367	30.8836	97.0374	11.3381	30.1424	92.2685	14.8345	33.6566	93.7166
L (μm)	400	400	400	400	400	400	400	400	400
S_m (Eq. 4-24) Hz/ pg	0.156	0.0755	0.0255	0.138	0.925	0.422	0.243	1.206	1.981
$S_{m,approx}$ (Eq. 4-27) Hz/ pg	0.165	0.0757	0.0255	0.538	0.965	0.422	0.206	1.801	2.033
S_m (Eq. 4-27) Using Numerical Results for Γ_{lat} Hz/ pg	0.162	0.075	0.025	0.474	0.959	0.426	0.167	1.623	2.099
S_m (Eq. 4-24) C_R=C_I=1 Hz/ pg	0.403	0.146	0.0473	1.204	1.173	0.478	0.333	1.756	2.096

Table 4-5. The mass sensitivities of nine laterally vibrating beams calculated using several different approximations assuming operation in water and a Young's modulus of 169 GPa and a beam density of 2330 kg/m^3. Higher mass sensitivities could be obtained if the length of the beam was assumed to be shorter (i.e. 200 μm).

It is noted in Table 4-5 that the approximation given by Eq. 4-27 for the mass sensitivity works well when the beam thickness or the Reynolds number is large. This is because the second term in Eq. 4-26 dominates the first term when the viscous damping is small or the beam mass is much larger than the displaced mass. However, it is inappropriate to use the approximation when viscous damping contributes significantly to the effective mass as given by Eq. 4-7b. Using the numerical results instead of the analytical approximation for the hydrodynamic function (row 8 in Table 4-5) also causes up to a 19% variation in the value of the mass sensitivity. However, this variation is again smaller for thicker beams and beams with higher Reynolds numbers. Using Stokes' solution (row 9 in Table 4-5) causes a large overestimate of the mass sensitivity due to the unaccounted displaced mass and viscous damping.

The mass sensitivities are also calculated using both values for the hydrodynamic function given by Eq. 4-27 and the values given in Ref. 97. Equation 4-27 is used for the comparison as the derivative of $g_{1,lat}$ and $g_{2,lat}$ again are not given in Ref. 97. The hydrodynamic function is also considered frequency-independent when calculating the effective mass. These mass sensitivities are compared in Table 4-6 for the nine geometries given in Table 4-2. For thick beams (*h/b*=1, or when lateral excitation and transverse excitation are the same) and the highest Reynolds number (1000), there is good agreement (<1.9%) for the mass sensitivity calculated using the two hydrodynamic functions. However, for thin beams and low Reynolds numbers there is a large discrepancy (up to 67.2%) due to the variations in the effective mass. These beams are again the geometries that have quality factors on the order of 1, and are the geometries that are not appropriate for sensing applications.

Aspect Ratio (*h/b*)	1	1	1	0.1	0.1	0.1	0.02	0.02	0.02
Reynolds Number (Re)	10	100	1000	10	100	1000	10	100	1000
h (μm)	10.156	21.176	45.177	1.1534	2.1272	4.3501	0.297	0.497	0.924
b (μm)	10.156	21.176	45.177	11.534	21.272	43.501	14.864	24.859	46.188
L (μm)	400	400	400	400	400	400	400	400	400
S_m (Eq. 4-27) Hz/pg	0.161	0.104	0.053	0.453	0.995	0.778	0.179	1.047	2.137
S_m (Eq. 4-27 Using Γ_{lat} from Ref. 97) Hz/pg	0.160	0.103	0.052	0.503	1.014	0.782	0.223	1.071	2.151

Table 4-6. The approximate mass sensitivities ($S_{m,approx}$) of nine laterally vibrating beams assuming operation in water, a Young's modulus of 169 GPa , and a beam density of 2330 kg/m^3 calculated using Eq. 4-4 for the values of the hydrodynamic function compared to using the values given in Ref. 97 for the values of the hydrodynamic function.

4.4.1 Effects of the Medium's Density and Viscosity on the Mass Sensitivity

In air, when $M_{lat} \cong \rho_B Lbh$, the mass sensitivity can be approximated as

$$S_{m,air} \cong \frac{(\beta_i L)^2}{2\pi} \frac{\sqrt{E}}{4\sqrt{3}\rho_B{}^{3/2}} \frac{1}{hL^3} . \qquad \textbf{(Eq. 4-28)}$$

The mass sensitivity decreases in viscous operating environments. Assuming that Eq. 4-27 can be used to approximate the mass sensitivity, using Eqs. 4-27, 4-28 and Eq. 4-14, the decrease in the mass sensitivity can be given as

$$\frac{S_{m,approx}}{S_{m,air}} = \left(1 + \frac{\rho_L}{\rho_B} \frac{b}{h} \frac{1}{\sqrt{\mathrm{Re}}} \left(\frac{\sqrt{2}}{2} C_R + C_I{}^2 \left(2\sqrt{\mathrm{Re}} \frac{h\rho_B}{b\rho_L} + \sqrt{2} C_R \right)^{-1} \right) \right)^{-3/2} . \qquad \textbf{(Eq. 4-29)}$$

It is noted from Eq. 4-29 that, if C_R and C_I are one, increasing the Reynolds number should increase the mass sensitivity in water. This trend does not hold for thick beams in Tables 4-5 and 4-6 due to the fact that C_R and C_I are large and dependent on the Reynolds number.

The changes in mass sensitivity as a function of the Reynolds number in Tables 4-5 and 4-6 are again due to changes in the beam geometry. To investigate the changes in the mass sensitivity as a function of the medium's properties, the medium's density and dynamic viscosity can again be varied by assuming varying concentrations of percent glycerol. The mass sensitivity of a 200x45x12 μm laterally vibrating silicon microcantilever as a function of Reynolds number, using aqueous concentrations of glycerol (0% to 72%) is given in Fig 4-18.

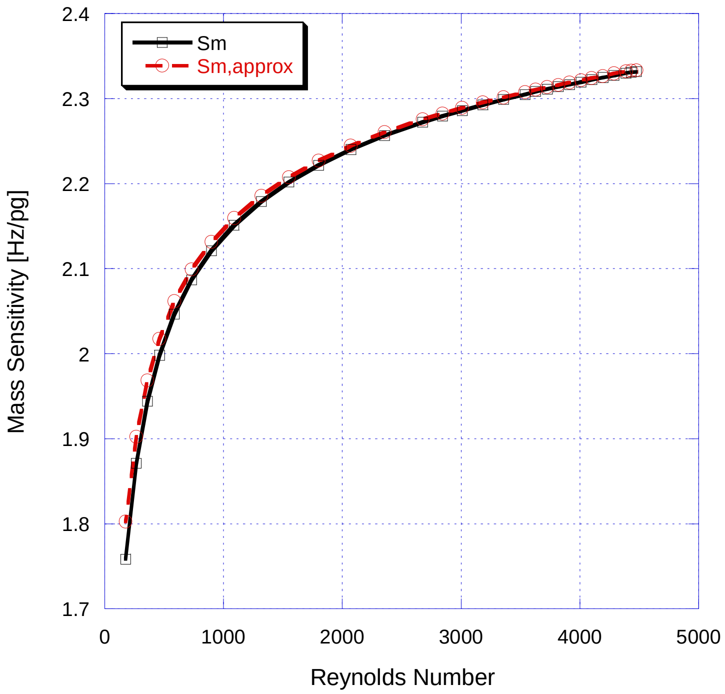

Figure 4-18. The mass sensitivity of a 200x45x12 μm laterally vibrating silicon microcantilever (*E*=169 GPa) calculated using the exact expression (Eq. 4-24) and the approximate expression valid for high Reynolds numbers (Eq. 4-27) as a function of Reynolds number. The Reynolds number is varied by using different values for density and dynamic viscosity corresponding to various aqueous solutions (0-72%) of glycerol.

It is noted in Fig. 4-18 that, as the Reynolds number decreases, the mass sensitivity decreases. It can also be seen that the variation in the predicted values of S_m caused by neglecting the first term in Eq. 4-26 will be larger when the Reynolds number is decreased. This is because the viscous damping's contribution to the effective mass increases as the Reynolds number decreases, while the beam mass remains constant.

Again, it is noted from Eq. 4-29 that the medium's density affects the mass sensitivity in a way that is independent of the Reynolds number. For example, increasing the medium's density from that of air to that of water, the mass sensitivity of a 400x45x12 μm laterally vibrating microcantilever decreases by a factor of 1.38, while the

Reynolds number increases from 81.1 to 1102.44. In general, the mass and chemical sensitivities of laterally vibrating microcantilevers will be lower for media with higher dynamic viscosities or densities.

4.4.2 Trends in the Chemical Sensitivity as a Function of Beam Geometry

From Eq. 4-28, in air the mass sensitivity is proportional to the inverse of hL^3. As shown in Fig. 4-16, shorter and thinner beams will then have higher mass sensitivities. When dealing with dynamically driven microcantilever chemical sensors, the sensitivity to chemicals in the operational environment, or the chemical sensitivity, is also of interest. The chemical sensitivity is defined as the change in the resonant frequency of the microcantilever as a function of the ambient concentration, C_A, of a particular analyte in the medium of operation [89], or

$$S_c = \left|\frac{\Delta f}{C_A}\right|. \qquad \textbf{(Eq. 4-30)}$$

The chemical sensitivity can be found as a function of the mass sensitivity [9] as

$$S_c = KLbh_2S_m \qquad \textbf{(Eq. 4-31)}$$

where K is the partition coefficient of the sensing layer in the operational medium and h_2 is the sensing layer's thickness. Finding the chemical sensitivity requires knowing the properties of the sensing layer, which is outside the scope of this investigation. However, since the chemical sensitivity is proportional to the mass sensitivity, the trends in both the mass sensitivity and chemical sensitivity as a function of the medium of operation will be the same (assuming K remains constant) and the trends in the chemical sensitivity as a function of the beam's geometry will be the trends in the mass sensitivity multiplied by a factor of $KLbh_2$. It will be assumed that $h>>h_2$. A normalized chemical sensitivity that does not depend on the properties of the sensing layer, $\overline{S}_c$, can be found

$$\overline{S}_c = S_c/(Kh_2)\,. \qquad \textbf{(Eq. 4-32)}$$

Assuming S_m is roughly linearly dependent with respect to $h^{-1}L^{-3}$, the chemical sensitivity will be proportional to (h_2/h) multiplied by (b/L^2). Since b/L^2 is the same geometric dependency as the resonant frequency, the chemical sensitivity will always be roughly proportional to the resonant frequency. The chemical sensitivity will also be proportional to the ratio of the beam's thickness to the sensing layer's thickness.

Unfortunately, no experimental data for the mass sensitivity or chemical sensitivity was published in Ref. 61. However, $\overline{S}_c$ in water can still be predicted and plotted as a function of b/L^2 for the geometries given in Ref. 61. Figure 4-19 shows that shorter and wider beams, assuming that the same sensing layer type and thickness are used, will be more sensitive to changes in analyte concentration compared to longer and narrower beams.

Note that decreasing the length and increasing the width improve both the mass sensitivity and the quality factor. There is a predicted h^{-1} linear dependency on the mass sensitivity and chemical sensitivity if the sensing layer thickness is held constant. Thinner beams will have a smaller mass and the sorbed analyte mass by the sensing layer will thus change the average beam density by larger amounts.

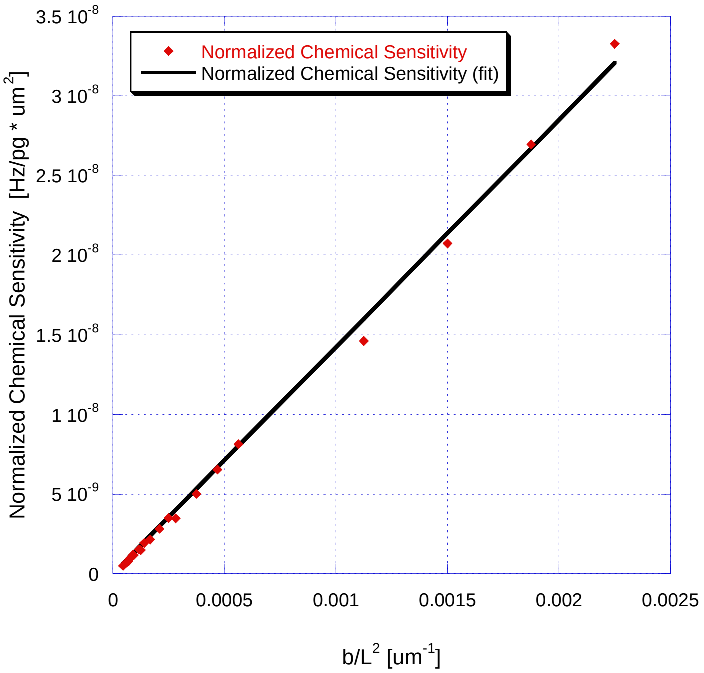

Figure 4-19. Predicted normalized chemical sensitivities of laterally vibrating microcantilevers in water. The width is varied between 45 and 90 µm, the length from 200 to 1000 µm, and the thickness is fixed at 14.48 µm. The beam's Young's modulus is assumed to be 127.5 GPa. If the normalized chemical sensitivity is multiplied by Kh_2, a chemical sensitivity in Hz per concentration can be found.

However, thinner beams will have lower quality factors. As a result, there is a predicted tradeoff between the chemical sensitivity and the quality factor when choosing the beam's thickness.

The limit of detection (LOD) for a given analyte is often defined as three times the ratio of the device/system frequency noise to the chemical sensitivity, and represents a measure of performance for a chemical sensor. When operating in an oscillator configuration, the system's frequency noise is proportional to $f_{res,lat}/Q_{lat}$ [89]. In terms of the normalized chemical sensitivity, the limit of detection satisfies the following relationship:

$$LOD \propto \frac{3f_{res,lat}}{Q_{lat}\bar{S}_c}. \qquad \textbf{(Eq. 4-33)}$$

This parameter is plotted as a function of beam thickness for a 400 μm long and 45 μm wide beam in Fig. 4-20. The Young's modulus of the beam is assumed to be 127.5 GPa. It is noted from Fig. 4-20 that the best thickness (the lowest detection limit) using the parameter given in Eq. 4-33 is 2.6 μm. The quality factor's relationship with respect to the beam's thickness is not linear when the thickness is large, whereas the mass sensitivity and normalized chemical sensitivity are linear with respect to the beam's thickness. When trying to minimize the limit of detection by varying the beam's thickness, the optimal thickness will be a function of the beam's length, the beam's width, and the viscosity and density of the medium of operation.

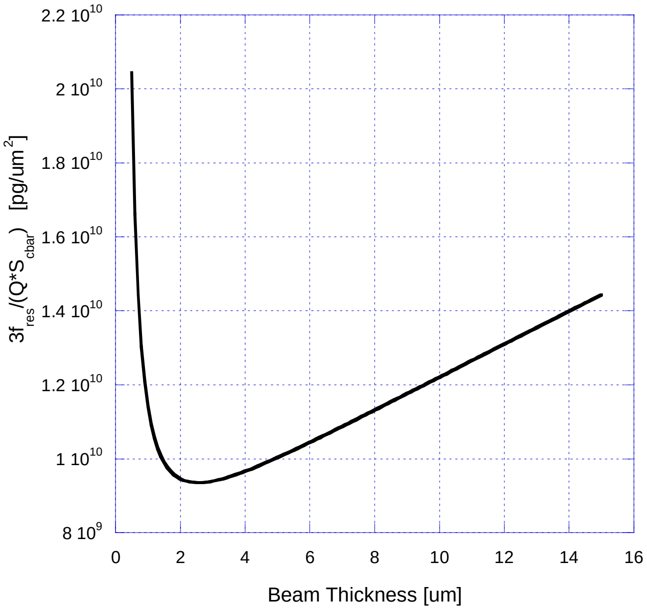

Figure 4-20. The parameter $3f_{res,lat}/(Q_{lat}\bar{S}_c)$ plotted as a function of beam thickness for a laterally vibrating beam 400 μm long and 45 μm wide laterally vibrating in water. The parameter $3f_{res,lat}/(Q_{lat}\bar{S}_c)$ is proportional to the limit of detection (LOD) of a laterally vibrating microcantilever in an oscillator configuration.

In chemical sensor applications, the beam's geometry should be designed with both the chemical sensitivity and the quality factor taken into account, as the system's frequency noise varies proportional to $f_{res,lat}/Q_{lat}$ [89]. However, as $3f_{res,lat} / (Q_{lat} \overline{S}_c)$ doesn't increase quickly with respect to thickness for thicknesses larger than 2.6 μm in Fig. 4-19, the limit of detection does not vary by much if the thickness is increased in order to reach a particular quality factor needed for a particular sensing application.

In general, the mass sensitivity is roughly proportional to the inverse of hL^3 and the chemical sensitivity is roughly proportional to h_2/h multiplied by b/L^2. Shorter and wider beams have higher chemical sensitivities along with higher quality factors. Thinner beams with the same sensing layer thickness will have higher chemical sensitivities but lower quality factors. The thickness must then be chosen taking into account its effect on both the chemical sensitivity and quality factor.

4.4.3 Improved Mass Sensitivity using Lateral Excitation Compared to Transverse Excitation

The mass sensitivity is also higher for microcantilevers laterally vibrating compared to microcantilevers transversely vibrating. The ratio of the mass sensitivity for a laterally vibrating beam compared to that of a transversely vibrating beam is

$$\frac{S_{m,lat}}{S_{m,trans}} \approx \frac{\lambda_{m,lat}}{\lambda_{m,trans}} \frac{b}{h} \sqrt{\frac{M_{trans}}{M_{lat}}} \qquad \textbf{(Eq. 4-34)}$$

Equation 4-34 shows that the increase in the mass sensitivity (and chemical sensitivity) is approximately the increase in relative mass sensitivity multiplied by the increase in the stiffness and by the increase in the square root of the total effective mass. If the second term in Eq. 4-26 dominates the first term for both the lateral and transverse normalized mass sensitivity, the ratio of the two normalized mass sensitivities can be approximated as

$$\frac{\lambda_{m,lat}}{\lambda_{m,trans}} \cong \frac{M_{trans}}{M_{lat}} \qquad \textbf{(Eq. 4-35)}$$

The increase in the mass sensitivity when operating in the in-plane flexural mode compared to the out-of-plane flexural mode is then approximately

$$\frac{S_{m,lat}}{S_{m,trans}} \approx \frac{b}{h}\left(\frac{M_{trans}}{M_{lat}}\right)^{3/2} \qquad \textbf{(Eq. 4-36)}$$

The effective mass of transversely vibrating beams is larger than that of laterally vibrating beams. Thus, the increase in the mass sensitivity when using lateral excitation compared with transverse excitation will be equal to or greater than *b/h*.

For media with low dynamic viscosities and densities, Eq. 4-36 is equal to *b/h*. As the operational medium becomes more viscous, the ratio of the effective masses should become larger. The ratio of the mass sensitivities of a 200x45x12 μm beam and a 400x45x12 μm beam with Young's moduli of 127.5 GPa as a function of percent aqueous glycerol is given in Fig. 4-21. It is noted from Fig. 4-21 that, for higher viscosities (lower Reynolds numbers), microcantilevers vibrating laterally will have higher mass sensitivities compared to beams vibrating transversely. The mass sensitivity will still decrease as the viscosity of the medium increases. However, Fig. 4-21 indicates that the rate at which the mass sensitivity decreases is smaller for laterally vibrating beams compared to transversely vibrating beams. For example, a 400x45x12 μm silicon beam transversely vibrating with a Young's modulus of 127.5 GPa will have a mass sensitivity of 88.69 Hz/ng in air and a mass sensitivity of 20.84 Hz/ng in water (a 76.5% drop). The same beam laterally vibrating will have a mass sensitivity of 333.6 Hz/ng in air and a mass sensitivity of 239.6 Hz/ng in water (only decreasing by 28.2%).

The ratio of the mass sensitivities is also a function of the beam's geometry. For the beams given in Ref. 61, the increase in the predicted mass sensitivity ranged from 7.3 to 35.8 using lateral as opposed to transverse excitation. The increase in mass sensitivity was higher for wider and longer beams.

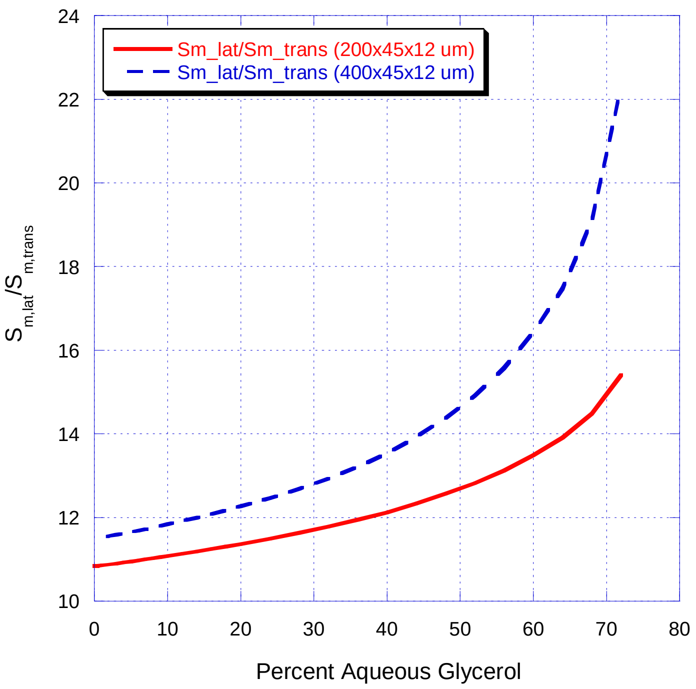

Figure 4-21. The ratio of the mass sensitivities of a laterally and transversely vibrating 200x45x12 μm beam and a 400x45x12 μm beam with Young's moduli of 127.5 GPa as a function of percent aqueous glycerol in the operational medium.

In air, the increase in mass sensitivity is smaller as the ratio of the two effective masses is closer to one. In air, the predicted mass sensitivity increases for the beams given in Ref. 61 ranged from 3.11 to 6.25, and roughly followed the beam's *b/h* values.

In general, exciting beams laterally as opposed to transversely increased both the mass sensitivity and chemical sensitivity by a factor of *b/h* or greater. The increase was larger for media with higher viscosity and densities. Thus, lateral excitation is a better method of excitation compared to transverse excitation for sensing applications when operating in media of high viscosities and densities.

5. Summary, Conclusions, and Future Work

5.1 Summary

The primary objective of this work was to theoretically characterize and compare the characteristics of microcantilever-based (bio)chemical sensors vibrating in the in-plane and out-of-plane direction and note the improvement when the microcantilever is excited in the in-plane direction. Dynamically driven microcantilevers are commonly vibrated in the transverse or out-of-plane direction in both gas- and liquid-phase sensing applications. However, microcantilever (bio)chemical sensors vibrating in the transverse direction have a dramatic increase in their detection limit in liquid-phase sensing applications compared to gas-phase sensing applications due to the decrease in the device's resonant frequency, quality factor, and chemical sensitivity. It was expected that these characteristics would improve for beams vibrating in the in-plane or lateral direction due to the decreased viscous drag of the leading edge of the beam. Experimental results given in the literature have also shown that microcantilevers have higher resonant frequencies and quality factors when operating in the in-plane flexural mode as opposed to the out-of-plane flexural mode [10,61]. Modeling the characteristics of a laterally vibrating beam allowed for the trends in these characteristics to be investigated as functions of the properties of the medium and the beam's geometry. Using these trends, geometries that improve the characteristics of laterally vibrating microcantilever (bio)chemical sensors in the liquid-phase could be identified.

In order to successfully characterize laterally vibrating microcantilevers, standard Euler-Bernoulli beam theory was used to model the deflection of the beam as a function of the frequency of excitation. The deflection was found to also depend on the properties of the microcantilever and the hydrodynamic forces from the operational medium acting on the beam. The hydrodynamic forces were found as the sum of the pressure and shear forces. An analytical expression for the hydrodynamic forces acting on a laterally vibrating ribbon was previously derived by G. G. Stokes [105]. However, this solution neglected the effects of the pressure from the fluid on the thickness. The assumption was also made that the fluid shear was constant along the width of the beam, which neglected the significant variation in the fluid shear near the edge of the beam.

To account for the edge effects and the effect of thickness, a numerical model of the fluid surrounding a laterally vibrating beam was defined in the finite element analysis software ANSYS and used to evaluate the hydrodynamic forces acting on the beam. The hydrodynamic forces from the fluid shear and pressure on a laterally vibrating cross-section in water were found for various aspect ratios (the ratio of the beam’s thickness to the beam’s width) and Reynolds numbers (a measure of the ratio of the fluid’s inertial and viscous forces). The number of elements used in the model was varied to confirm that the solution for the hydrodynamic forces was convergent. The numerical results for the hydrodynamic function (a normalized version of the hydrodynamic force) were then compared to the results given by another model published in the literature [97]. The hydrodynamic function was then found for aspect ratios ranging from 1/56 to 1 and Reynolds numbers ranging from 10 to 10,000. A set of correction factors were obtained so that the hydrodynamic function found from Stokes’ solution could be mapped to the numerical results. These two correction factors were found as functions of the aspect ratio and the Reynolds number.

Using the same procedures found in Ref. 124, expressions for the resonant frequency, quality factor, and mass sensitivity of laterally vibrating beams were obtained. The trends in these characteristics were then investigated as functions of both the medium of operation (fluid density and dynamic viscosity) and the geometry of the microcantilever. These characteristics were also calculated using the values of the hydrodynamic function given by Ref. 97 and compared to the characteristics found using the hydrodynamic function obtained in this work.

The improvement obtained for each characteristic (resonant frequency, quality factor, and mass sensitivity) when using in-plane flexural modes compared to out-of-plane flexural modes was demonstrated. This was done by finding an expression for the ratio of the characteristics of a laterally vibrating beam to a transversely vibrating beam of the same geometry. This ratio was investigated as a function of the beam’s geometry and the medium of operation. This then demonstrated the benefits of using lateral excitation over the more common transverse excitation when operating in a viscous liquid medium.

5.2 Conclusions

The approach taken to find the semi-analytical expression for the hydrodynamic function involved the use of correction factors to map Stokes’ solution to exact numerical results. This technique is more appropriate for laterally vibrating beams compared to other methods given in the literature, which were primarily used to find the hydrodynamic forces of transversely vibrating beams. The number of terms used in the correction factors was small, thus yielding simple expressions while still providing a good approximation to the numerical results. The error introduced by the mapping also did not significantly change the predicted characteristics (resonant frequency, quality factor, and mass sensitivity) over the range of Reynolds numbers and aspect ratios investigated.

This semi-analytical expression is a significant benefit of this work, as it allowed for the rapid calculation of the hydrodynamic function over various ranges of aspect ratios and Reynolds numbers. Using the semi-analytical expression, it was found that the effects of the shear force acting on the width of the beam is significant and should be taken into account when modeling laterally vibrating beams operating in a viscous liquid medium. It was also found that the pressure forces from the viscous liquid medium acting on laterally vibrating beams for particular ranges of geometric parameters and Reynolds numbers contribute significantly to the total hydrodynamic force. For example, over the range of aspect ratios and Reynolds numbers investigated, the pressure force acting on the thickness contributed 10% or more of the total hydrodynamic force. It was noted that the significance of the shear forces and pressure forces on the total hydrodynamic force was also investigated by Brumley et al. [97] and similar results and conclusions were obtained. However, a larger range of Reynolds numbers was investigated in the present work. This may be important, as the Reynolds numbers of beams vibrating laterally compared to beams vibrating transversely are larger due to their increased resonant frequency.

Using the semi-analytical expression given in this work, the amount of displaced fluid mass is predicted, which compares well with recent results published in the literature [97]. Observed differences ranged from 5.88% (Re= 10, *h/b*=1/50) to -1.8% (Re= 31.62, *h/b*=1/5) and had an average absolute difference of 1.37%. However, the present method predicts a higher amount of viscous damping from the fluid. The difference ranged from 9.85% (Re= 10, *h/b*=1/50) more viscous damping to 2.8% (Re= 10, *h/b*=1) less viscous damping and had an average absolute difference of 3.8%. This difference could arise from errors in the hydrodynamic forces determined from the finite element analysis due to the selected mesh density dictating the convergence criteria of the computation. It is also possible that the results from the finite element analysis in this work more accurately represent the behavior of the fluid, as it accounts for the nonlinear convective effects of the fluid [127]. It was observed that the difference between the two methods is insignificant regarding the calculated resonant characteristics (frequencies, quality factors, and mass sensitivities) for practical cantilever geometries used in sensor applications over the range of aspect ratios and Reynolds numbers investigated. For example, the difference in the predicted characteristics from the two methods was found to be small (<4.1%) for beams that have quality factors high enough to be considered practical for sensor applications.

Analyzing these characteristics, it was found that the resonant frequency, quality factor, and mass sensitivity of dynamically driven microcantilevers were all predicted to increase for beams undergoing lateral excitation compared to those undergoing transverse excitation when operating in viscous liquid media. This indicated that operating dynamically driven microcantilevers in the in-plane flexural mode is better for liquid-phase (bio)chemical sensing applications, assuming that such devices may be effectively excited.

It was found that the ratio of the resonant frequencies of beams vibrating laterally compared to beams vibrating transversely increases by a factor proportional to the inverse of the beam's aspect ratio. This was due to the increased stiffness of the beam when operating in the in-plane flexural mode. This resonant frequency increase was predicted to be larger for media with higher densities and dynamic viscosities, which affect the effective mass more when operating in the out-of-plane flexural mode compared to when operating in the in-plane flexural mode. Increasing the density or dynamic viscosity of the medium still decreases the laterally vibrating beam's resonant frequency. However, this drop in resonant frequency for laterally vibrating beams (~10% when placed in water) was substantially smaller than the drop predicted for transversely vibrating beams (on the order of a ~50% drop when placed in water). This indicates that the resonant frequencies of beams operating in the in-plane flexural mode were both higher and less affected by the viscous damping from the medium of operation when compared to the resonant frequencies of similar beams operating in the out-of-plane flexural mode.

The resonant frequencies of laterally vibrating beams were also investigated as a function of the beam's geometry. The resonant frequency of a laterally vibrating microcantilever in air was found to be proportional to the width of the beam over the square of the length of the beam. This trend was found to also hold approximately for beams laterally vibrating in water. These trends also matched experimentally obtained trends published in the literature when a microcantilever was laterally vibrated both in air and in water. If beams with high resonant frequencies are desired for particular sensing applications, shorter and wider beams should be chosen.

The resonant frequency is expected to be approximately independent of the beam's thickness when operating in air. In water, it was predicted that the resonant frequency of a laterally vibrating beam has a slight dependence on the beam's thickness. For small beam thicknesses, the total effective mass (the sum of the beam mass and displaced fluid mass) was found to be approximately independent of the thickness, while the stiffness had a linear dependence on the thickness. Initially, when the beam's thickness was increased the resonant frequency was found to increase. This trend occurs when the beam's mass is less than the displaced mass of the fluid. Using the practical geometries in water studied in Ref. 61, the predicted displaced fluid mass only accounts for 11% to 35% of the total effective mass. When the beam's mass is greater than the displaced mass of the fluid, increasing the thickness increases the total effective mass more than the stiffness due to the additional viscous damping. This caused the resonant frequency to decrease as the thickness of the beam is increased. An optimal value for the beam thickness with respect to the resonant frequency could then be found if the operational medium and the beam's length and width were known.

The quality factor was also found to increase when beams were operating in the in-plane flexural mode compared to the out-of-plane flexural mode, with quality factors of laterally vibrating beams reaching values as high as 64 when operating in water. Unlike the trend found for the resonant frequency, the improvement when using the in-plane flexural mode was smaller when beams were operating in media with higher densities and dynamic viscosities. The predicted improvement for the practical geometries studied in Ref. 61 ranged from 3 to 4.5 in air and 1.55 to 2.53 in water. This improvement was also a function of the beam’s geometry. The improvement in the quality factors of laterally vibrating beams compared to transversely vibrating beams was found to be larger for shorter and wider beams. This was due to the shorter and wider beams having higher resonant frequencies and Reynolds numbers. As the Reynolds number increases, the ratio of the viscous damping seen by the transversely vibrating beam to the laterally vibrating beam increases.

Shorter and wider beams operating in the in-plane flexural mode also had higher quality factors compared to longer and narrower beams, since the quality factor of a laterally vibrating beam was found to be proportional to the square-root of the beam’s resonant frequency. This trend was predicted both in air and in water and was observed in experimental data published for laterally vibrating beams in water. (In air, additional effects, such as the support loss, need to be taken into account when comparing the theoretical results to those observed in the experimental data). The quality factor of a laterally vibrating beam in a viscous liquid medium was also found to be dependent on the beam’s thickness. For small beam thicknesses, this dependence was approximately linear. However, the quality factor’s linear dependency on the beam’s thickness does not hold for larger beam thicknesses (when the beam’s mass is greater than the displaced mass of the fluid) due to the additional viscous damping and effective fluid mass coming from the pressure acting on the thickness.

The quality factor was also found to be a function of the medium’s density. As the density of the medium increases, the quality factor decreases. The quality factor was found to have approximately the same dependence on the medium’s density as on the medium’s dynamic viscosity. Since the medium’s density increases more than its dynamic viscosity when a beam is placed in water from air, it can be noted that the quality factor drops more due to the increase in the medium’s density compared to the drop from the increase in the medium’s dynamic viscosity.

The ratio of the mass sensitivity of a laterally vibrating beam to that of a transversely vibrating beam of the same geometry, like the resonant frequency, was found to be proportional to the inverse of the aspect ratio. For small aspect ratios, operating in the in-plane flexural mode compared to operating in the out-of-plane flexural mode then increases the mass sensitivity more than it increases the quality factor. For the practical geometries studied in Ref. 61, the predicted improvement ranged from 7.3 to 35.8. For thinner beams, this improvement could be much larger. As with the resonant frequency, increasing the density and dynamic viscosity of the medium of operation will decrease the mass sensitivity. The mass sensitivity of beams operating in the in-plane flexural mode will decrease less than the mass sensitivity of beams operating in the out-of-plane flexural mode when the density and dynamic viscosity of the operational medium is increased. The ratio of these mass sensitivities was then higher for media with higher densities and dynamic viscosities. Assuming the same sensing layer is used, the ratio of the chemical sensitivity of a laterally vibrating beam to the chemical sensitivity of a transversely vibrating beam will be the same as the ratio of the mass sensitivities.

The mass sensitivity was found to be approximately proportional to the inverse of the beam’s thickness multiplied by the inverse of its length cubed. This means that the chemical sensitivity will be proportional to the resonant frequency of the beam when it is excited laterally. Shorter and wider beams vibrated laterally will thus have higher chemical sensitivities as well as higher quality factors and resonant frequencies. The chemical sensitivity was also found to be a function of the ratio of the sensing layer's thickness to the beam's thickness. There is then a trade-off between decreasing the chemical sensitivity of the device and increasing the quality factor of the device when increasing the thickness of the beam. Since the limit of detection is proportional to the inverse of the product of the quality factor and the chemical sensitivity, a thickness exists that optimizes the limit of detection for a particular beam length and width in a particular medium of operation. Regardless of the beam's thickness, the limit of detection of laterally vibrating beams in viscous liquid media is predicted to be much smaller than that of transversely vibrating beams of similar geometries, thus indicating in-plane excitation is a better excitation method compared to out-of-plane excitation when operating in viscous liquid media.

5.3 Future Work

The work done in this investigation can easily be expanded upon and improved. The sensing layer effects were not discussed in this investigation. The effects of different thicknesses of particular viscoelastic sensing layers on the characteristics of laterally vibrating beams can be incorporated into the model using the same method given in Ref. 124. The optimum thicknesses in terms of the limit of detection of particular sensing layers in viscous liquid media could then be calculated. The sensing layer's viscoelastic properties can change as a function of the amount of analyte sorbed. This will cause a change in the resonant frequency and change the chemical sensitivity of the device.

These effects can also be easily incorporated into the model if the properties of the sensing layer and its reaction to the analyte of interest are known.

It was shown that the beams with the highest resonant frequencies and quality factors were also the shortest beams. These short beams also have the largest rotational and shear inertia effects. These effects were not accounted for in this investigation. Modeling the beam using Timoshenko beam theory instead of Euler-Bernoulli beam theory would account for these effects. This would also allow optimal beam lengths and widths with respect to the limit of detection to be found.

The in-plane flexural mode is not the only other alternative mode of operation for dynamically driven microcantilevers. The torsional mode has also been investigated as a potential mode that would improve the characteristics of dynamically driven microcantilever (bio)chemical sensors over that of the out-of-plane flexural mode in liquid environments. While there have been many attempts at modeling this mode of operation [10,95-96], these models have not included the effects of the thickness. A numerical method similar to the one done in this work could be used to simulate the effects of thickness on the hydrodynamic loading of beams operating in the torsional mode. From the hydrodynamic loading and the beam’s properties, the resonant frequency, quality factor, and mass sensitivity could be found as functions of the medium of operation and the beam’s geometry. These characteristics could then be compared to those found for beams of similar geometries operating in both the in-plane and out-of-plane modes. One of the aspects of operating in the torsional mode that has been investigated previously is the dependence of the hydrodynamic function on the length of the beam [95]. Modeling this effect is not only important for short beams, but can also aid in the modeling of the hammerhead or T-shaped beams whose widths are not constant as a function of length.

Another parameter of interest when working with dynamically excited microcantilever (bio)chemical sensors is the optimum spacing of microcantilevers in arrays. The interaction of transversely vibrating arrays of infinitely thin microcantilevers in water has previously been modeled [50]. However, neither the interaction's dependence on the beam thickness or the interaction of arrays of laterally excited beams has been investigated in the literature. A numerical model of two cross-sections laterally vibrating could be defined and the change in the hydrodynamic loading as a function of the microcantilever's spacing, the Reynolds number, and the aspect ratio of both beams could be found.

Finally, the effects of thermal noise on the microcantilever should be modeled. Thermal noise causes random variations in the resonant frequency of dynamically driven microcantilever (bio)chemical sensors limiting the minimum detectable analyte concentration. The thermal noise itself might depend on the geometry of the beam and the medium of operation. Particular geometries or materials could then be chosen that limit the thermal noise. The thermal noise can also be positively utilized. One of the limits to the minimum size of dynamically driven microcantilevers is the minimum size of the transducer used to excite the beam into resonance. The thermal noise can cause the beam to undergo self-excitation. If the thermal noise is appropriately modeled, the random thermal fluctuations in the deflection can be used to track the resonant frequency of the beam without needing to drive the beam into resonance. While this method of excitation has been investigated in the literature for beams vibrating transversely [64, 65], no investigations have been published for lateral excitation, which, from the conclusions of this work, would be better suited for liquid-phase sensing applications.

REFERENCES

[1] Lange, D., Hagleitner, C., Hierlemann, A., Brand, O., and Baltes, H., "Complementary Metal Oxide Semiconductor Cantilever Arrays on a Single Chip: Mass-Sensitive Detection of Volatile Organic Compounds" *Analytical Chemistry*, vol. 74, pp. 3084-3095, 2002

[2] Paci, D., Kirstein, K. U., Vancura, C., Lichtenberg, J., and Baltes, H., "A Behavioural Model of Resonant Cantilever for Chemical Sensing" *Analog Integrated Circuits and Signal Processing*, vol. 44, pp. 119-128, 2005

[3] Vancura, C., Dufour, I., Heinrich, S. M., Josse, F., and Hierlemann, A., "Analysis of Resonating Microcantilevers Operating in a Viscous Liquid Environment" *Sensors and Actuators A*, vol. 141, pp. 43–51, 2008

[4] Bargatin, I., Myers, E. B., Arlett, J., Gudlewski, B., and Roukes, M. L., "Sensitive Detection of Nanomechanical Motion using Piezoresistive Signal Downmixing" *Applied Physics Letters*, vol. 86, no. 133109, pp. 1-3, 2005

[5] Fletcher, P. C., Xu, Y., Gopinath, P., Williams, J., Alphenaar, B. W., Bradshaw R. D., and Keynton, R. S., "Piezoresistive Geometry for Maximizing Microcantilever Array Sensitivity" *Proceedings of IEEE Sensors 2008*, pp. 1580-1583, 2008

[6] Fadel, L., Lochon, F., Dufour, I., and Francais, O., "Chemical Sensing: Millimeter Size Resonant Microcantilever Performance" *Journal of Micromechanics and Microengeneering*, vol. 14, pp. S23–S30, 2004

[7] Chatzandroulis, S., Tserepi, A., Goustouridis, D., Normand, P., and Tsoukalas, D., "Fabrication of Single Crystal Si Cantilevers using a Dry Release Process and Application in a Capacitive-Type Humidity Sensor" *Microelectronic Engineering*, vol. 61–62, pp. 995-961, 2002

[8] Gupta, A. , Denton, J. P., McNally, H., and Bashir, R., "Novel Fabrication Method for Surface Micromachined Thin Single-Crystal Silicon Cantilever Beams" *Journal of Microelectromechanical Systems*, vol. 12, no. 2, pp.1-7, 2003

[9] Hagleitner, C., Lange, D., Hierlemann, A., Brand, O., and Baltes, H., "CMOS Single-Chip Gas Detection System Comprising Capacitive, Calorimetric and

Mass-Sensitive Microsensors” *IEEE Journal of Solid-State Circuits*, vol. 37, no. 12, pp. 1867-1878, 2002

[10] Sharos, L. B., Raman, A., Crittenden, S., and Reifenberger, R., “Enhanced Mass Sensing using Torsional and Lateral Resonances in Microcantilevers” *Applied Physics Letters*, vol. 84, no. 23, pp. 4638-4640, 2004

[11] Spletzer, M., Raman, A., Sumali, H., and Sullivan, J. P., “Highly Sensitive Mass Detection and Identification Using Vibration Localization in Coupled Microcantilever Arrays” *Applied Physics Letters*, vol. 92, no. 114102, pp. 1-3, 2008

[12] Narducci, M., Figueras, E., Lopez, M. J., Gracia, I., Fonseca, L., and Santander, J., “A High Sensitivity Silicon Microcantilever Based Mass Sensor” *Proceedings of IEEE Sensors 2008*, pp. 1127-1130, 2008

[13] Yi, J. W., Shih, W. Y., and Shih, W. H., “Effect of Length, Width, and Mode on the Mass Detection Sensitivity of Piezoelectric Unimorph Cantilevers” *Journal of Applied Physics*, vol. 91, no. 3, pp. 1680-1686, 2002

[14] Davis, Zachary J., Abadal, G., Kuhn, O., Hansen, O., Grey, F., and Boisen, A., “Fabrication and Characterization of Nanoresonating Devices for Mass Detection” *Journal of Vacuum Science & Technology B*, vol. 18, no. 2, pp. 612-616, 2000

[15] Pinnaduwage, L. A., Boiadjiev, V., Hawk, J. E., and Thundat, T., “Sensitive Detection of Plastic Explosives with Self-Assembled Monolayer-coated Microcantilevers,” *Applied Physics Letters*, vol. 83, no. 7, p. 1471, 2003

[16] Pei, J., Tian, F. and Thundat, T., “Glucose Biosensor Based on the Microcantilever” *Analytical Chemistry*, vol. 76, no. 2, pp. 292-297, 2004

[17] Calleja, M., Tamayo, J., Johansson, A., Rasmussen, P., Lechuga, L., and Boisena, A., “Polymeric Cantilever Arrays for Biosensing Applications,” *Sensor Letters*, vol. 1, no. 1–5, 2003

[18] Wenzel, M., *Polymer-Coated and Polymer-Based Microcantilever Chemical Sensors: Analysis and Sensor Signal Processing*, Ph.D. Dissertation, August 2009, Marquette University, WI, USA

[19] Vancura, C., Li, Y., Lichtenberg, J., Kirstein, K.-U, Hierlemann, A., and Josse, F., “Liquid-Phase Chemical and Biochemical Detection Using Fully Integrated Magnetically Actuated Complementary Metal Oxide Semiconductor Resonant Cantilever Sensor Systems” *Analytical Chemistry*, vol. 79, no. 4, pp. 1646-1654, January 2007

[20] Boisen, A., Thaysen, J., Jensenius, H. and Hansen, O., “Environmental Sensors Based on Micromachined Cantilevers with Integrated Read-Out” *Ultramicroscopy*, vol. 82, pp. 11-16, 2000

[21] Rogers, B., Manning, L., Jones, M., Sulchek, T., Murray, K., Beneschott, B., Adams, J.D., Hu, Z., Thundat, T., Cavazos, H., and Minne, S.C., “Mercury Vapor Detection with a Self-Sensing, Resonating Piezoelectric Cantilever” *Review of Scientific Instruments*, vol. 74, no. 11, pp. 4899-4901, 2003

[22] Thundat, T., Wachter, E. A., Sharp, S. L. and Warmack, S. J., “Detection of Mercury Vapor using Resonating Microcantilevers” *Applied Physics Letters*, vol. 66, iss. 13, pp. 1695-1697, 1995

[23] Sepaniak, M., Datskos, P., Lavrik, N., and Tipple, C., “Microcantilever Transducers: A new Approach in Sensor Technology” *Analytical Chemistry*, vol. 74, no. 21, pp. 568-575, 2002

[24] Chon, J., Mulvaney, P., and Sader, J., “Experimental Validation of Theoretical Models for the Frequency Response of Atomic Force Microscope Cantilever Beams Immersed in Fluids” *Journal of Applied Physics*, vol. 87, no. 8, pp. 3978-3988, April 2000

[25] Kadam, A. R., Nordin, G. P., and George, M. A., “Use of Thermally Induced Higher Order Modes of a Microcantilever for Mercury Vapor Detection” *Journal of Applied Physics*, vol. 99, no. 094905, pp. 1-4, 2006

[26] Lochon, F., Fadel, L., Dufour, I., Rebiere, D., and Pistre, J., “Silicon Made Resonant Microcantilever: Dependence of the Chemical Sensing Performances on the Sensitive Coating Thickness” *Materials Science and Engineering C*, vol. 26, pp. 348-353, 2006

[27] Pinnaduwage, L. A., Ji, H.-F., and Thundat, T., “Moore’s Law in Homeland Defense: An Integrated Sensor Platform Based on Silicon Microcantilevers” *IEEE Sensors Journal*, vol. 5, no. 4, pp. 774-785, August 2005

[28] Porter, T. L., Delinger, W., Gunter, R. L., “Embedded Piezoresistive Microcantilever Sensors: Materials for Sensing Chemical and Biological Analytes” *Material Research Society Symposium Proceedings*, vol. 872, pp. 265-270, 2005

[29] Keskar, G., Elliott, B., Skove, M. J., Gaillard, J., Serkiz, S. M., and Rao, A. M., “Active Sensing in Ambient Conditions Using an Electrostatically Driven Silicon Microcantilever” *Sensors & Transducers Journal*, vol. 91, iss. 4, pp. 1-13, April 2008

[30] Li, S., Orona, L., Li, Z., and Chenga, Z.-Y., “Biosensor Based on Magnetostrictive Microcantilever” *Applied Physics Letters*, vol. 88, no. 073507, pp 1-3, 2006

[31] Lavrik, N. V., Sepaniak, M. J., and Datskos, P. G., “Cantilever Transducers as a Platform for Chemical and Biological Sensors” *Review of Scientific Instruments*, vol. 75, no. 7, pp. 2229-2253, July 2004

[32] Ocakli, H. I., Ozturk, A., Ozber, N., Kavakli, H., Alaca, E., and Urey, H., “Resonant Cantilever Bio Sensor with Integrated Grating Readout” *2008 IEEE/LEOS International Conference on Optical MEMs and Nanophotonics*, pp. 46-47, 2008

[33] Karhade, O. G., Chiluveru, S. S., and Apte, P. R., “Novel Cantilever for Biosensing Applications” *IEEE/SEMI Advanced Semiconductor Manufacturing Conference*, pp 409-412, 2004

[34] Fu, L., Li, S., Zhang, K., Cheng, Z-Y., and Barbaree, J. M., “Detection of Bacillus Anthracis Spores in Water Using Biosensors Based on Magnetostrictive Microcantilever Coated with Phage” *Proceedings of the SPIE - The International Society for Optical Engineering*, vol. 6556, no. 1, pp. 655619-1-9, 2007

[35] Boisen, A., and Thundat, T., “Design & Fabrication of Cantilever Array Biosensors” *Materials Today*, vol. 12, no. 9, pp. 32-38, 2009

[36] Ji, Hai-Feng, and Thundat, Thomas, “In Situ Detection of Calcium Ions with Chemically Modified Microcantilevers” *Biosensors & Bioelectronics*, vol. 17, pp. 337–343, 2002

[37] Ilic, B., Czaplewski, D., Craighead, H. G., Neuzil, P., Campagnolo, C. and Batt, C., “Mechanical Resonant Immunospecific Biological Detector” *Applied Physics Letters*, vol. 77, no. 3, pp. 450-452, 2000

[38] Rudnitsky, R. G., Chow, E. M., and Kenny, T. W., “Rapid Biochemical Detection and Differentiation with Magnetic Force Microscope Cantilever Arrays” *Sensors and Actuators A*, vol. 83, pp. 256–262, 2000

[39] Loui, A., Goericke, F. T., Ratto, T. V., Lee, J., Hart, B. R., and King, W. P., “The Effect of Piezoresistive Microcantilever Geometry on Cantilever Sensitivity During Surface Stress Chemical Sensing” *Sensors and Actuators A*, vol. 147, no. 2, pp. 516-521, 2008

[40] Tetin, S., Caillard, B., Menil, F., Debeda, H., Lucat, C., Pellet, C., and Dufour, I., “Chemical Sensing using Microcantilever without Sensitive Coating” *Joint*

Meeting of the European Frequency and Time Forum (EFTF'09) and the IEEE International Frequency Control Symposium (FCS'09), pp. 818-821, 2009

[41] Lang, H. P., Berger, R., Battiston, F., Ramseyer, J.-P., Meyer, E., Andreoli, C., Brugger, J., Vettiger, P., Despont, M., Mezzacasa, T., Scandella, L. Güntherodt, H.-J., Gerber, Ch., and Gimzewski, J. K., "A Chemical Sensor Based on a Micromechanical Cantilever Array for the Identification of Gases and Vapors" *Applied Physics A*, vol. 66, pp. S61–S64, 1998

[42] Wachter, E. A., and Thundat T., "Micromechanical Sensors for Chemical and Physical Measurements" *Review of Scientific Instruments*, vol. 66, no. 6, pp. 3662-3668, 1995

[43] Dufour, I., and Fadel, L., "Resonant Microcantilever Type Chemical Sensors : Analytical Modeling in View of Optimization" *Sensors and Actuators B*, vol. 91, pp. 353–361, 2003

[44] Ji, H.-F., Thundat, T., Dabestani, R., Brown, G. M., Britt, P. F., and Bonnesen, P. V., "Ultrasensitive Detection of CrO4 2- Using a Microcantilever Sensor" *Analytical Chemistry*, vol. 73, pp. 1572-1576, 2001

[45] Cox, R., Josse, F., Wenzel, M. J., Heinrich, S. M., and Dufour, I., "Generalized Model of Resonant Polymer-Coated Microcantilevers in Viscous Liquid Media" *Analytical Chemistry*, vol. 80, no. 15, pp. 5760-5767, 2008

[46] Sampath, U., Heinrich, S. M., Josse, F., Lochon, F., Dufour, I. and Rebiere, D., "Study of Viscoelastic Effect on the Frequency Shift of Microcantilever Chemical Sensors" *IEEE Transactions on Ultrasonics, Ferroelectrics, and Frequency Control*, vol. 53, no. 11, 2006

[47] Ghatkesar, M., Barwich, V., Braun, T. Bredekamp, A., Drechsler, U., Despont, M., Lang, H., Hegner, M. and Gerber Ch., "Real-Time Mass Sensing by Nanomechanical Resonators in Fluid", *Proceedings of IEEE Sensors 2004*, October, 2004

[48] Datskos, P. G., Thundat, T., Lavrik, and Nickolay V., "Micro and Nanocantilever Sensors" *Encyclopedia of Nanoscience and Nanotechnology*, vol. 10, pp. 1–10, 2004

[49] Duda, R. O., Hart, P. E. and Stork, D. G., *Pattern Classification*, Wiley, New York, 2001

[50] Basak, S. and Raman, A., "Hydrodynamic Coupling Between Micromechanical Beams Oscillating in Viscous Fluids" *Physics of Fluids*, vol. 19, no. 017105, pp. 1-13, 2007

[51] Chaudhary, M., and Gupta, A., “Microcantilever-Based Sensors” *Defence Science Journal*, vol.59, no.6, pp. 634-641, 2009

[52] Eggins, B., *Chemical Sensors and Biosensors*, NJ, USA: John Wiley & Sons, LTD, pp.98-111, 2002

[53] Zhonghui, L., *Guided Shear-Horizontal Surface Acoustic Wave (SH-SAW) Chemical Sensors for Detection of Organic Contaminants in Aqueous Environments*, Ph.D. Dissertation, December 2004, Marquette University, WI, USA

[54] Zhao, Y.-P., Fortin, J. B., Bonvallet, G., Wang, G.-C., and Lu, T.-M., “Kinetic Roughening in Polymer Film Growth by Vapor Deposition” *Physical Review Letters*, vol. 85, no. 15, pp. 3229-3233, October 2000

[55] Oliviero, G., Bergese, P., Canavese, G., Chiari, M., Colombi, P., Cretich, M., Damin, F., Fiorilli, S., Marasso, S. L., Ricciardi, C., Rivolo, P., and Depero, L. E., “A Biofunctional Polymeric Coating for Microcantilever Molecular Recognition”, *Analytica Chimica Acta*, vol. 630, pp. 161–167, 2008

[56] Nielsen, T. B., and Hansen, C. M., “Significance of Surface Resistance in Absorption by Polymers”, *Industrial and Engineering Chemical Research*, vol. 44 no. 11, p. 3959, 2005

[57] Timoshenko, S. P., “Analysis of Bi-Metal Thermostats” *Journal of the Optical Society of America,* vol. 11, iss. 3, pp. 233-255, 1925

[58] Heinrich, S. M., Wenzel, M. J., Josse, F., and Dufour, I., “An Analytical Model for Transient Deformation of Viscoelastically Coated Beams: Applications to Static-Mode Microcantilever Chemical Sensors,” *Journal of Applied Physics*, vol. 105, no. 124903, pp. 1-36, 2009

[59] Lobontiu, N., and Garcia, E., *Mechanics of Microelectromechanical Systems*, Kluwer Academic Publishers: New York, pp. 16-17, 66-114, and 182-262, 2005

[60] Bargatin, I., Kozinsky, I., and Roukes, M. L., “Efficient Electrothermal Actuation of Multiple Modes of High-Frequency Nanoelectromechanical Resonators” *Applied Physics Letters*, vol. 90, no. 093116, pp. 1-3, 2007

[61] Beardslee, L., Addous, A. M., Heinrich, S. M., Josse, F., Dufour, I., and Brand, O., “Thermal Excitation and Piezoresistive Detection of Cantilever In-Plane Resonance Modes for Sensing Applications,” *Journal of Microelectromechanical Systems*, vol. 19, no. 4, pp. 1015-1017, 2010

[62] Dufour, I., and Sarraute, E., “Analytical Modeling of Beam Behaviour Under Different Actuations: Profiles and Stress Expressions” *Journal of Modeling and Simulating of Microsystems*, vol. 1, no. 1, pp. 57-64, 1999

[63] Bianco, S., Cocuzza, M., Ferrante, I., Giuri, E., Pirri, C. F., Scaltrito, L., Bich, D., Merialdo, A., Schina, P., and Correale, R., “Silicon Microcantilevers with Different Actuation-Readout Schemes for Absolute Pressure Measurement” *Journal of Physics: Conference Series*, vol. 100, no. 092008, pp. 1-4, 2008

[64] Ramos, D., Mertens, J., Calleja, M., and Tamayo, J., “Phototermal Self-Excitation of Nanomechanical Resonators in Liquids” *Applied Physics Letters,* vol. 92, no. 173108, pp. 1-3, 2008

[65] Passian, A., Lereu, A. L., Yi, D., Barhen, S., and Thundat, T., “Stochastic Excitation and Delayed Oscillation of a Micro-oscillator” *Physical Review B,* vol. 75, no. 233403, pp. 1-4, 2007

[66] Calleja, M., Rasmussen, P., Johansson, A., and Boisen, A., “Polymeric Mechanical Sensors with Integrated Readout in a Microfluidic System” *Smart Sensors, Actuators, and MEMS. Conference,* vol. 5116, no. 1, pp. 314-321, 2003

[67] Jensenius, H., Thaysen, J., Rasmussen, A. A., Veje, L. H., Hansen, O., and Boisen, A., “A Microcantilever-based Alcohol Vapor Sensor-Application and Response Model” *Applied Physics Letters*, vol. 76, no. 18, pp. 2615-2617, 2000

[68] Vancura, C., Kirstein, K.-U., Li, Y., Josse, F., and Hierlemann, A., “Equivalent-Circuit Model for CMOS-Based Resonant Cantilever Biosensors” *Transducers '07, Digest of Technical Papers*, pp.1733-1736, 2007

[69] Cox, R., Wenzel, M. J., Josse, F., Heinrich, S. M., and Dufour, I., “Generalized Characteristics of Resonant Polymer-Coated Microcantilevers in Viscous Liquid Media” *Proceeding of the 2007 IEEE International Frequency Control Symposium,* pp.420-425, 2007

[70] Boskovic, S., Chon, J. W. M., Mulvaney, P., and Sader, J. E., “Rheological Measurements using Microcantilevers” *Journal of Rheology*, vol. 46, no. 4, pp. 891-899, 2002

[71] Oden, P. I., Chen, G. Y., Steele, R. A., Warmack, R. J., and Thundat, T., “Viscous Drag Measurements Utilizing Microfabricated Cantilevers” *Applied Physics Letters*, vol. 68, no. 26, pp. 3814-3816, 1996

[72] Shih, W. Y., Li, X., Gu, H., Shih, W.-H., and Aksay, I. A., “Simultaneous Liquid Viscosity and Density Determination with Piezoelectric Unimorph Cantilevers” *Journal of Applied Physics,* vol. 89, no. 2, 2001

[73] Giessibl, F. J., “Advances in Atomic Force Microscopy” *Reviews of Modern Physics*, vol. 75, pp. 949-983, 2003

[74] Thundat, T., Warmack, R. J., Chen, G. Y., and Allison, D. P., “Thermal and Ambient Induced Deflections of Scanning Force Microscope Cantilevers” *Applied Physics Letters*, vol. 64, pp. 2894-2896, 1994

[75] Kapa, P., Liu, P., Bandhanadham, A., Ji, F., Varahramyan, K., Davis W., and Ji, H.-F., “Moisture Measurement Using Porous Aluminum Oxide Coated Microcantilevers” *Sensors and Actuators B*, vol. 134, no. 2, pp. 390-395, 2008

[76] Baselt, D. R., Fruhberger, B., Klaasen, E., Cemalovic, S., Britton Jr., C. L., Patel, S. V., Mlsna, T. E., McCorkle, D. and Warmack, B., “Design and Performance of a Microcantilever Based Hydrogen Sensor” *Sensors and Actuators B*, vol. 88, no. 2, pp. 120-131, 2003

[77] Goeders, K., Colton, J., and, Bottomley, L., “Microcantilevers: Sensing Chemical Interactions via Mechanical Motion” *Chemical Reviews*, vol. 108, no. 2, pp. 522-542, 2008

[78] Vancura, C., Ruegg, M., Li, Y., Lange, D., Hagleitner, C., Brand, O., Hierlemann, A., and Baltes, H., “Magnetically Actuated CMOS Resonant Cantilever Gas Sensor for Volatile Organic Compounds” *Transducers '03, 12th International Conference on Solid-State Sensors, Actuators and Microsystems*, vol. 2, pp. 1355-1358, 2003

[79] Neste, C. W. Van, Senesac, L. R., Yi, D., and Thundat, T., “Standoff Detection of Explosive Residues Using Photothermal Microcantilevers” *Applied Physics Letters*, vol. 92, no. 134102, pp. 1-3, 2008

[80] Plata, M. R., Hernando, J., Zougagh, M., Contento, A. M., Villasenor, M. J., Sanchez-Rojas, J. L., and Rios, A., “Characterization and Analytical Validation of a Microcantilever-Based Sensor for the Determination of Total Carbonate in Soil Samples” *Sensors and Actuators B*, vol. 134, no. 1, pp. 245-51, 2008

[81] Pinnaduwage, L. A., Zhao, W., Gehl, A. C., Allman, S. L., Shepp, A., Mahmud, K. K., and Leis, J. W., “Quantitative Analysis of Ternary Vapor Mixtures Using a Microcantilever-based Electronic Nose” *Applied Physics Letters*, vol. 91, no. 044105, pp. 1-3, 2007

[82] Tamayo, J., Humphris, A. D. L., Malloy, A. M. and Miles, M. J., “Chemical Sensors and Biosensors in Liquid Environment Based on Microcantilevers with Amplified Quality Factor” *Ultramicroscopy*, vol. 86, pp. 167-173, 2001

[83] Ghatkesar, M. K., Rakhmatullina, E., Lang, H-P., Gerber, C., Hegner, M., and Braun, T., “Multi-parameter Microcantilever Sensor for Comprehensive Characterization of Newtonian Fluids” *Sensors and Actuators B*, vol. 135, no. 1, pp. 133-138, 2008

[84] Dufour, I., Heinrich, S., and Josse, F., “Theoretical Analysis of Strong-Axis Bending Mode Vibrations for Resonant Microcantilever (Bio)Chemical Sensors in Gas or Liquid Phase” *Journal of Microelectromechanical Systems*, vol.16, iss.1, pp. 44-49, Feb. 2007

[85] Sader, J., “Frequency Response of Cantilever Beams Immersed in Viscous Fluids with Applications to the Atomic Force Microscope” *Journal of Applied Physics*, vol. 84, no. 1, pp. 64-76, July 1998

[86] Basak, S., and Raman, A., “Hydrodynamic Loading of Microcantilevers Vibrating in Viscous Fluids” *Journal of Applied Physics*, vol. 99, no. 114906, pp. 1-10, 2006

[87] Razavi, B., “A Study of Phase Noise in CMOS Oscillators” *IEEE Journal of Solid-State Circuits*, vol. 31, no. 3, pp. 331-343, 1996

[88] Sekaric, L., Zalalutdinov, M., Bhiladvala, R. B., Zehnder, A. T., Parpia, J. M., and Craighead, H. G., “Operation of Nanomechanical Resonant Structures in Air” *Applied Physics Letters*, vol. 81, iss. 14, pp. 2641-2643, September 2002

[89] Lochon, F., Dufour, I., Rebière, D., Sampath, U., Heinrich, S.M., and Josse, F., “Effect of Viscoelasticity on Quality Factor of Microcantilever Chemical Sensors: Optimal Coating Thickness for Minimum Limit of Detection” *Proceedings of IEEE Sensors 2005*, pp. 265-268, 2005

[90] Eysden, C. A. Van, and Sader, J. E., “Frequency Response of Cantilever Beams Immersed in Viscous Fluids with Applications to the Atomic Force Microscope: Arbitrary Mode Order” *Journal of Applied Physics*, vol. 101, no. 044908, 2007

[91] Xia, X., Zhou, P., and Li, X., “Effect of Resonance-mode Order on Mass-sensing Resolution of Microcantilever Sensors” *Proceedings of IEEE Sensors 2008*, pp. 577-580, 2008

[92] Lochon, F., Dufour, I., and Rebiere, D., “An Alternative Solution to Improve Sensitivity of Resonant Microcantilever Chemical Sensors: Comparison Between Using High-Order Modes and Reducing Dimensions” *Sensors and Actuators B*, vol. 108, no. 1-2, p. 979–985, July 2005

[93] Hao, Z., Erbil, A., and Ayazi, F., “An Analytical Model for Support Loss in Micromachined Beam Resonators with In-plane Flexural Vibrations” *Sensors and Actuators A*, vol. 109, pp. 156–164, 2003

[94] Naeli, K. and Brand, O., “Dimensional Considerations in Achieving Large Quality Factors for Resonant Silicon Cantilevers in Air,” *Journal of Applied Physics* vol. 105, no. 014908, pp. 1-10, 2009

[95] Green, C. P., and Sader, J. E., “Torsional Frequency Response of Cantilever Beams Immersed in Viscous Fluids with Applications to the Atomic Force Microscope” *Journal of Applied Physics*, vol. 92, no. 10, 2002

[96] Xie, H., Vitard, J., Haliyo, S., and Régnier, S., “Enhanced Sensitivity of Mass Detection Using the First Torsional Mode of Microcantilevers” *Proceedings of the 2007 IEEE International Conference on Mechatronics and Automation,* pp. 39-44, 2007

[97] Brumley, D., Willcox, M., and Sader, J., “Oscillation of Cylinders of Rectangular Cross section Immersed in Fluid” *Physics of Fluids*, vol. 22, no. 052001, 2010

[98] Heinrich, S. M., Maharjan, R., Beardslee, L. Brand, O., Dufour, I., and Josse, F. “An analytical model for in-plane flexural vibrations of thin cantilever-based sensors in viscous fluids: applications to chemical sensing in liquids,” *Proceedings*, *International Workshop on Nanomechanical Cantilever Sensors*, Banff, Canada, pp. 2, 2010

[99] Heinrich, S. M., Maharjan, R., Dufour, I. Josse, F., Beardslee, L. and Brand, O. “An analytical model of a thermally excited microcantilever vibrating laterally in a viscous fluid,” *Proceedings IEEE Sensors 2010 Conference*, Waikoloa, Hawaii, pp. 1399-1404., 2010

[100] Kanwal, R. P., “Vibration of an Elliptic Cylinder and Flat Plate in a Viscous Fluid” *Journal of Applied Mathematics and Mechanics,* vol. 35, iss. 1-2, pp. 17–22, 1955

[101] Crabtree, L. F., Gadd, G. E., Gregory, N., Illingworth, C. R., Jones, C. W., Kuchemann, D., Lighthill, M. J., Pankhurst, R. C., Rosenhead, L., Sowerby, L., Stuart, J. T., Watson, E. J., Whitham, G. B., *Laminar Boundary Layers*, Clarendon Press: Oxford, p. 27, 1963

[102] Tuck, E., “Calculation of Unsteady Flows due to Small Motions of Cylinders in a Viscous Fluid” *Journal of Engineering Mathematics*, vol. 3, no. 1, pp. 29-44, 1969

[103] Bhiladvala, R. B. and Wang, Z. J., "Effect of Fluids on the Q Factor and Resonance Frequency of Oscillating Micrometer and Nanometer Scale Beams" *Physical Review E*, vol. 69, no. 036307, pp. 1-5, 2004

[104] Rosenhead, L., ed. *Laminar Boundary Layers*. Oxford: Clarendon press, 1963

[105] Stokes, G., "On the Effects of the Internal Friction of Fluids on the Motion of Pendulums" *Transactions of the Cambridge Philosophical Society*, vol. 9, pp 8-106, 1851

[106] Hu, S. P., "Method of Fundamental Solutions for Stokes' First and Second Problems", *Journal of Mechanics*, vol. 21, no. 1, pp. 25-31, 2005

[107] Zhang, W., Requa, M., and Turner, K., "Determination of Frequency Dependent Fluid Damping of Micro and Nano Resonators for Different Cross-Sections" *Sensors and Actuators A*, vol. 134, iss. 2, pp. 594-599, 2007

[108] Tomotika, S., and Aoi, T., "The Steady Flow of a Viscous Fluid past an Elliptic Cylinder and a Flat Plate at Small Reynolds Numbers" *The Quarterly Journal Of Mechanics and Applied Mathematics*, vol. 6, iss. 3, pp. 290-312, 1953

[109] Iyengar, T., Srinivasacharyulu, N., and Ramana, J. "Drag on an Elliptic Cylinder in a Fluid Particle Suspension" *Journal of Applied Mathematics and Physics*, vol. 39, pp. 649-667, 1988

[110] Lamb, H., *Hydrodynamics* Dover Publications: New York, 6th edition, p. 609, 1945

[111] Westervelt, P. J., "Hydrodynamic Flow and Oseen's Approximation" *The Journal of the Acoustical Society of America*, vol. 25, no. 5, pp. 951-953, 1953

[112] Dufour, I. and Fadel, L., "Resonant Microcantilever Type Chemical Sensors: Analytical Modeling in View of Optimization" *Sensors and Actuators B*, vol. 91, pp. 353–361, 2003

[113] Chuang, W.-H., Luger, T., Fettig, R., and Ghodssi, R. "Mechanical Property Characterization of LPCVD Silicon Nitride Thin Films at Cryogenic Temperatures" *Journal of Microelectromechanical Systems*, vol. 13, no. 5, pp. 870-879, October 2004

[114] Lopez, A, Yong, D. J., Serna, M. A., "Lateral-Torsional Buckling of Steel Beams: A General Expression for the Moment Gradient Factor", *Stability and Ductility of Steel Structures*, Lisbon, Portugal, September 6-8, 2006

[115] Hosaka, H., Itao, K., and Kuroda, S., "Damping Characteristics of Beam-shaped Micro-oscillators" *Sensors and Actuators A*, vol. 49, pp. 87-95, 1995

[116] Maali, A., Hurth, C., Boisgard, R., Jai, C., Cohen-Bouhacina, T., and Aimé, J. "Hydrodynamics of Oscillating Atomic Force Microscopy Cantilevers in Viscous Fluids" *Journal of Applied Physics*, vol. 97, no. 074907, pp. 1-6, 2005

[117] Wylie, C. Ray, Barrett, Louis C., *Advanced Engineering Mathematics*, 6th edition, New York: McGraw-Hill, Inc, pp. 783-913, 1995

[118] Jones, D. I. G., *Handbook of Viscoelastic Vibration Damping*, Chichester: John Wiley & Sons Ltd., p. 266, 2001.

[119] Hopcroft, M. A., Nix, W. D., and Kenny, T. W., "What is the Young's Modulus of Silicon?" *Journal of Microelectromechanical Systems*, vol.19, no. 2, pp. 229-238, 2010

[120] Matthews, G., *Investigation of Flexural Plate Wave Devices for Sensing Applications in Liquid Media*, Ph.D. Dissertation, August 2007, Royal Melbourne Institute of Technology University, Melbourne, Australia

[121] Turner, M. J., Clough, R.W., Martin, H. C. and Topp, L. J., "Stiffness and Deflection Analysis of Complex Structures," *Journal of the Aeronautical Sciences*, vol. 23, no. 9, Sept. 1956.

[122] Rao, S. S., *The Finite Element Method In Engineering*, 4th ed. Burlington, MA: Elsevier Inc, 2005.

[123] Weast, C. R., ed., *Standard Mathematical Tables*, Ohio, 17th edition, p. 213, 1969

[124] Cox, R., *Theoretical Analysis of Dynamically Operating Polymer-Coated Microcantilever Chemical Sensors in a Viscous Liquid Medium*, Masters Thesis, August 2007, Marquette University, WI, USA

[125] Weast, C. R., ed., *Handbook of Chemistry and Physics*, Ohio, 54th edition, 1973

[126] Weast, C. R., ed., *Handbook of Chemistry and Physics*, Ohio, 65th edition, 1984

[127] ANSYS Inc., *Theory Reference for the Mechanical APDL and Mechanical Applications*, Version 12.0, section 7.1.2, 2009

APPENDIX A: NUMERICAL RESULTS FROM ANSYS

	log(h/b)=0	0.25	0.5	0.75	1	1.25	1.5	1.75
log(Re)=1	4.62e-4	2.59 e-4	1.77e-4	1.39 e-4	1.18 e-4	1.1 e-4	1.05 e-4	1.01 e-4
1.25	1.261e-3	6.61 e-4	4.24 e-4	3.21 e-4	2.67 e-4	2.46 e-4	2.32 e-4	2.24 e-4
1.5	3.54 e-3	1.734e-3	1.041 e-3	7.53 e-4	6.12 e-4	5.57 e-4	5.22 e-4	5.02 e-4
1.75	0.010179	4.683 e-3	2.621 e-3	1.799 e-3	1.421 e-3	1.274 e-3	1.184 e-3	1.134 e-3
2	0.029867	0.013004	0.006775	0.004379	0.003341	0.002939	0.002709	0.002582
2.25	0.089009	0.037028	0.018001	0.010876	0.007956	0.006838	0.00624	0.005918
2.5	0.268561	0.107789	0.049147	0.027616	0.019197	0.016046	0.014457	0.013638
2.75	0.821627	0.318097	0.13771	0.071825	0.047039	0.03794	0.033662	0.031554
3	2.532252	0.955205	0.393836	0.191633	0.117155	0.090508	0.078787	0.073227
3.25	7.864478	2.907386	1.139516	0.524508	0.297407	0.217925	0.18516	0.170301
3.5	24.53087	8.953956	3.398823	1.453204	0.771819	0.530605	0.436847	0.396544
3.75	76.73886	27.75059	10.3261	4.143764	2.042715	1.308498	1.034591	0.923467
4	239.8214	86.20338	31.60972	12.15687	5.51711	3.269185	2.458668	2.147008

Table A-1. Magnitude of hydrodynamic force in Newtons on top and right hand side of laterally vibrating cross-section in water (*b*=20 μm, *h*=2 μm) as a function of Reynolds number and aspect ratio (*h/b*)

	log(h/b)=0	0.25	0.5	0.75	1	1.25	1.5	1.75
log(Re)=1	-63.76330	-53.50664	-44.26542	-38.38273	-35.12395	-33.20753	-32.22597	-31.11153
1.25	-68.15430	-57.90142	-48.16814	-41.36597	-37.53344	-34.82186	-33.69106	-33.11546
1.5	-72.12286	-62.43517	-52.20018	-44.46925	-39.54898	-36.89584	-35.65673	-35.02011
1.75	-75.54705	-66.75285	-56.31586	-47.38066	-41.97502	-38.88040	-37.42441	-36.74974
2	-78.51016	-70.67383	-60.35054	-50.74748	-44.41889	-40.72260	-39.02426	-38.23815
2.25	-80.92598	-74.25600	-64.41381	-54.08272	-46.62607	-42.10859	-40.05742	-39.11227
2.5	-82.90587	-77.36046	-68.41135	-57.65227	-49.00218	-43.55865	-40.97702	-39.84097
2.75	-84.51849	-79.94275	-72.10805	-61.39611	-51.63494	-45.02736	-41.79886	-40.40481
3	-85.78797	-82.11191	-75.37234	-65.22664	-54.53457	-46.65440	-42.62046	-40.83073
3.25	-86.78245	-83.87635	-78.15498	-69.00095	-57.73629	-48.48177	-43.42677	-41.12138
3.5	-87.55144	-85.29849	-80.67153	-72.30376	-61.15305	-50.51009	-44.14355	-41.14128
3.75	-88.14273	-86.41880	-82.81018	-75.52771	-64.71762	-53.01765	-45.13836	-41.25305
4	-88.57708	-87.27893	-84.51174	-78.50240	-68.22110	-55.78456	-46.21060	-41.13328

Table A-2. Phase offset in degrees between hydrodynamic force and velocity on top and right hand side of laterally vibrating cross-section in water as a function of Reynolds number and aspect ratio (*h/b*)

	log(h/b)=0	0.25	0.5	0.75	1	1.25	1.5	1.75
log(Re)=1	2.637865	1.327356	0.786240	0.549178	0.431921	0.384095	0.354825	0.332673
1.25	2.357109	1.126900	0.636330	0.426597	0.327220	0.283353	0.259489	0.246473
1.5	2.144983	0.978523	0.523850	0.335850	0.248093	0.213075	0.193835	0.183339
1.75	1.984367	0.866288	0.439110	0.266567	0.191286	0.161019	0.144911	0.136588
2	1.863290	0.781189	0.374859	0.215897	0.148863	0.122084	0.108596	0.101731
2.25	1.769470	0.717477	0.326858	0.177325	0.116424	0.092301	0.080849	0.075163
2.5	1.696626	0.669580	0.290929	0.148524	0.092239	0.070395	0.060354	0.055625
2.75	1.646512	0.630543	0.263827	0.126948	0.074250	0.054035	0.045168	0.041175
3	1.607729	0.602349	0.242597	0.110771	0.060745	0.041902	0.033964	0.030480
3.25	1.580757	0.581966	0.224519	0.098580	0.050629	0.032849	0.025624	0.022547
3.5	1.560259	0.568109	0.213514	0.088136	0.043038	0.026069	0.019369	0.016609
3.75	1.544072	0.557576	0.206247	0.080774	0.037184	0.021043	0.014763	0.012259
4	1.526281	0.548169	0.200311	0.075840	0.032616	0.017210	0.011299	0.008991

Table A-3. The real part of the hydrodynamic function of a laterally vibrating beam found as a function of Reynolds number and aspect ratio (*h/b*)

	log(h/b)=0	0.25	0.5	0.75	1	1.25	1.5	1.75
log(Re)=1	1.300093	0.9819549	0.806664	0.693320	0.614016	0.586791	0.562887	0.551228
1.25	0.944961	0.7068655	0.569582	0.484459	0.425927	0.407360	0.389220	0.377866
1.5	0.691868	0.5107961	0.406338	0.342131	0.300438	0.283833	0.270180	0.261640
1.75	0.511456	0.3721369	0.292675	0.245287	0.212631	0.199693	0.189368	0.182915
2	0.378749	0.2739701	0.213378	0.176412	0.151914	0.141823	0.133988	0.129100
2.25	0.282602	0.2022693	0.156508	0.128444	0.109996	0.102121	0.096157	0.092448
2.5	0.211151	0.1501549	0.115121	0.094067	0.080176	0.074029	0.069486	0.066666
2.75	0.158007	0.1118321	0.085173	0.069226	0.058776	0.053983	0.050519	0.048372
3	0.118406	0.0834559	0.063317	0.051121	0.043274	0.039550	0.036909	0.035273
3.25	0.088866	0.0624380	0.047089	0.037839	0.031961	0.029081	0.027072	0.025827
3.5	0.066721	0.0467229	0.035074	0.028122	0.023707	0.021482	0.019957	0.019012
3.75	0.050071	0.0348967	0.026018	0.020848	0.017563	0.015847	0.014692	0.013977
4	0.037914	0.0260538	0.019247	0.015427	0.013032	0.011703	0.010832	0.010295

Table A-4. The imagery part of the hydrodynamic function of a laterally vibrating beam found as a function of Reynolds number and aspect ratio (*h/b*)

APPENDIX B: MACRO USED IN ANSYS TO COMPUTE HYDRODYNAMIC FORCES

```
!Node spacing on width
varycon=3.33333333333333e-8

!Title (do not run program twice with same title)
/FILNAME, rbbtest1, 1

/CONFIG, NRES, 6002

!Width
h = 20.0e-6

!Reynolds number
Re = 1
!Re = 1.7782794100389228012254211951927
!Re = 3.1622776601683793319988935444327
!Re = 5.6234132519034908039495103977648
!Re = 10

!Re = 17.782794100389228012254211951927
!Re = 31.622776601683793319988935444327
!Re = 56.234132519034908039495103977648
!Re = 100

!Re = 177.82794100389228012254211951927
!Re = 316.22776601683793319988935444327
!Re = 562.34132519034908039495103977648
!Re = 1000

!Re = 1778.2794100389228012254211951927
!Re = 3162.2776601683793319988935444327
!Re = 5623.4132519034908039495103977648
!Re = 10000


!Frequency in water
frq=Re*4e-3/(4e-10*1000*6.283185307)

numcycles=2
numtimedivpercylce=200
numtimdiv= numcycles*numtimedivpercylce

!Set middle of mesh
```

```
mdl=10*h/2.0

!Ratios of node spacings on boundaries
inner=varycon
out=40*inner
outter=out*10

/PREP7

!Set displacement and velocity of beam
*DEL,_FNCNAME
*DEL,_FNCMTID
*SET,_FNCNAME,'DIS'
*DIM,%_FNCNAME%,TABLE,6,8,1
!
! Begin of equation: 1e-7*sin(6.28318*frq*{TIME})
%_FNCNAME%(0,0,1)= 0.0, -999
%_FNCNAME%(2,0,1)= 0.0
%_FNCNAME%(3,0,1)= 0.0
%_FNCNAME%(4,0,1)= 0.0
%_FNCNAME%(5,0,1)= 0.0
%_FNCNAME%(6,0,1)= 0.0
%_FNCNAME%(0,1,1)= 1.0, -1, 0, 6.28318, 0, 0, 0
%_FNCNAME%(0,2,1)= 0.0, -2, 0, frq, 0, 0, -1
%_FNCNAME%(0,3,1)=   0, -3, 0, 1, -1, 3, -2
%_FNCNAME%(0,4,1)= 0.0, -1, 0, 1, -3, 3, 1
%_FNCNAME%(0,5,1)= 0.0, -1, 9, 1, -1, 0, 0
%_FNCNAME%(0,6,1)= 0.0, -2, 0, 1e-7, 0, 0, -1
%_FNCNAME%(0,7,1)= 0.0, -3, 0, 1, -2, 3, -1
%_FNCNAME%(0,8,1)= 0.0, 99, 0, 1, -3, 0, 0
! End of equation: 1e-7*sin(6.28318*frq*{TIME})
!-->

*DEL,_FNCNAME2
*DEL,_FNCMTID
*SET,_FNCNAME2,'VEL'

*DIM,%_FNCNAME2%,TABLE,6,12,1
!
! Begin of equation: 6.283185*frq*1e-7*cos(6.28318*frq*{TIME})
%_FNCNAME2%(0,0,1)= 0.0, -999
%_FNCNAME2%(2,0,1)= 0.0
%_FNCNAME2%(3,0,1)= 0.0
%_FNCNAME2%(4,0,1)= 0.0
%_FNCNAME2%(5,0,1)= 0.0
%_FNCNAME2%(6,0,1)= 0.0
```

```
%_FNCNAME2%(0,1,1)= 1.0, -1, 0, 6.283185, 0, 0, 0
%_FNCNAME2%(0,2,1)= 0.0, -2, 0, frq, 0, 0, -1
%_FNCNAME2%(0,3,1)=   0, -3, 0, 1, -1, 3, -2
%_FNCNAME2%(0,4,1)= 0.0, -1, 0, 1e-7, 0, 0, -3
%_FNCNAME2%(0,5,1)= 0.0, -2, 0, 1, -3, 3, -1
%_FNCNAME2%(0,6,1)= 0.0, -1, 0, 6.28318, 0, 0, 0
%_FNCNAME2%(0,7,1)= 0.0, -3, 0, frq, 0, 0, -1
%_FNCNAME2%(0,8,1)= 0.0, -4, 0, 1, -1, 3, -3
%_FNCNAME2%(0,9,1)= 0.0, -1, 0, 1, -4, 3, 1
%_FNCNAME2%(0,10,1)= 0.0, -1, 10, 1, -1, 0, 0
%_FNCNAME2%(0,11,1)= 0.0, -3, 0, 1, -2, 3, -1
%_FNCNAME2%(0,12,1)= 0.0, 99, 0, 1, -3, 0, 0
! End of equation: 6.283185*frq*1e-7*cos(6.28318*frq*{TIME})
!-->

!Total domain
RECTNG,0,10*h,0,10*h,

!Create fluid inner layer

!square
RECTNG,mdl-h, mdl+h, mdl-h, mdl+h,

ASBA, 1,2,,DELETE,KEEP

!create beam

!RECTNG,mdl-0.0316227766e-6,mdl+0.0316227766e-6,mdl-10e-6,mdl+10e-6,
!RECTNG,mdl-0.0562341325e-6,mdl+0.0562341325e-6,mdl-10e-6,mdl+10e-6,
!RECTNG,mdl-.1e-6,mdl+.1e-6,mdl-10e-6,mdl+10e-6,
!RECTNG,mdl-0.17782794100e-6,mdl+0.17782794100e-6,mdl-10e-6,mdl+10e-6,
!RECTNG,mdl-0.31622776601e-6,mdl+0.31622776601e-6,mdl-10e-6,mdl+10e-6,
!RECTNG,mdl-0.56234132519e-6,mdl+0.56234132519e-6,mdl-10e-6,mdl+10e-6,
!RECTNG,mdl-1e-6,mdl+1e-6,mdl-10e-6,mdl+10e-6,
!RECTNG,mdl-1.7782794100e-6,mdl+1.7782794100e-6,mdl-10e-6,mdl+10e-6,
!RECTNG,mdl-3.1622776601e-6,mdl+3.1622776601e-6,mdl-10e-6,mdl+10e-6,
!RECTNG,mdl-5.6234132519e-6,mdl+5.6234132519e-6,mdl-10e-6,mdl+10e-6,
RECTNG,mdl-10e-6,mdl+10e-6,mdl-10e-6,mdl+10e-6,

ASBA, 2,1,,DELETE, DELETE


et,3,141
KEYOPT,2,4,1
type,2
mat,1
```

```
lsel,s,,,5
lsel,a,,,6
lsel,a,,,7
lsel,a,,,8
Lesize, ALL,out

lsel,s,,,9
lsel,a,,,10
lsel,a,,,11
lsel,a,,,12
Lesize,ALL,inner


!MESH

asel,s,,,4
mshape,1,2d
mshkey,0
amesh,all

allsel
et,4,141
KEYOPT,3,4,1
type,3
mat,1
asel,s,,,3
esize, outter
mshape,1,2d
mshkey,0
amesh,all

!Set DOF

nsel,s,loc,x,0
D,ALL,pres,0.0
D,ALL,UX,0.0,
D,ALL,UY, 0.0

nsel,s,loc,x,10*h
D,ALL,pres,0.0
D,ALL,UX,0.0,
D,ALL,UY, 0.0

nsel,s,loc,y,0
D,ALL,pres,0.0
```

```
D,ALL,UX,0.0,
D,ALL,UY, 0.0

nsel,s,loc,y,10*h
D,ALL,pres,0.0
D,ALL,UX,0.0,
D,ALL,UY,0.0,

lsel,s,,,9
lsel,a,,,10
lsel,a,,,11
lsel,a,,,12
nsll,s,1

!Lateral displacement (switch x and y for transverse displacement)

d,all,UX, 0.0
d,all,UY, %DIS%
d,all,VX, 0.0
d,all,VY, %VEL%
D,ALL,ENKE,-1
allsel
!cdwrite,db,fluid,cdb,
fini
! Flotran Setup
/solu
FLDATA30,QUAD,MOMD,2,
FLDATA30,QUAD,MOMS,2,
FLDATA30,QUAD,PRSD,2,
FLDATA30,QUAD,PRSS,2,
FLDATA30,QUAD,THRD,0,
FLDATA30,QUAD,THRS,0,
FLDATA30,QUAD,TRBD,0,
FLDATA30,QUAD,TRBS,2,
/solu
FLDATA4,TIME,NUMB,100000,

!Set number of cycles
frq2=numcycles/frq                    !2/frq for one cycle
FLDATA4,TIME,TEND,frq2,     !should be 2e-2 for 20 cycles

FLDA,SOLU,ALE,T                 ! ALE solution
FLDATA1,SOLU,FLOW,1
FLDATA1,SOLU,TRAN,1
!FLDATA1,SOLU,TURB,1              !No turbulence
FLDATA2,TIME,GLOB,2400
```

```
FLDATA7,PROT,DENS,Constant
FLDATA8,NOMI,DENS,1000
FLDATA7,PROT,VISC,Constant
FLDATA8,NOMI,VISC, 1e-3
!FLDA,BULK,BETA,1.0e5

!Number of total time instances
frq3=frq2/numtimdiv
FLDA,TIME,STEP, frq3
FLDATA4A, STEP, APPE, 1
!
!!! Newmark method
!
FLDATA,OUTP,TAUW,T
FLDATA,TIME,METH,NEWM
FLDATA,TIME,DELT,0.5
!
!! Set ANSYS-STRUCTURE commands
SAVE
/COM
/COM  Re-meshing Commands
/COM
FLDATA,REMESH,ELEM,ALL        ! all defined element re-meshing
FLDATA,REMESH,ARMA,10.0       ! maximum aspect ratio
FLDATA,REMESH,VOCH,5.0        ! maximum volume change
FLDATA,REMESH,ARCH,5.0        ! maximum aspect ratio change

SOLVE

/post1

!Set path (this should be changed depending on mesh)
PATH,TOP,2,,
PPATH,1,121,
PPATH,2,122,

!code for extracting shear and velocity (PAV)

*DEL,_FNCNAME4
*DEL,_FNCMTID
*SET,_FNCNAME4,'SHE'
*DIM,%_FNCNAME4%,TABLE, numtimdiv,1,1
*DEL,_FNCNAME5
*DEL,_FNCMTID
*SET,_FNCNAME5,'PAV'
```

```
*DIM,%_FNCNAME5%,TABLE, numtimdiv,1,1



count=1
count2= numtimdiv-2


*DOWHILE, count2
count=count+1
SET, 1, count
PDEF,PRV,TAUW
PCALC,INTG,IPV,PRV,YG
*GET,PRDV, Path,   0,      LAST,  IPV
%_FNCNAME4%(count,0,1)= count
%_FNCNAME4%(count,1,1)= PRDV
count2=count2-1
*Enddo

count=1
count2= numtimdiv-2

*DOWHILE, count2
count=count+1
SET, 1, count
PDEF,PRV,VY
PCALC,INTG,IPV,PRV,YG
*GET,PRDV,Path,0,LAST,IPV
%_FNCNAME5%(count,0,1)= count
%_FNCNAME5%(count,1,1)= PRDV
count2=count2-1
*Enddo

!This writes data to a file, only works if run as a .mac macro
*CFOPEN,lg0b1SHElg0,,
*VWRITE,SHE(1)
(F20.14)

*CFOPEN,lg0b1PAVlg0,,
*VWRITE,PAV(1)
(F20.14)

!!Get the pressure force

!Set path (this should be changed depending on mesh)
PATH,TOP2,2,,
```

```
PPATH,1,1322,
PPATH,2,122,

*DEL,_FNCNAME6
*DEL,_FNCMTID
*SET,_FNCNAME6,'PRE'
*DIM,%_FNCNAME6%,TABLE, numtimdiv,1,1

count=1
count2= numtimdiv-2

*DOWHILE, count2
count=count+1
SET, 1, count
PDEF,PRV,PRES
PCALC,INTG,IPV,PRV,XG
*GET,PRDV,Path,0,LAST,IPV
%_FNCNAME6%(count,0,1)= count
%_FNCNAME6%(count,1,1)= PRDV
count2=count2-1
*Enddo

!This writes data to a file, only works if run as a .mac macro
*CFOPEN,lg0b1PRElg0,,
*VWRITE,PRE(1)
(F20.14)

/quit
/clear
```

APPENDIX C: MATLAB PROGRAM USED TO CALCULATE FREQUENCY SPECTRUM OF LATERALLY VIBRATING MICROCANTILEVERS IN VISCOUS LIQUID MEDIA

```
%Lateral Microcantilever Spectrum Plotter

clear;
clc;
%close all;

%index of the frequency
counter0=0;
%modeN=1;

%Frequency range to search
%air
plotl=[1:10:380,380:1:386,386:.1:386.7,386.7:.01:387,387:.1:388,388:1:4
00,400:10:2410,2410:1:2424,2424:.1:2424.3,2424.3:.01:2424.7,2424.7:.1:2
425,2425:1:2440,2450:10:5000,5000:25:6786,6786:.1:6791,6791:25:8000]*2*
pi*10^3;

%base layer Young's modulus
Ep1=169*10^9;

countdown=size(plotl);
for w=plotl

%Displays the clock
counter0=counter0+1;
countdown-counter0

b=45*10^-6; %width
h1=12*10^-6; %base
L=400*10^-6; %length

%choose medium of operation

%52% Glycerol
%pl=998.23*1.1308;
%n=1*10^-3*6.6530;

%air
pl=1.205;
n=1.827*10^-5;

%CCl4
%pl=1590;
%n=8.79*10^-4;

%acetone
%pl=785;
%n=3.08*10^-4;
```

```
%water
%pl=997;
%n=10*10^-4;

mB=2330*(1.00)*b*h1; % 2330 kg/m^3 (Si) * 20 *10^-6 *2 *10^-6+ 917
kg/m^3 (PIB)* same = kg/m

I1=(1/12).*b.^3.*h1;

%flextural rigidity
EIp=Ep1.*I1;


%Reynolds number
Re=(pl.*w.*b.^2)/(4.*n);

%Hydrodynamic function
h=h1;

gamma=2*sqrt(2)/(pi*sqrt(Re))*(((1.657624692.*(h/b)^1.83).*sqrt(Re)+3.0
807413409.*(h/b)^.85+1)  +j.*(     (-
1.321274*(h/b).^1+2.5602901549).*1./sqrt(Re)+3.1077195556.*(h/b).^.85+1
));


%Mass per unit length
mBp=mB+(pi/4).*pl.*b.^2.*real(gamma);
mBpp=(pi/4).*pl.*b.^2.*imag(gamma);

%mode numbers
Bg=[1.87510406871196 4.69409113297418 7.85475743823761 10.9955407348755
14.1371683910465 17.2787595320882 20.4203522510413 23.5619449018064
26.7035375555183 29.8451302091028];

%length index
counter=0;

%change to look at different points along the length,
%currently only looking at beginning, middle and end
overlength=0:(L/2):L/1;

for x=overlength

    counter=counter+1;
    wxtotal=0;
    for i=1:10

        Bi=Bg(i)./L;

        %mode shape
```

```
        phi=((cos(Bi.*x)-
cosh(Bi.*x)).*(cos(Bi.*L)+cosh(Bi.*L))+(sin(Bi.*x)-
sinh(Bi.*x)).*(sin(Bi.*L)-sinh(Bi.*L))).(sin(Bi.*L)-sinh(Bi.*L));
        F1= @(x) (((cos(Bi.*x)-
cosh(Bi.*x)).*(cos(Bi.*L)+cosh(Bi.*L)))./(sin(Bi.*L)-
sinh(Bi.*L))+(sin(Bi.*x)-sinh(Bi.*x)));

        %Modal excitation assumption  %uncomment to force in modeshape
of mode

        %if i==modeN
                %integral top part
            itp=quad(F1,0,L);
        %else
        %    itp=0;
        %end

        F2= @(x) (((cos(Bi.*x)-
cosh(Bi.*x)).*(cos(Bi.*L)+cosh(Bi.*L)))./(sin(Bi.*L)-
sinh(Bi.*L))+(sin(Bi.*x)-sinh(Bi.*x))).^2;

        %second integral part
        sip=quad(F2,0,L);

        %frequency dependent part
        fdp=(EIp.*(Bi.*L).^4-mBp.*w.^2.*L.^4)+j*(mBpp.*w.^2.*L.^4);

        Fx=(175/400)*10^-6;%constant force along beam

        %amplitude of delection @ x
        C=L^4*(Fx*itp./(fdp.*sip));

        %deflection from this mode
        wx=C.*phi;

        %total defelction
        wxtotal=wx+wxtotal;

        %store deflection for this mode
        wxi(i)=wx;


    end

    %store deflections as a function of x

    Wbig(counter)=(wxtotal);

    Wpart(counter)=(wxi(1));
    Wpart2(counter)=(wxi(2));
    Wpart3(counter)=(wxi(3));
    Wpart4(counter)=(wxi(4));
    Wpart5(counter)=(wxi(5));
    Wpart6(counter)=(wxi(6));
```

```
    Wpart7(counter)=(wxi(7));
    Wpart8(counter)=(wxi(8));


end

%store tip deflection as a function of frequency
%(You can look at different points on the beam
%by changing ENDL to the correct index)
[nothing ENDL]=size(overlength);
%ENDL=2;
sweep1(counter0)=Wpart(ENDL);
sweep2(counter0)=Wpart2(ENDL);
sweep3(counter0)=Wpart3(ENDL);
sweep4(counter0)=Wpart4(ENDL);
sweep5(counter0)=Wpart5(ENDL);
sweep6(counter0)=Wpart6(ENDL);
sweep7(counter0)=Wpart7(ENDL);
sweep8(counter0)=Wpart8(ENDL);
sweep(counter0)=Wbig(ENDL);



end

%Plot graphs

rad=2*pi*10^3

%Change this to normalize sweep to a particular value
maxabssweep=max(abs(sweep));

figure (14)
grid('on');
hold on;
plot(plotl./(rad),20*log10(abs(sweep)./maxabssweep),'r')
plot(plotl./(rad),20*log10(abs(sweep1)./maxabssweep),'r--')
plot(plotl./(rad),20*log10(abs(sweep2)./maxabssweep),'r--')
plot(plotl./(rad),20*log10(abs(sweep3)./maxabssweep),'r--')

%air (transverse resonant frequencies)
plot([103.046173231076,103.046173231076],[min(20*log10(abs(sweep)./maxa
bssweep)) 0],'k')
plot([645.964652687217,645.964652687217],[min(20*log10(abs(sweep)./maxa
bssweep)) 0],'k')
plot([1808.86734001235,1808.86734001235],[min(20*log10(abs(sweep)./maxa
bssweep)) 0],'k')
plot([3544.78700981296,3544.78700981296],[min(20*log10(abs(sweep)./maxa
bssweep)) 0],'k')
plot([5859.9095844272,5859.9095844272],[min(20*log10(abs(sweep)./maxabs
sweep)) 0],'k')
%plot([8753.80997837765,8753.80997837765],[min(20*log10(abs(sweep)./max
(abs(sweep)))) 0],'k')
```

```
%water
%
plot([64.1961148174447,64.1961148174447],[min(log10(abs(sweep)./maxabss
weep)) 0],'k')
%plot([417.699903858705,417.699903858705],[min(log10(abs(sweep)./maxabs
sweep)) 0],'k')
%plot([1182.20035206476,1182.20035206476],[min(log10(abs(sweep)./maxabs
sweep)) 0],'k')
%plot([2327.68289764804,2327.68289764804],[min(log10(abs(sweep)./maxabs
sweep)) 0],'k')
%plot([3858.31415669093,3858.31415669093],[min(log10(abs(sweep)./maxabs
sweep)) 0],'k')
```

APPENDIX D: MATLAB PROGRAM USED TO CALCULATE CHARATERISTICS OF LATERALLY VIBRATING MICROCANTILEVERS IN VISCOUS LIQUID MEDIA

```
%This is the matlab algorithm for investigation of laterally excited
%microcantilevers

%Technical (remove close all to allow for multiple run plots)
clc;
clear all;
%close all;

%switches (mode active [on = 1, off = 0])
%Choose which parameter to sweep
watergly=0;
watereth=0;
varyh1=1;
varyb=0;
varyL=0;



%Choose min, max, and step size of parameter sweep
%For water-gly and water-eth, use integer values
%representing the first and last data points desired
bottom=45*10^-6; %Note: Do not set to zero
every=15*10^-6;
top=90.001*10^-6; %.001 added so that bottom!=top

%Choose default beam geometry
h1=12*10^-6; %Thickness [in meters]
b=45*10^-6;   %Width [in meters]
L=200*10^-6;  %Length [in meters]

%Mode numbers
Bg=[1.87510406871196 4.69409113297418 7.85475743823761 10.9955407348755
14.1371683910465 17.2787595320882 20.4203522510413 23.5619449018064
26.7035375555183 29.8451302091028];

%Choose mode number
bl=Bg(1);
rad=2*pi;

%Operational Medium Properties:

%glycerol data: 37 points

%Viscosity
gnarray=[1 1.009 1.020 1.046 1.072 1.098 1.125 1.155 1.186 1.218 1.253
1.288 1.362 1.442 1.530 1.627 1.734 1.984 2.274 2.632 3.082 3.646 4.434
5.402 6.653 8.332 10.66 13.63 18.42 27.57 40.49 59.78 84.17 147.2 383.7
778.9 1759.6];
```

```
%Density
gplarray=[1 .9994 1.0005 1.0028 1.0051 1.0074 1.0097 1.0120 1.0144
1.0167 1.0191 1.0215 1.0262 1.0311 1.036 1.0409 1.0459 1.0561 1.0664
1.0770 1.0876 1.0984 1.1092 1.1200 1.1308 1.1419 1.1530 1.1643 1.1755
1.1866 1.1976 1.2085 1.2192 1.2299 1.2404 1.2508 1.2611];
%Percent (w/w) aqueous glycerol
gperarray=[0 .5 1 2 3 4 5 6 7 8 9 10 12 14 16 18 20 24 28 32 36 40 44
48 52 56 60 64 68 72 76 80 84 88 92 96 100] ;

%ethanol data: 71 points

%Viscosity
eplarray=[1 .9973 .9963 .9954 .9945 .9936 .9927 .9918 .9910 .9902 .9893
.9885 .9878 .9870 .9862 .9855 .9847 .9840 .9833 .9826 .9819 .9805 .9792
.9778 .9765 .9752 .9739 .9726 .9713 .9700 .9687 .9660 .9632 .9602 .9571
.9539 .9504 .9468 .9431 .9392 .9352 .9311 .9269 .9227 .9183 .9139 .9095
.9049 .9004 .8958 .8911 .8865 .8818 .8771 .8724 .8676 .8629 .8581 .8533
.8485 .8436 .8387 .8335 .8284 .8232 .8180 .8125 .8070 .8013 .7954
.7893];
%Density
enarray=[1 1.021 1.044 1.068 1.093 1.116 1.138 1.159 1.181 1.203 1.226
1.250 1.276 1.301 1.328 1.355 1.382 1.411 1.439 1.468 1.498 1.560 1.624
1.691 1.757 1.822 1.886 1.951 2.015 2.077 2.138 2.254 2.365 2.471 2.576
2.662 2.721 2.762 2.797 2.823 2.840 2.846 2.844 2.837 2.826 2.807 2.783
2.749 2.696 2.627 2.542 2.474 2.410 2.342 2.276 2.210 2.144 2.078 2.011
1.944 1.877 1.804 1.738 1.671 1.603 1.539 1.472 1.404 1.339 1.270
1.201];
%Percent (w/w) aqueous ethanol
eperarray=[0 .5 1 1.5 2 2.5 3 3.5 4 4.5 5 5.5 6 6.5 7 7.5 8 8.5 9 9.5
10 11 12 13 14 15 16 17 18 19 20 22 24 26 28 30 32 34 36 38 40 42 44 46
48 50 52 54 56 58 60 62 64 66 68 70 72 74 76 78 80 82 84 86 88 90 92 94
96 98 100];

%Water
nwa=1*10^-3;   %Viscosity of water in Pa * s, or kg/(m s)  @ 20'C (@
T=25'C= .89*10^-3) (1 cP= 10^-3 Pa*s)
plwa=997;       %Density of water in kg/m^3

%Air
nair=1.827*10^-5 ; %viscosity of air in Pa * s from CRC (1984, pp.F-42-
44, a different CRC than the one in the lab)
plair=1.205;       %density of air in kg/m^3 from CRC

%Uncomment to Run in Air
%nwa=nair;
%plwa=plair;

%Uncomment here and in algorithm to force a particular gamma value
%saderin=1.696626383+j.*0.211151462;

%Indexing variable
c=0;

for param=bottom:every:top
```

```
c=c+1; %Main counter
n=nwa;
pl=plwa;

%%%If statements to put param into the right variable%%%
if watergly==1;
    n=gnarray(c)*nwa;
    pl=gplarray(c)*plwa;
    per=gperarray(c);
end
if watereth==1;
    n=enarray(c)*nwa;
    pl=eplarray(c)*plwa;
    per=eperarray(c);
end
if varyb==1;
    b=param;
end
if varyh1==1;
    h1=param;
end
if varyL==1;
    L=param;
end

%%%Define everything%%%

%beam density
pB=2330;

%mass per unit length
mB=pB*b*h1;

%Young's modulus of beam
Ep1=(127.5*10^9); %Pa= kg/(m s^2) Si:169e9 Experimental:127.5e9

%Vacuum Resonant Frequency
I1=(1/12).*b^3.*h1;
EIp=Ep1.*I1;
Pwvac(c)=((bl.^2)./L.^2).*sqrt(EIp./mB);

%initial frequency
w=Pwvac(c);

wh = Pwvac(c);

%%Find an approximation for the resonant frequency%%%
for iteration=1:20

    %Centroidal moment of inertia
    I1=(1/12).*b^3.*h1;

    EIp=Ep1.*I1;
```

```
            %Reynolds number
            Re=(pl.*wh.*b.^2)/(4.*n);

            %Hydrodynamic function (Stokes' approximation)
            gamma=sqrt(2)*2./(pi*sqrt(Re))*(1+j);

            mBp=mB+(pi/4).*pl.*b.^2.*real(gamma);
            mBpp=(pi/4).*pl.*b.^2.*imag(gamma);

            %resonant frequency

      wh=((bl.^2)./L.^2).*sqrt((mBp.*EIp)./(mBp.*mBp+mBpp.*mBpp));

        end

        %Lateral ribbon quality factor
        IQlr=(mBpp)./(mBp);
        Qlr=1./(2.*(1-sqrt(1-abs(IQlr))));

        %Collect plot variable data from Stokes' solution
        PQlr(c)=Qlr;
        Pwlr(c)=wh;
        Pg2s(c)=(pi/4).*pl.*b.^2.*2.*sqrt(2)./(pi*sqrt(Re));
        Pg1s(c)=Pg2s(c).*Pwlr(c);
        PRes(c)=Re;

        %%%Calc exact res freq%%%

        %initial approximation
        wh2d=wh;

        for iteration=1:20

            %centroidal moment of inertia
            I1=(1/12).*b^3.*h1;
            EIp=Ep1.*I1;

            %Reynolds number
            Re=(pl.*wh2d.*b.^2)/(4.*n);
            h=h1;

            %Hydrodynamic function found from ANSYS

gamma2d=2*sqrt(2)/(pi*sqrt(Re))*(((1.657624692.*(h/b)^1.83).*sqrt(Re)+3
.0807413409.*(h/b)^.85+1)  +j.*(    (-
1.321274*(h/b).^1+2.5602901549).*1./sqrt(Re)+3.1077195556.*(h/b).^.85+1
));

            mBp2d=mB+(pi/4).*pl.*b.^2.*real(gamma2d);
            mBpp2d=(pi/4).*pl.*b.^2.*imag(gamma2d);

            %Effective spring constant (off by factor of three from
normal
```

```
            %notation)
            klat= (EIp./L.^3);

            %Effective mass (with the dgamma/dw accounted for)
            Mlat = mBp2d.*L+L.*((mBpp2d-
((sqrt(2).*pl.*b.^2./4./Re).*(2.5602901549-
1.321274.*(h./b))+(sqrt(2).*pl.*b.^2./8./sqrt(Re)).*(3.1077195556.*(h./
b).^0.85+1)))./(mBp2d-
((sqrt(2).*pl.*b.^2./8./sqrt(Re)).*(3.0807413409.*(h./b).^.85+1))))).*mB
pp2d;

            %Resonant frequency
            wh2d=(bl.^2).*sqrt(klat./Mlat);
        end

        Pw2d(c)=wh2d;

        %%%Quality factor with Thickness Effects%%%
        IQ2d=(mBpp2d)./(mBp2d);
        Qapprox=1./IQ2d;
        if IQ2d>1
            Q2d=1./(sqrt(1+abs(IQ2d)));
        else
            Q2d=1./(2.*(1-sqrt(1-abs(IQ2d))));
        end

        %%%Sensitivity%%%

        A=mBpp2d;
        Apdiv=(mBpp2d-((sqrt(2).*pl.*b.^2./4./Re).*(2.5602901549-
1.321274.*(h./b))+(sqrt(2).*pl.*b.^2./8./sqrt(Re)).*(3.1077195556.*(h./
b).^0.85+1)));
        Bpdiv=(mBp2d-
((sqrt(2).*pl.*b.^2./8./sqrt(Re)).*(3.0807413409.*(h./b).^.85+1)));

        B=mBp2d;
        k=(EIp)/L.^3;

        %If forcing a particular gamma, use these lines
        %M=L.*B+L.*(A.^2./B);
        %lamM(c)=((A.^2.*EIp)./(2.*k.*L.*M.*(L.*B).^2)-1./(2.*M));%

        %Normalized mass sensitivity
        M = mBp2d.*L+L.*((mBpp2d-
((sqrt(2).*pl.*b.^2./4./Re).*(2.5602901549-
1.321274.*(h./b))+(sqrt(2).*pl.*b.^2./8./sqrt(Re)).*(3.1077195556.*(h./
b).^0.85+1)))./(mBp2d-
((sqrt(2).*pl.*b.^2./8./sqrt(Re)).*(3.0807413409.*(h./b).^.85+1))))).*mB
pp2d;
        lamM(c)=((A.*Apdiv.*EIp)./(2.*k.*L.*M.*(L.*Bpdiv).^2)-
1./(2.*M));%

        %Mass sensitivity in Hz/kg
        PSmass(c)=lamM(c).*(Pw2d(c)/(2*pi));
```

```
        %Mass sensitivity approx
        lamMap(c)=(1./(2.*M));
        PSmap(c)=(1./(2.*M)).*(Pw2d(c)/(2*pi));

        %Normalized Chemical sensitivity in Hz/pg * um^2
        PScbar(c)= (PSmass(c)./1000./10.^12).*b.*L.*10^12;


        %Collect plot variable data
        Phb(c)=h1/b;
        PRe(c)=Re;
        Pgamma2d(c)=gamma2d;
        PmBp2d(c)=mBp2d;
        PmBpp2d(c)=mBpp2d;
        Pklat(c)=klat;
        PMlat(c)=Mlat;
        Pw2d(c)=wh2d;
        Pf2d(c)=wh2d./(2*pi);
        PQ2d(c)=Q2d;
        PQapprox(c)=Qapprox;

        Pg1(c)=mBpp2d.*wh2d;
        Pg2(c)=(pi/4).*pl.*b.^2.*real(gamma2d);
        Pnwa(c)=nwa;
        PL(c)=L;
        Pb(c)=b;
        Ph(c)=h1;


        %%%Calculate other approximations%%%

        %Re>>1 approximation res freq (no-div [nd])

        wh2dnd=wh;

        for iteration=1:20

            %Centroidal moment of inertia
            I1=(1/12).*b^3.*h1;
            EIp=Ep1.*I1;

            %Reynolds number
            Re=(pl.*wh2dnd.*b.^2)/(4.*n);

            %Hydrodynamic function found from ANSYS
            h=h1;

gamma2dnd=2*sqrt(2)/(pi*sqrt(Re))*(((1.657624692.*(h/b)^1.83).*sqrt(Re)
+3.0807413409.*(h/b)^.85+1)  +j.*(     (-
1.321274*(h/b).^1+2.5602901549).*1./sqrt(Re)+3.1077195556.*(h/b).^.85+1
));

            %Uncomment here and above to force a particular gamma value
            %gamma2d=saderin;
```

```
            mBp=mB+(pi/4).*pl.*b.^2.*real(gamma2dnd);
            mBpp=(pi/4).*pl.*b.^2.*imag(gamma2dnd);

            %resonant frequency

wh2dnd=((bl.^2)./L.^2).*sqrt((mBp.*EIp)./(mBp.*mBp+mBpp.*mBpp));
        end

        Pw2dnd(c)=wh2dnd;

        %%%Quality factor with Thickness Effects%%%
        IQ2dnd=(mBpp)./(mBp);
        Qapproxnd=1./IQ2dnd;
        if IQ2dnd>1
            Q2dnd=1./(sqrt(1+abs(IQ2dnd)));
        else
            Q2dnd=1./(2.*(1-sqrt(1-abs(IQ2dnd))));
        end

        A=mBpp;
        B=mBp;
        k=(EIp)/L.^3;
        M=L.*B+L.*(A.^2./B);
        lamMnd(c)=((A.^2.*EIp)./(2.*k.*L.*M.*(L.*B).^2)-1./(2.*M));%

        %Mass sensitivity in Hz/kg
        PSmassnd(c)=lamM(c).*(Pw2dnd(c)/(2*pi));

        %Mass sensitivity approx
        lamMapnd(c)=(1./(2.*M));
        PSmapnd(c)=(1./(2.*M)).*(Pw2dnd(c)/(2*pi));

        %Collect plot variable data
        Pgamma2dnd(c)=gamma2dnd;
        PmBp2dnd(c)=mBp;
        PmBpp2dnd(c)=mBpp;
        Pw2dnd(c)=wh2dnd;
        PQ2dnd(c)=Q2dnd;
        PQapproxnd(c)=Qapproxnd;



        %Inviscid approximation [in]
        wh2din=wh;

        for iteration=1:20

            %centroidal moment of inertia
            I1=(1/12).*b^3.*h1;
            EIp=Ep1.*I1;

            %Reynolds number
            Re=(pl.*wh2din.*b.^2)/(4.*n);
```

```
            h=h1;

            %Inviscid approximation [works for 0<h/b<<1, Re=inf]

gamma2din=(2./(pi.^2)).*(h1./b).^2.*(1+2.*log(4.*pi.*b./h));

            mBp2d=mB+(pi/4).*pl.*b.^2.*real(gamma2din);
            mBpp2d=(pi/4).*pl.*b.^2.*imag(gamma2din);

            %Effective spring constant (off by factor of three from
normal
            %notation)
            klat= (EIp./L.^3);

            %Effective mass (with the dgamma/dw accounted for)
            Mlat = mBp2d.*L+L.*((mBpp2d-
((sqrt(2).*pl.*b.^2./4./Re).*(2.5602901549-
1.321274.*(h./b))+(sqrt(2).*pl.*b.^2./8./sqrt(Re)).*(3.1077195556.*(h./
b).^0.85+1))))./(mBp2d-
((sqrt(2).*pl.*b.^2./8./sqrt(Re)).*(3.0807413409.*(h./b).^.85+1)))).*mB
pp2d;

            %Resonant frequency
            wh2din=(bl.^2).*sqrt(klat./Mlat);
        end

        Pw2din(c)=wh2din;




        %Countdown clock: if numbers to high, change the value of
"every"
        top/every-c-bottom




end

  %A2 will output a resonant frequency [kHz], quality factor, and Sm
[Hz/pg]

  A2(:,1)=Pw2d./2./pi/10^3;
  A2(:,2)=PQ2d;
  A2(:,3)=(abs(PSmass)/1000/10^12);

%if statements separating different plot types

if varyb==1

     %b/L^2 vs. Resonant frequency (kHz)
     figure (1)
     hold on;
     plot((bottom:every:top)./(PL.^2),Pw2d./(rad*10^3),'b')
```

```
     grid('on');
     xlabel('b/L^2 [m^-1]');
     ylabel('resonant frequency [kHz]');

     %sqrt(b)/L vs. Quality Factor
     figure (2)
     hold on;
     plot(sqrt(bottom:every:top)./(PL),PQ2d,'b')
     grid('on');
     xlabel('b^1/2/L [m^-1/2]');
     ylabel('Quality Factor');


     %b/L^2 vs. Scbar
     figure (3)
     hold on;
     plot((bottom:every:top)./(PL.^2),abs(PScbar),'b')
     grid('on');
     xlabel('b/L^2 [m^-1]');
     ylabel(‘Normalized Chemical Sensitivity [Hz/pg * um^2]');


 end

if varyL==1

     %b/L^2 vs. Resonant frequency (kHz)
     figure (1)
     hold on;
     plot(Pb./(bottom:every:top).^2,Pw2d./(rad*10^3),'b')
     grid('on');
     xlabel('b/L^2 [m^-1]');
     ylabel('resonant frequency [kHz]');

     %sqrt(b)/L vs. Quality Factor
     figure (2)
     hold on;
     plot(sqrt(Pb)./(bottom:every:top),PQ2d,'b')
     grid('on');
     xlabel('b^1/2/L [m^-1/2]');
     ylabel('Quality Factor');

     %b/L^2 vs. Scbar
     figure (3)
     hold on;
     plot(Pb./(bottom:every:top).^2,abs(PScbar),'b')
     grid('on');
     xlabel('b/L^2 [m^-1]');
     ylabel(‘Normalized Chemical Sensitivity [Hz/pg * um^2]');

end

if varyh1==1
```

```
     %h1 (um) vs. Resonant frequency (kHz)
     figure (1)
     hold on;
     plot((bottom:every:top).*10^6,Pw2d./(rad*10^3),'b')
     grid('on');
     xlabel('h [um]');
     ylabel('resonant frequency [kHz]');

     %h1 (um) vs. Quality Factor
     figure (2)
     hold on;
     plot((bottom:every:top).*10^6,PQ2d,'b')
     grid('on');
     xlabel('h [um]');
     ylabel('Quality Factor');

     %h1 (um) vs. Scbar
     figure (3)
     hold on;
     plot((bottom:every:top).*10^6,abs(PScbar),'b')
     grid('on');
     xlabel('h [um]');
     ylabel(‘Normalized Chemical Sensitivity [Hz/pg * um^2]');

 end

if watergly==1

     %Re vs. Resonant frequency (kHz)
     figure (1)
     hold on;
     plot(PRe,Pw2d./(rad*10^3),'b')
     plot(PRe,Pw2dnd./(rad*10^3),'r--')
     plot(PRe,Pw2din./(rad*10^3),'k')
     grid('on');
     xlabel('Reynolds Number');
     ylabel('resonant frequency [kHz]');

     %sqrt(Re) vs. Quality Factor
     figure (2)
     hold on;
     plot(sqrt(PRe),PQ2d,'k')
     plot(sqrt(PRe),PQapprox,'r--')
     grid('on');
     xlabel('Reynolds Number');
     ylabel('Quality Factor');

     %Re vs. Smass
     figure (3)
     hold on;
     plot(PRe,abs(PSmass)/1000/10^12,'b')
     plot(PRe,abs(PSmap)/1000/10^12,'r--')
     grid('on');
     xlabel('Reynolds Number');
     ylabel(‘Mass Sensitivity [Hz/pg]');
```

```
    % %gly vs. Resonant frequency (kHz)
     figure (4)
     hold on;
     plot(gperarray(bottom:every:top),Pw2d./(rad*10^3),'b')
     grid('on');
     xlabel('Percent Aqueous Glycerol’);
     ylabel('resonant frequency [kHz]');

     % %gly vs. Quality Factor
     figure (5)
     hold on;
     plot(gperarray(bottom:every:top),PQ2d,'b')
     grid('on');
     xlabel('Percent Aqueous Glycerol’);
     ylabel('Quality Factor');

     % %gly vs. Smass
     figure (6)
     hold on;
     plot(gperarray(bottom:every:top),abs(PSmass)/1000/10^12,'b')
     grid('on');
     xlabel('Percent Aqueous Glycerol’);
     ylabel(‘Mass Sensitivity [Hz/pg]');

end

if watereth==1

     %Re vs. Resonant frequency (kHz)
     figure (1)
     hold on;
     plot(PRe,Pw2d./(rad*10^3),'b')
     plot(PRe,Pw2dnd./(rad*10^3),'r--')
     plot(PRe,Pw2din./(rad*10^3),'k')
     grid('on');
     xlabel('Reynolds Number');
     ylabel('resonant frequency [kHz]');

     %sqrt(Re) vs. Quality Factor
     figure (2)
     hold on;
     plot(sqrt(PRe),PQ2d,'k')
     plot(sqrt(PRe),PQapprox,'r--')
     grid('on');
     xlabel('Reynolds Number');
     ylabel('Quality Factor');

     %Re vs. Smass [Hz/pg]
     figure (3)
     hold on;
     plot(PRe,abs(PSmass)/1000/10^12,'b')
     plot(PRe,abs(PSmap)/1000/10^12,'r--')
     grid('on');
     xlabel('Reynolds Number');
     ylabel(‘Mass Sensitivity [Hz/pg]');
```

```
     % %gly vs. Resonant frequency (kHz)
     figure (4)
     hold on;
     plot(eperarray(bottom:every:top),Pw2d./(rad*10^3),'b')
     grid('on');
     xlabel('Percent Aqueous Ethanol’);
     ylabel('resonant frequency [kHz]');

     % %gly vs. Quality Factor
     figure (5)
     hold on;
     plot(eperarray(bottom:every:top),PQ2d,'b')
     grid('on');
     xlabel('Percent Aqueous Ethanol’);
     ylabel('Quality Factor');

     % %gly vs. Smass [Hz/pg]
     figure (6)
     hold on;
     plot(eperarray(bottom:every:top),abs(PSmass)/1000/10^12,'b')
     grid('on');
      xlabel('Percent Aqueous Ethanol’);
      ylabel(‘Mass Sensitivity [Hz/pg]');

end
```